3-21-2019

# Initial Stage of Fluid-Structure Interaction of a Celestial Icosahedron Shaped Vacuum Lighter Than Air Vehicle

Dustin P. Graves

Follow this and additional works at: https://scholar.afit.edu/etd

Ⓖ Part of the Aerodynamics and Fluid Mechanics Commons, Fluid Dynamics Commons, and the Structures and Materials Commons

**INITIAL STAGE OF FLUID-STRUCTURE INTERACTION OF A CELESTIAL ICOSAHEDRON SHAPED VACUUM LIGHTER THAN AIR VECHICLE**

THESIS

Dustin P. Graves, Captain, USAF

AFIT-ENY-MS-19-M-216

**DEPARTMENT OF THE AIR FORCE**
**AIR UNIVERSITY**
# AIR FORCE INSTITUTE OF TECHNOLOGY

**Wright-Patterson Air Force Base, Ohio**

The views expressed in this thesis are those of the author and do not reflect the official policy or position of the United States Air Force, Department of Defense, or the United States Government.  This material is declared a work of the U.S. Government and is not subject to copyright protection in the United States.

AFIT-ENY-MS-19-M-216

AERODYNAMIC ANALYSIS OF A CELESTIAL ICOSAHEDRON SHAPED VACUUM
LIGHTER THAN AIR VEHICLE

THESIS

Presented to the Faculty

Department of Aeronautics and Astronautics

Graduate School of Engineering and Management

Air Force Institute of Technology

Air University

Air Education and Training Command

In Partial Fulfillment of the Requirements for the

Degree of Master of Science in Aeronautical Engineering

Dustin P. Graves, BS

Captain, USAF

March 2019

AFIT-ENY-MS-19-M-216

# AERODYNAMIC ANALYSIS OF A CELESTIAL ICOSAHEDRON SHAPED VACUUM LIGHTER THAN AIR VEHICLE

Dustin P. Graves, BS

Captain, USAF

Committee Membership:

Anthony Palazotto, PhD
Chair

Mitch Wolff, PhD
Member

Mark Reeder, PhD
Member

# Abstract

The analysis of a celestial icosahedron geometry is considered as a potential design for a Vacuum Lighter than Air Vehicle (VLTAV). The goal of the analysis is ultimately to understand the initial fluid-structure interaction of the VLTAV and the surrounding airflow. Up to this point, previous research analyzed the celestial icosahedron VLTAV in relation to withstanding a symmetric sea-level pressure applied to the membrane of the structure. This scenario simulates an internal vacuum being applied in the worst-case atmospheric environmental condition. The next step in analysis is to determine the aerodynamic effects of the geometry. The experimental setup for obtaining aerodynamic effects is validated prior to analyzing the deformed celestial icosahedron geometry by analyzing a perfect sphere utilizing the same manufacturing process and setup expected to be adopted for the celestial icosahedron experiments. The data received from Computational Fluid Dynamics (CFD) analysis of the deformed structure in collaboration with Wright State University is used to determine the significance of aerodynamic effects on the structure. The pressure profiles experienced in the wind tunnel experiments and CFD analysis are comparatively similar. Therefore, the CFD data is used to conduct a structural analysis in which aerodynamic effects are incorporated. The research concluded that the aerodynamic pressures do not significantly affect the stress on the structure. As a result, it recommended that a full nonlinear fluid-structure interaction analysis is not necessary for this structure.

# Acknowledgments

I would like to thank my advisor, Dr. Anthony Palazotto, for continued involvement and mentorship throughout the time I spent conducting research. I would like to thank the committee members for my defense to include Dr. Mark Reeder and Dr. Mitch Wolff for their involvement and guidance as well. Lastly, I would like to thank Dr. Jaimie Tiley from the Air Force Office of Scientific Research for the continued support and funding of this research.

Dustin P. Graves

# Table of Contents

# List of Figures

# List of Tables

# List of Symbols

| | |
|---|---|
| $c_a$ | Correction Value |
| $C_D$ | Drag Coefficient |
| $D$ | Diameter |
| $D_s$ | Diameter of Structural Analysis Model |
| $D_w$ | Diameter of Wind Tunnel Model |
| $I_a$ | Internal Load |
| $kg$ | Kilogram |
| $k_L$ | Laminar Kinetic Energy |
| $k_o$ | Original Stiffness |
| $k_T$ | Turbulent Kinetic Energy |
| $lb$ | Pound Mass |
| $m$ | Meter |
| $mm$ | Millimeter |
| $N$ | Newton |
| $P$ | Applied Load |
| $psid$ | Pounds per Square Inch Differential |
| $R_a$ | Residual Force |
| $Re$ | Reynolds number |
| $u_a$ | New Configuration |
| $u_o$ | Original Configuration |
| $U_s$ | Maximum Displacement of Structural Analysis Model |
| $U_w$ | Maximum Displacement of Wind Tunnel Model |
| $V$ | Velocity |
| $\epsilon$ | Strain |
| $\mu$ | Kinematic Viscosity |
| $\mu m$ | Micrometer |
| $\omega$ | Turbulent Time Scale |

# I.  Introduction

## 1.1  Chapter Overview

Throughout history, humans have utilized lighter than air vehicles (LTAV) as a form of air travel. Mankind produced many iterations of the LTAV as well, utilizing different forms of obtaining a lighter than air gas within the membrane of a structure. Methods used include heating the internal air of the LTAV as well as using lighter than air gases to include hydrogen and helium. However, the prospect of utilizing sufficiently strong and light materials with the air inside the body being excavated to create a vacuum has yet to be manufactured and tested as a lighter than air vehicle. A vacuum lighter than air vehicle (VLTAV), which is used in this research, presents pros and cons to a traditional LTAV.

The introductory chapter lays the framework for the objective of the research, the motivation for the research, a background on the research, history of lighter than air vehicles, previous research, and an overview of the thesis.

## 1.2  Objective

The objective of this thesis is to determine whether the aerodynamic effects of a celestial icosahedron VLTAV, from Kyle Moore's work, significantly affect the structural integrity of the VLTAV model [1],[2],[3]. Comparing the structural response to aerodynamic effects with the structural response of an internal vacuum at sea-level pressure provides insight into whether or not it is important to consider aerodynamic effects in future research for this vehicle. The pressures experienced by the structures as they resist freestream airflow can be utilized to update the structural

1

analysis models. The models incorporated in the research so far have assumed symmetric sea-level pressure acting on the surface of the membrane for the different structures considered here at the Air Force Institute of Technology (AFIT). However, since this is a dynamic problem, the effects of airflow around the structure must be taken into consideration when structurally analyzing the VLTAVs.

### 1.3    Motivation

The motivation behind studying the feasibility of a VLTAV is simple; the advantages of a VLTAV over a traditional LTAV increase the utility of the air vehicle. One of the main issues of the historical LTAVs, which utilize lighter than air gases, is the simple fact that they leak. The permeability of the balloon structures in a traditional LTAV is not low enough to prevent the lighter than air gases from leaking out. Therefore, in order to maintain a consistent altitude over a period of time, traditional LTAVs must carry reserve stores of their lighter than air gas. This, in turn, reduces the overall payload that the LTAV withstands to make room for the reserves. Along with reducing payload, at some point the craft must return to the surface to reestablish its gas reserves. Although a VLTAV is not impermeable theoretically, the advantages of a vacuum over lighter than air gas with respect to reserves is readily apparent. First, the VLTAV does not require the storage of on-board reserves of lighter-than-air gas which increases the effective payload of the overall craft. Admittedly, the VLTAV does require an on-board pump to extract any atmospheric air that permeates the membrane of the vehicle. Secondly, because the vehicle does not rely on a reserve supply of gas, the VLTAV does not require returning to the

2

surface for resupply. The VLTAV, therefore, indefinitely loiters with the constraint resting on the operational capability of the on-board pump. [4]

Along with the loiter advantages, a VLTAV could change altitude more readily than a traditional LTAV. Traditional vehicles require the usage of ballast (by either taking on to descend or removing to ascend) to adjust their altitude. A VLTAV, however, allows atmospheric air in to descend or extracts atmospheric air to ascend via an on-board pump system likely with an electronic controller. [4]

The uses of a VLTAV are vast. A network of the balloons equipped with solar arrays could be utilized above the cloud layer to collect solar energy or a network of the balloons could be used to collect water within the atmosphere. [4]

Although there are many civilian applications for a VLTAV, this thesis is concerned with the applications within the military environment. Utilizing the extended loiter time of a VLTAV, the military could enhance the capabilities of intelligence, surveillance, and reconnaissance (ISR). A VLTAV could transport the payload necessary to conduct ISR missions while loitering indefinitely in a pre-defined position. Apart from ISR, loiter time of the VLTAV could be utilized by the military to enhance or to increase the redundancy of Nuclear Command, Control, and Communications (NC3) networks.

## 1.4 Background

Francesco Lana de Terzi first introduced the concept of a VLTAV in 1663. De Terzi's concept, as shown in Figure I-1, utilized copper spheres connected to a ship design which would be evacuated of air in order to provide buoyancy. Although the volume of air displaced by the internal vacuums of the copper spheres would

3

theoretically weigh more than the materials of the ship itself, de Terzi had not accounted for the buckling effect of the external atmosphere collapsing the copper balloons. [5]
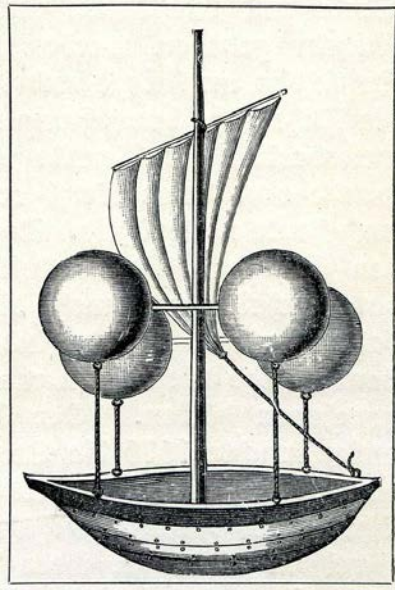


**Figure I-1. Francesco Lana de Terzi's VLTAV concept** [5]

To maintain the feasibility of a VLTAV, an internal structure must be introduced that withstands the external pressure of the surrounding atmosphere. Throughout the theses and dissertation research conducted at the Air Force Institute of Technology (AFIT), there have been many geometric structures designed and analyzed to determine the feasibility of a VLTAV. Of the structures analyzed so far, three designs maintained the greatest feasibility to include the icosahedron frame, the hexakis frame, and the celestial icosahedron frame. The icosahedron consists of 20 equilateral triangles and 12 vertices, the hexakis consists of 120 identical triangles and 62 vertices, and the celestial icosahedron consists of 9 intersecting rings spaced out and

at 45 degree increments. Each of the designs includes a thin, membrane-like skin that is draped over the frame to provide means of creating a vacuum. [1]

To date, the analysis and research of the Masters and PhD students at AFIT has not addressed the asymmetric effects caused by airflow around the VLTAV. The size constraint of the VLTAV is motivated by operationally being able to fit through a door frame in an urban environment, and the analysis of the structure has been conducted at the brink of buckling. The varying pressure observed due to airflow around the VLTAV could have resounding effects on the structural integrity of the VLTAV.

## 1.5    Lighter Than Air Vehicles

The first of the lighter than air vehicles took flight in 1783 produced by the Montgolfiere brothers in France. The balloon built by the Montgolfiere brothers produced lift by heating the interior air of the balloon to make the air inside the balloon less dense than the outside atmosphere [6]. Later in 1785, the first balloon filled with hydrogen flew from Dover to Calais. [7]

Many of the early lighter than air vehicles produced in the world resembled a nominally spherical shape as seen in Figure I-2. The reason for this spherical shape is evident in calculating the weight-to-buoyancy ratio of a body which is discussed in greater detail in section 6 of this chapter. With any air vehicle which used lighter than air gas to produce lift, this spherical shape took form by either heating the internal air in a hot air balloon or filling the balloon with a lighter than air gas such as helium or hydrogen. The internal lighter than air gas produces an internal pressure on the

ال_منارة للاستشارات

www.manaraa.com

structure of the balloon allowing for the structure to be constructed out of light-weight envelope material. [7]
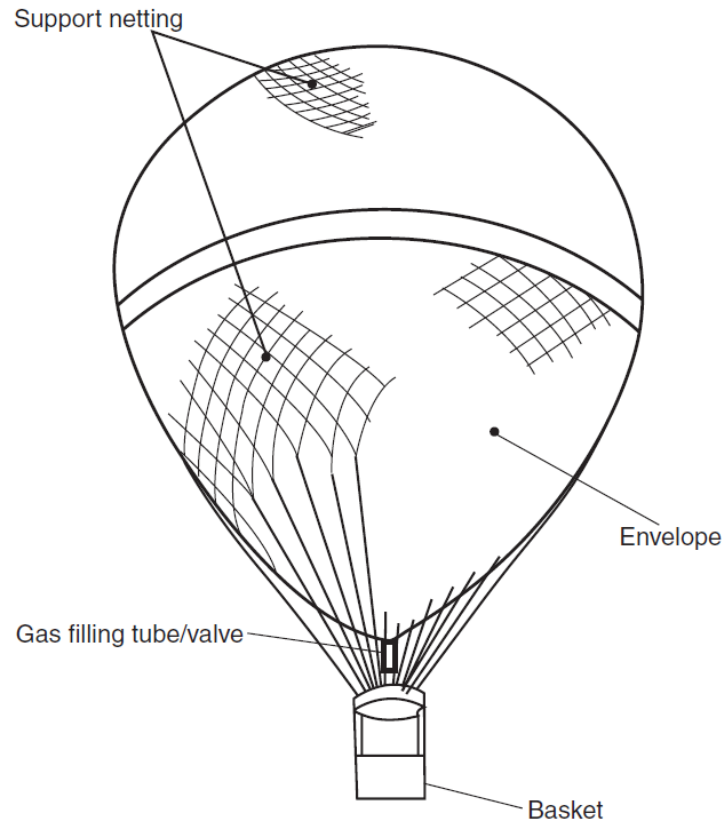


**Figure I-2. Early "spherical" pressure balloon** [7]

As shown in Table I-1, the lifting gases used for original lighter than air vehicle design are at best 9% as dense as the air surrounding the vehicle. Hydrogen maintains the superior density of the lifting gases at 9% the density of sea level air, but hydrogen also introduces the most safety concerns of the gases.

6

**Table I-1**. **Lifting gas properties (sea level)** [7]

| Gas | Density (kg m$^{-3}$) | Lifting force (N m$^{-3}$) | Lifting force (% hydrogen) |
|---|---|---|---|
| Air | 1.225 | | |
| Hydrogen | 0.108 | 11.0 | |
| Helium | 0.189 | 10.2 | 92.7 |
| Coal gas | 0.564 | 6.5 | 59 |
| Natural gas | 0.664 | 5.5 | 50 |
| Hot air | 0.88–0.98 | 3.4–2.4 | 31–22 |

Hydrogen was often chosen to provide vehicles lift because of the low density as well as the cost and abundance of the gas as compared to helium. Throughout World War I cities in the United Kingdom suffered bombardment from German hydrogen airships. The German hydrogen airships avoided many of the ground anti-aircraft defenses because of the heights they could reach; if the airships were hit by any anti-aircraft fire, several did not burn or explode due to the hydrogen cells on board. However, as the allies began to use incendiary ammunition, more of the hydrogen airships suffered more casualties due to hydrogen fires and explosions. The reason for these fires and explosions is credited to the low ignition energy of hydrogen as well as the high flammability of a mixture of hydrogen and oxygen which would be expected from a jet of hydrogen from a leak mixing with the external atmosphere outside of an airship. [8]

Due to the safety concerns associated with hydrogen as a lifting gas along with the relatively high density of other lifting gases, a solution for a vacuum lighter than air vehicle becomes very valuable. A vacuum or near vacuum has significantly lower

7

densities than any other lifting gas, and theoretically a vacuum lighter than air vehicle produces a weight-to-buoyancy ratio less than 1, providing lift in a cheaper and safer manner than other lifting gases. This is predicated on the assumption that materials are available to keep the structure of the vehicle intact. The next section will discuss the theory behind the weight-to-buoyancy ratio which allows LTAVs to float.

### 1.6  Weight-to-Buoyancy Ratio

According to Archimedes' Principle, "A body partly or completely immersed in a fluid is buoyed up by a force equal to the weight of the displaced fluid"[9]. This principle is the crux behind how LTAVs and, theoretically, VLTAVs operate. As shown in Figure I-3, Archimedes' Principle can be applied to a weight in water. Although, the weight sinks, a buoyant force is created equal to the weight of the displaced water. This force reduces the value on the scale due to the effective 3 lbs of force acting upward on the weight when submerged [10]. If the weight of the displaced water is greater than that of the weight of the object being submerged, then the object will float. This concept is known as a weight-to-buoyancy (W/B) ratio. If the weight-to-buoyancy ratio is less than 1, that is if the weight of the object is lighter than the weight of the displaced fluid, then an object will float [1].

8
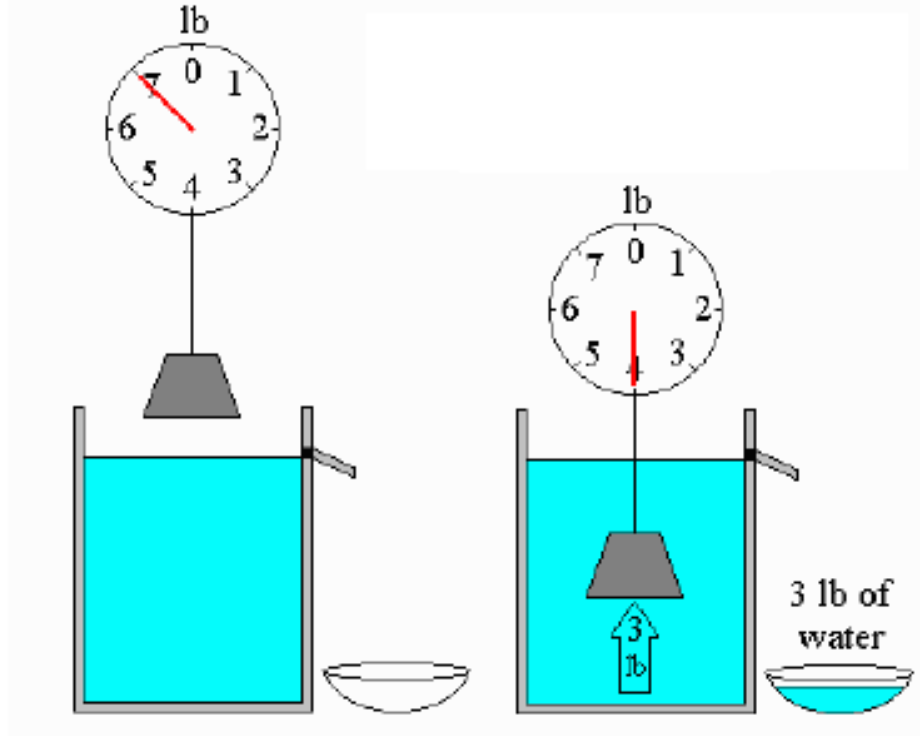
**Figure I-3. Archimedes' Principle illustrated with a 7 lb weight [1]**

The same concept is true in air as it is in water. A lighter-than-air vehicle

produces lift by displacing the atmosphere around it with a less dense form of fluid.

Historically, as discussed previously, LTAVs achieve a weight-to-buoyancy ratio of

less than 1 with lighter than air gases. Because these gases are less dense than air, the

weight of the air the vehicle displaces weighs more than the combination of the lifting

gas inside the vehicle plus the weight of the vehicle itself. Again, this concept is why

the production of a vacuum lighter than air vehicle could be so lucrative. If a structure

has an internal vacuum, there is no weight associated with an internal gas to add to

the vehicle's overall weight.

Although the W/B ratio of a vacuum lighter than air vehicle is ideal on the

surface, there are issues associated with creating an internal vacuum as opposed to

9

filling a structure with a lighter than air gas. Issues associated with an internal

vacuum as a means of reducing the W/B ratio include structural instability and

integrity. The pressure differential between the internal vacuum and the atmospheric

pressure outside of the structure cause an external load on the vehicle in the form of a

uniform pressure equal to that of the atmospheric pressure. In contrast, typical lighter

than air vehicles which use a lighter than air gas have internal pressure greater than

that of the atmospheric pressure allowing a simple membrane to restrain the air. The

external pressure associated with a VLTAV leads to the potential collapse or buckling

of the vehicle's structure. Structural integrity requirements call for an internal

structure in the vehicle that can withstand these loads without buckling or collapsing.

Therefore, the material used for constructing a VLTAV will be denser than the

material used for a traditional lighter than air vehicle because the internal structure

must withstand the external pressure loads. The next section describes three of the

structural geometries designed in past research. [2]

## 1.7    Previous Research and Structural Geometries

Through previous research at AFIT, three structural designs emerged to solve the

problem of structural integrity in a vacuum lighter than air vehicle. The ideal shape to

consider when minimizing a weight-to-buoyancy ratio is a sphere because a sphere

produces the most internal volume (vacuum) for the smallest surface area (structure,

i.e. weight) and consequently the most lift [1]. However, a perfect sphere shell would

not be able to withstand the external atmospheric pressure if its thickness is reduced

to a point where a weight-to-buoyancy ratio of less than 1 is achieved. Therefore, in

his thesis, Trent Metlen first introduced the idea of an icosahedron which is a

10

geodesic sphere that approximates a sphere using straight lines [11]. Next, Brian Cranston proposed, in his dissertation, the design of a hexakis icosahedron which would provide a closer approximation to a sphere compared to Melen's icosahedron. Along with the hexakis, Cranston also analyzed a celestial icosahedron structure which provided the closest approximation to a sphere to date.

The icosahedron that Metlen proposed was derived from a patent from Buckminster Fuller in 1951 in which Fuller designed a geodesic dome [12]. The icosahedron is a polyhedron with 20 equilateral triangles in which the vertices lie on the surface of an imaginary sphere. To create an internal vacuum, a membrane must be draped over the icosahedron frame in which the frame provides structural integrity for the lighter than air vehicle and the membrane provides a means to create the vacuum. Metlen's icosahedron, shown in Figure I-4, utilized an Ultra High Modulus (UHM) carbon fiber tube frame and a reinforced Mylar membrane draped over the frame for conducting his analyses. [11]

11
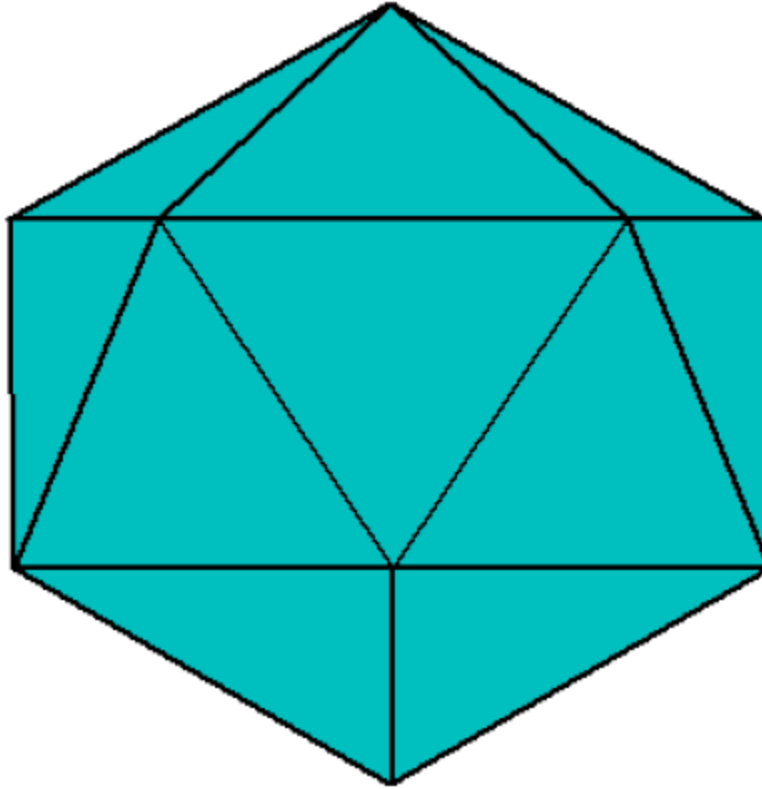
**Figure I-4. Metlen's icosahedron (geodesic sphere) representation** [11]

Brian Cranston later proposed the hexakis icosahedron because Metlen's icosahedron holds a significantly less internal volume compared to a perfect sphere, especially with large diameters. By increasing the diameter of the structure, the W/B ratio is reduced further compared to smaller diameters, therefore, this volumetric void is problematic. As a result, Cranston proposed a structure even closer in shape and volume to a sphere called the hexakis icosahedron. The hexakis icosahedron, shown in Figure I-5, has 120 faces and 62 vertices. [1]

12
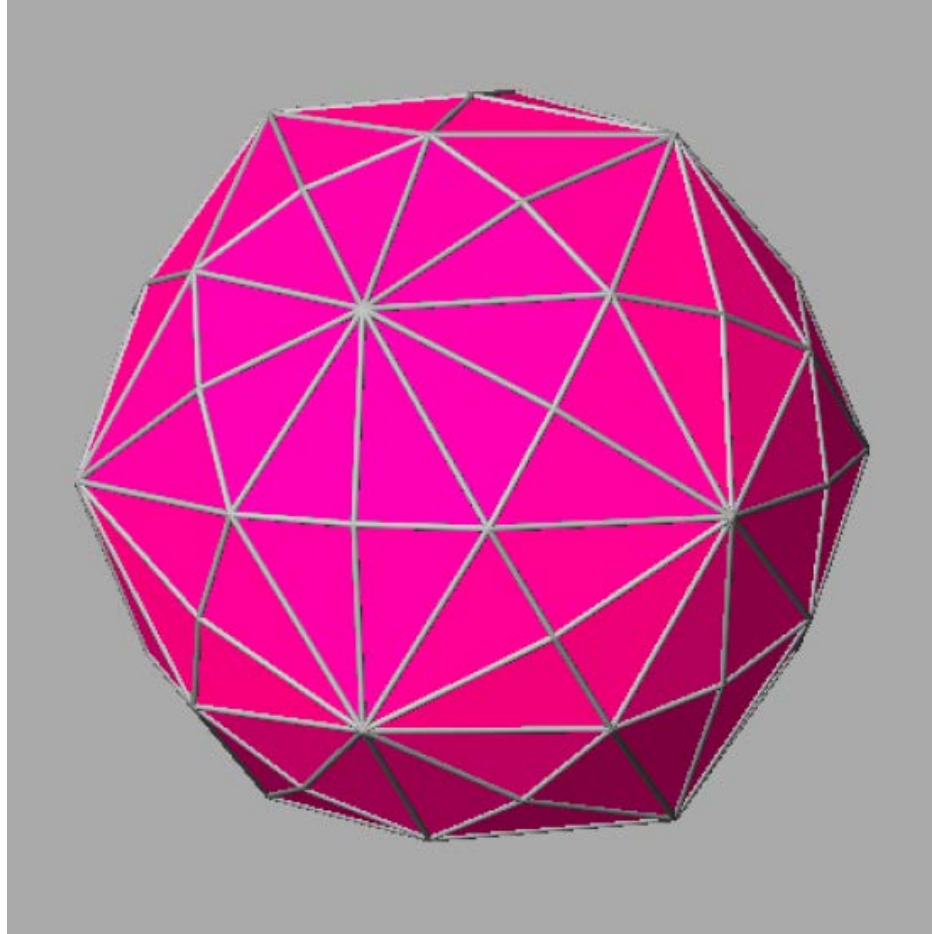
**Figure I-5. Cranston's Hexakis Icosahedron [3]**

Lastly, Cranston then proposed the most spherical design in the AFIT research so far, the celestial icosahedron. The celestial icosahedron design, shown in Figure I-6, consists of intersecting circular rings as opposed to the combination of straight rods in the previously mentioned icosahedron and hexakis icosahedron. Instead of flat, connected triangular faces, the celestial icosahedron had 9 intersecting rings revolved around each axis offset by 45 degrees. Cranston did not analyze the celestial icosahedron structure thoroughly, so Kyle Moore later optimized the structure for a minimum diameter which could still float given the materials used. [1]

13
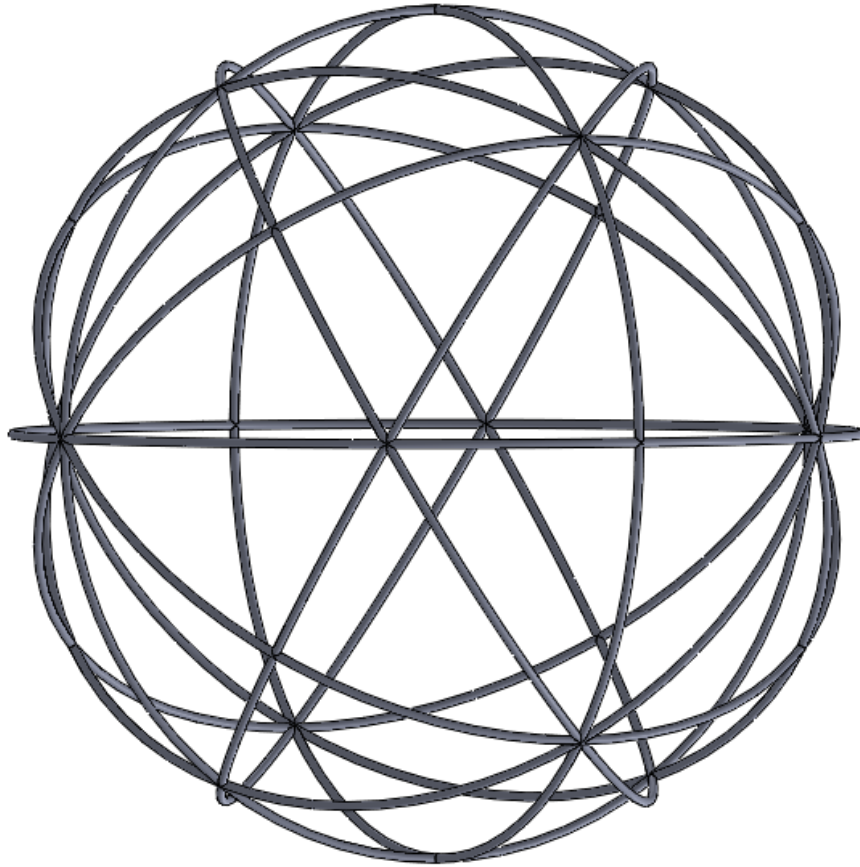
**Figure I-6. Celestial icosahedron frame in SolidWorks**

The icosahedron, hexakis icosahedron, and the celestial icosahedron designed by previous researchers to date have their own merit when it comes to the design of a vacuum lighter than air vehicle. While the celestial icosahedron provides the closest geometry to a sphere and therefore the most internal volume to be evacuated, the icosahedron and hexakis icosahedron provide more structural integrity because their members are straight and not curved. An aspect of design analysis which has not been taken into account yet in past VLTAV research is the aerodynamic effects of the geometric shapes when deformed under internal vacuum. Airflow around these

14

shapes will cause pressures and other aerodynamic phenomenon which have not previously been considered in the structural analyses of the VLTAV. Consequently, the purpose of this thesis is to provide the initial aerodynamic analysis which can be utilized to determine if the fluid-structure interaction of a VLTAV is a problem worth considering in design.

## 1.8    Overview

- Chapter I: Thesis objective, motivation, background, lighter than air vehicles, and previous research

- Chapter II: Assumptions, methodology, and theory associated with research

- Chapter III: Detailed methodology to include the finite element model, validation of test setup, stagnation pressure comparison, conversion of models, additive manufacturing, incorporating aerodynamic effects to structural analysis

- Chapter IV: Results and discussion to include validation of setup, stagnation pressure results, CFD comparison to wind tunnel data, structural analysis with aerodynamic effects

- Chapter V: Conclusions and recommendations

# II.  Theory

## 2.1    Chapter Overview

Although the idea of lighter than air travel was first introduced by de Terzi in 1670, with the idea of creating an internal vacuum in copper spheres, the first flights utilized the concept of a lighter than air vehicle (LTAV). Francesco Lana de Terzi had formulated the idea for a vacuum lighter than air vehicle (VLTAV), but due to the compressive stress of the outer atmosphere, the spheres collapsed.

Since de Terzi, the research of VLTAVs has not produced a physical prototype that floats with an internal vacuum. Although the research from past students at the Air Force Institute of Technology (AFIT) has not produced a working prototype, the analyses produced studying VLTAVs provides data to suggest that floating is possible with materials that may be available in the near future. The previous research from AFIT students analyzes three feasible design geometries that include an icosahedron, a hexakis icosahedron, and, most recently, a celestial icosahedron.

The analyses conducted on the different geometric structures of the VLTAV involved nonlinear-solution methods to characterize the displacements of the skin and the frame of a VLTAV when a ramped pressure is applied to the outer surface. The analyses used a pressure equivalent to that of sea-level pressure as a worst-case scenario. The analyses show that the VLTAV deforms when reacting to sea-level pressure as the internal air is vacuumed out. The deformations in the skin and frame have effects on the aerodynamics of the entire structure. The goal of this thesis is to determine the aerodynamic effects and discuss how the aerodynamic effects affect the already completed structural analyses.

16

This chapter addresses the assumptions, brief methodology, and theory behind the research conducted in this thesis. The theory behind the structural analysis tools as well as the aerodynamic experiments addressed in this chapter show the approach taken and give an understanding of the principles utilized in this work. The theory shall address finite element analysis (FEA), nonlinear structural analysis, aerodynamics of a sphere, pressure measurement technique, drag measurement technique, and Reynolds number scaling.

## 2.2    Assumptions

In order to conduct the research associated with this thesis, there are several assumptions that were made that must be taken into consideration. The first assumption is that the deformation of the VLTAV due to the aerodynamic effects of the airflow around the body are not large enough to change the aerodynamics significantly. Next, this thesis assumes, as has been assumed in other theses, that the materials utilized are able to be manufactured into the geometries analyzed within the thesis.

The first assumption addresses the problem of conducting wind tunnel and CFD analysis with multiple deformed models. With the assumption that deformations due to aerodynamics are small compared to the deformation brought about by applying sea-level pressure to the outer surface of the membrane on the structure, the research conducted utilizes a single deformed model for all velocities analyzed. This assumption is tested and addressed in later sections with the stagnation pressure comparisons.

17

The second assumption assumes the materials used in structural analyses can be readily manufactured in the geometries consistent with the analysis. This assumption is more reality everyday as manufacturing techniques improve. The capabilities of major graphene manufacturers include producing graphene sheets in thickness on the order of micrometers to hundreds of nanometers which is on the same order as the analysis conducted for this thesis. Also, according to Ren and Cheng, "Bluestone Global Tech is a USA-based CVD graphene manufacturer established in 2011 that produces graphene films on copper, $SiO_2$/Si wafers and flexible polyethylene terephthalate (PET), and its largest film produced on copper that is available is 24 x 300 $inch^2$. [13]

Similarly, the manufacturing technology of carbon nanotube composites can be manufactured with the same thickness as the thin walled tubes used in the structural analysis for this thesis. As an example, Cheng et al. utilized tensile test samples cut from carbon nanotube composite panels with a thickness of 0.3mm [14]. Also, it has been shown that Multi-walled carbon nanotube-sheet-reinforced bismaleimide resin nanocomposites are produced at a thickness of 60µm for dog-bone shaped specimens which retain the same material properties as used in this analysis [15]. Moore, for his analysis, utilized a carbon nanotube composite thickness of 0.2 mm for his beam thickness.

Therefore, the technology exists to manufacture the materials on the scale needed to represent the analyses. However, it is still assumed that the graphene and carbon nanotube composite materials are able to be shaped into the geometry of the celestial

18

icosahedron. This may or may not be possible with the small scale thicknesses necessary to physically build the structural model.

## 2.3    Methodology

The research conducted for this thesis seeks to gain an understanding of the relationship between aerodynamic and structural analyses for the celestial icosahedron VLTAV. By understanding this relationship, the determination can be made on whether aerodynamic effects must be considered for future analyses and designs. The research includes conducting structural analysis utilizing finite element methods, conducting CFD analysis of the celestial icosahedron in collaboration with Wright State University, and conducting wind tunnel experiments to determine the aerodynamic effects of a deformed VLTAV and to validate CFD results.

A structural analysis of Moore's minimum diameter model is conducted to produce a deformed VLTAV which can be employed to understand the aerodynamic effects of the deformed shape. In order to gain confidence in the wind tunnel data acquired, before conducting experiments with the deformed shape, wind tunnel experiments were conducted with a perfect sphere to compare to analytical data available for this sphere. If the data from the wind tunnel experiments on a perfect sphere correlate well with the analytical data, then the experimental set up is validated. Also, to assure the quality of the first assumption in the previous section, a structural analysis was conducted based on a scenario of applying a stagnation pressure to one hemisphere of the celestial icosahedron to determine the difference in displacements between a stagnation pressure hemisphere and a sea-level pressure only hemisphere.

19

Once confidence is built in the methods of analysis and testing via the activities described in the previous chapter, the deformed celestial icosahedron shall be analyzed to determine if the aerodynamics significantly affect the stresses which the VLTAV experiences. Figure II-1 illustrates the process used to make the determination of the interaction between the aerodynamic and structural analyses.



**Abaqus Structural Analysis**
- Sea-level pressure
- Minimum diameter model (Moore)

**Solidworks Import**
- Convert deformed Abaqus mesh to point cloud
- Generate solid from point cloud

**Scale to 8"**
- Structure scaled to accommodate wind tunnel
- Proportional scaling used

**Wind Tunnel and CFD analysis**
- Compared to validate aerodynamic results

$$Re = \frac{\rho VD}{\mu}$$

**Scale aerodynamic results**
- Pressures used for appropriate wind speeds based on Reynolds Number

**Run Abaqus structural analysis with aerodynamic pressures**
- Fluid-Structure interaction

**Figure II-1. Interaction between aerodynamic and structural effects**

## 2.4    Structural Analysis

The structural analysis conducted for this thesis is consistent with the structural analysis conducted previously by Kyle Moore. Moore utilized the celestial

20

icosahedron frame which consists of the nine intersecting tubular rings rotated at 45 degrees about each access with a membrane surrounding the internal frame [1]. The Abaqus Quasi-Static Nonlinear analysis is used due to large deformations in the structure which come about from utilizing a thin membrane of graphene and thin walled tubes of carbon nanotube material properties. The large deformations expected in the analysis lead to the possibility of nonlinear geometry while the possibility of entering the plastic regime of the material allows for the possibility of nonlinear material behavior [16].

### 2.4.1    Finite Element Analysis

FEA is a numerical method for solving field problems to include heat transfer, stress analysis, and magnetism among others [17]. As stated previously, the finite element model for this thesis employs Abaqus as the tool for running the finite element analysis of the celestial icosahedron design. For a finite element simulation, the first thing that must be done is to discretize the structure to be analyzed. The matrices which make up the fundamental equation for finite element analysis are indexed based on the nodes within a structural analysis. [18]

Each element within a finite element model has 5 different characteristics to include family, degrees of freedom, number of nodes, formulation, and integration [18]. It is up to the modeler to determine the correct selection in each of these categories. A major distinction for the family is the geometry of the element. As an example, for the celestial icosahedron analysis, the frame should be made of beam elements because the geometry of a beam or truss are ideal for a rib, but trusses cannot handle bending so beams are the most suitable candidate. A membrane

21

element is the logical choice for the graphene membrane since the thickness is relatively small and the geometry is most closely related to the membrane element. Figure II-2 and Figure II-3 show the elements used in the analysis of the celestial icosahedron VLTAV.
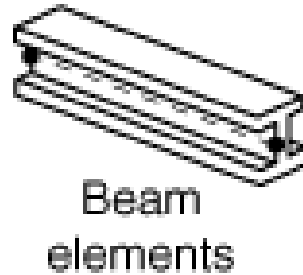


**Figure II-2. Generic beam element which are used for frame** [18]
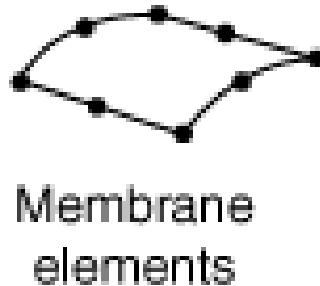


**Figure II-3. Generic membrane element which is used for skin** [18]

The degrees of freedom associated with an element include translation (displacement) and rotation for each node in each direction for the majority of stress/displacement simulations. The number of nodes on an element determines the interpolation function used for the element. For example, an element with two nodes on one edge would use a linear interpolation function for that edge while an element

22

with three nodes would use a quadratic interpolation function for that edge. The formulation of an element relates to the mathematical theory which will be used to solve the simulation whether that be Eulerian or Lagrangian among others. Integration is used to integrate material response over the volume of each element using numerical techniques. [18]

For the purposes of the structural analysis in this thesis, the frame of the celestial icosahedron is constructed of B31 beam elements and the skin is modeled using M3D4R membrane elements. B31 is a Timoshenko beam in three dimensional space with a linear interpolation function (i.e. 2 nodes). The M3D4R membrane element is a three-dimensional 4-node membrane element with reduced integration. Figure II-4 and Figure II-5 show an illustration of the B31 element and the M3D4R element respectively [1].
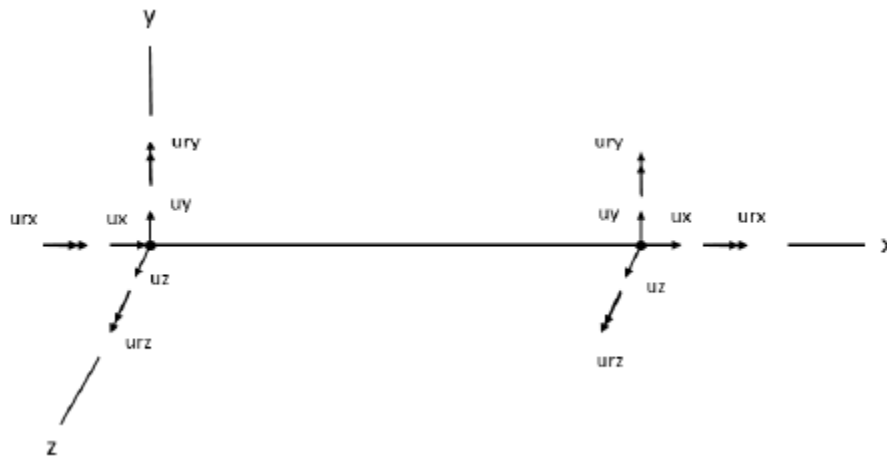


**Figure II-4. B31 beam element [1]**

23
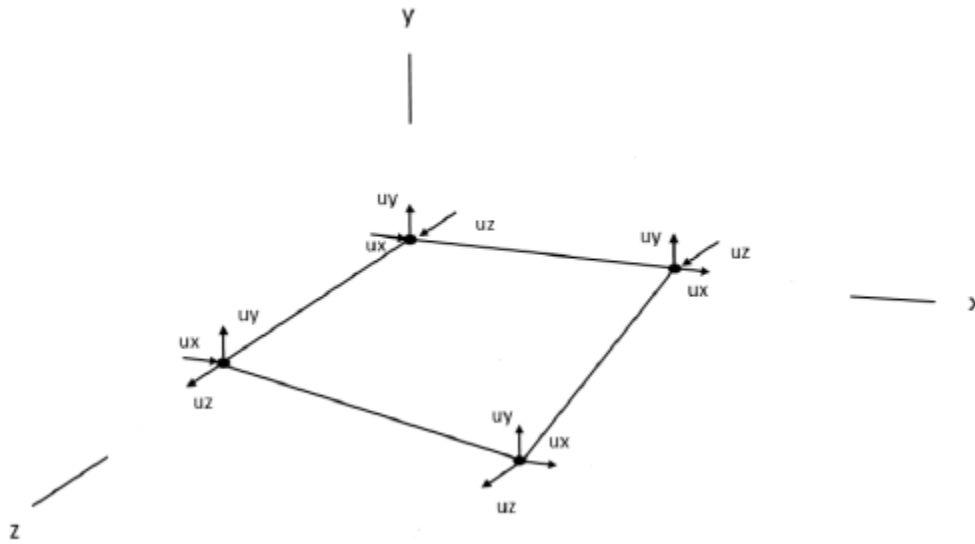
**Figure II-5 . M3D4R membrane element [1]**

### 2.4.2    Nonlinear Analysis

A nonlinear analysis is used for the structural analysis of the celestial icosahedron

VLTAV design since the expectation is to have large displacements and/or rotations

as the structure withstands atmospheric pressure. Nonlinear analysis uses numerical

methods in order to iteratively calculate the displacement of element nodes to find the

correct value [19]. The equations are solved iteratively for the correct displacement

value and is dependent upon the type of nonlinear method being used. The iterations

are terminated once a tolerance is met, which could be on a value for strain $\varepsilon$, for a

convergence criterion. The convergence criterion is very small for terminating the

iterative calculations [19].

Abaqus utilizes the Newton-Raphson method for calculating nonlinear structural

analysis problems. In order to find a solution to a nonlinear problem, Abaqus

incrementally increases the load over delta a time step and solves for an equilibrium

24

configuration after each of the steps. For each increment, the solver iterates through the calculation to attempt to find the equilibrium configuration. [18]

The Newton-Raphson method in general is described by the iterative algorithm found in Equation (1). This method is used to solve a nonlinear equation through iterations. This method can be expanded into the solution of a nonlinear system of equations which is useful for FEA. The method provides a means of solving nonlinear equations through linear means at very small increments. [20]

$$x_{i+1} = x_i - f(x_i)/f'(x_i) \qquad (1)$$

The first iteration in a load increment is shown in Figure II-6. The solver uses the structures original stiffness, $K_0$, based off of the configuration at $u_0$ to find a correction value $c_a$ to update the new configuration of the structure $u_a$ [18]. Abaqus then forms a new stiffness for the new configuration, $K_a$. Based off of this new configuration, Abaqus updates the internal load, $I_a$, and the difference between the applied load, $P$, and the internal load is found as the residual force, $R_a$ [18]. If the residual force was 0, then the point $a$ on the figure would be on the nonlinear curve. Therefore, Abaqus utilizes this residual force as a convergence criteria for the equilibrium solution for this increment. If the residual force does not meet a tolerance value (default to 0.5% of force in the structure), the solver will continue to iterate until an equilibrium solution is found. The equilibrium configuration, once converged, is $u_a$ [18].
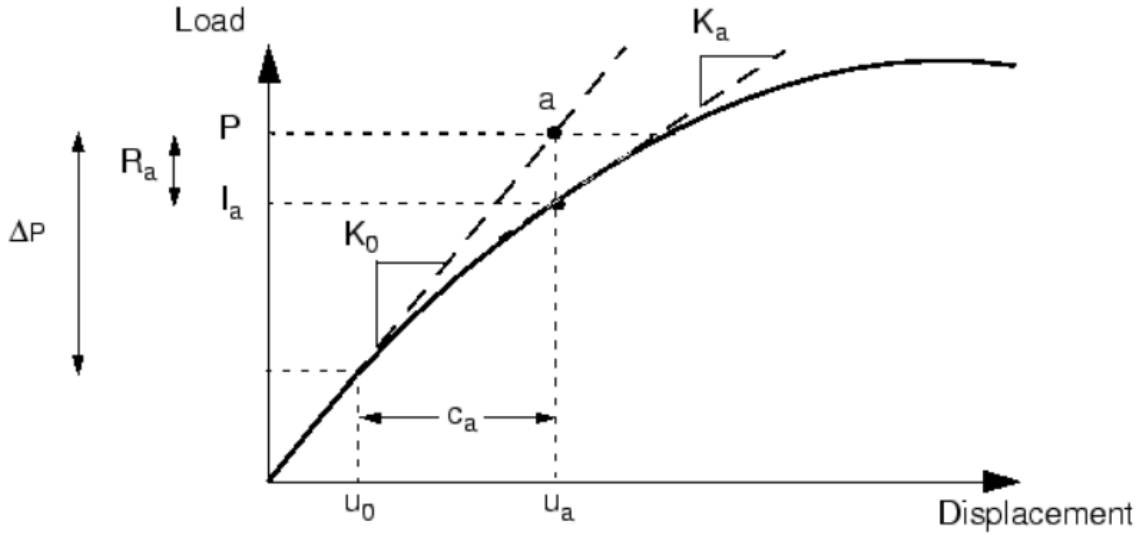
**Figure II-6. First Iteration in an Increment** [18]

In order to combat any issues of convergence due to instability within the

analysis, the Abaqus solver allows for the use of a feature called automatic adaptive

stabilization. Basically this feature within the nonlinear solver uses the aid of artificial

damping. If the stabilization method is adaptive, the damping value can vary spatially

or temporally as an analysis is run. For the case of this research the damping value is

varied temporally. The variance of the artificial damping within the model is

dependent on the convergence history of the solution. If convergence is an issue due

to instabilities within the structure or rigid body modes, the analysis tool will increase

the damping factor in order to try and combat these instabilities. [21]

### 2.5 Aerodynamic Analysis

The purpose of this thesis is to understand the relationship between the

aerodynamic and structural analyses to determine whether aerodynamic effects must

be taken into consideration in future structural analyses and designs for the VLTAV.

26

In order to understand the aerodynamic data obtained from experiments and computational analyses for better application in structural analysis, the theory behind the experiments and analyses must be understood. This section addresses the aerodynamics of a sphere for assistance in validating the aerodynamic test setup. This section also addresses the pressure and drag measurement techniques used in collection of data, and this section addresses scaling the flow inside the wind tunnel using Reynolds number.

### 2.5.1   Aerodynamics of a Sphere

Before conducting aerodynamic analysis of the deformed celestial icosahedron model, the test setup planned for the analysis must be validated against a known experimental scenario. Due to the close geometric shape of the deformed celestial icosahedron VLTAV to a perfect sphere, the determination was made to validate the test setup for wind tunnel analysis with aerodynamic data associated with a perfect sphere. The theory and analytical data available for flow around a sphere, therefore, must be understood.

Due time constraints, the test setup is validated against data available for the drag coefficient of a sphere in uniform flow. When an object is placed in a moving fluid, or moves through a stationary fluid, a force is exerted on that object. The force exerted is in the direction of relative motion of the object to the fluid producing a force referred to as drag. This drag force is dependent upon the size of the body, the fluid velocity, the fluid density, and the fluid viscosity [22]. The correlation for drag, or the dimensionless drag coefficient, in flow for a sphere is a fundamental problem in fluid flow calculations [23]. Morrison provides a data correlation between the drag

27

coefficient of a sphere and the Reynolds number up to turbulent flow. The Reynolds number is a ratio between the inertial forces and viscous forces of a fluid. The Reynolds number was first introduced in 1883 and is discussed further in the section on Reynolds number scaling. The equation below shows the data correlation for drag coefficient of a sphere as a function of Reynolds number.

$$C_D = \frac{24}{Re} + \frac{2.6\left(\frac{Re}{5.0}\right)}{1 + \left(\frac{Re}{5.0}\right)^{1.52}} + \frac{0.411\left(\frac{Re}{2.63x10^5}\right)^{-7.94}}{1 + \left(\frac{Re}{2.63x10^5}\right)^{-8.00}} + \frac{0.25\left(\frac{Re}{10^6}\right)}{1 + \left(\frac{Re}{10^6}\right)} \quad (2)$$

The use of this equation is not recommended above a Reynolds number of $10^6$ according to Morrison, but is an excellent means to predict the drag crisis range of Reynolds number depicted in Figure II-7.

28

$$C_D = \frac{24}{Re} + \frac{2.6\left(\frac{Re}{5.0}\right)}{1 + \left(\frac{Re}{5.0}\right)^{1.52}} + \frac{0.411\left(\frac{Re}{2.63 \times 10^5}\right)^{-7.94}}{1 + \left(\frac{Re}{2.63 \times 10^5}\right)^{-8.00}} + \frac{0.25\left(\frac{Re}{10^6}\right)}{1 + \left(\frac{Re}{10^6}\right)}$$
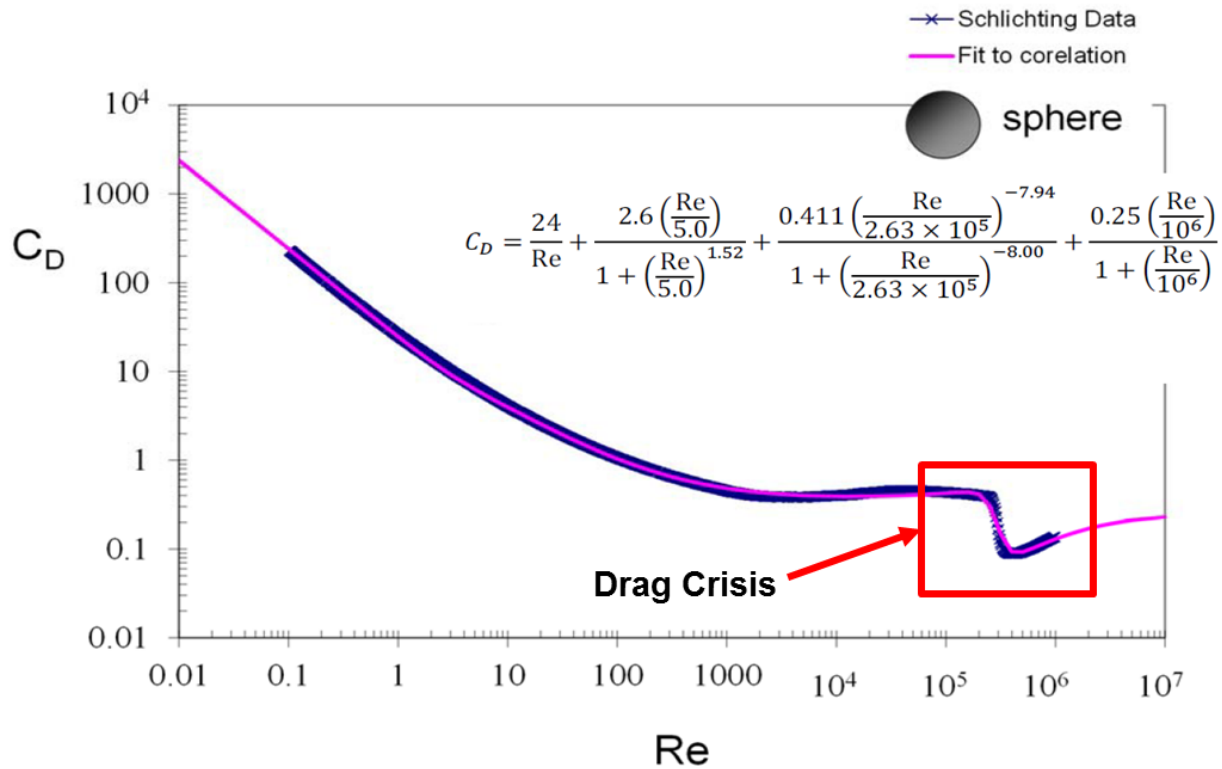
**Figure II-7. Drag Coefficient versus Reynolds number for Schlichting experimental data and the Morrison fit to correlation data** [23]

This data is utilized in later sections to compare experimental data for the drag on a sphere with analytical data.

### 2.5.2   Data Acquisition Techniques

The two data sets acquired for this thesis within the wind tunnel are the drag data and the pressure data associated with pressure at the surface of the model. The drag data is not only utilized to validate the test set up with the perfect sphere scenario, but it is also compared to the CFD results for the deformed VLTAV for comparison of experimental and analytical results. The pressure data acquired from the deformed VLTAV model is employed to compare to the pressure data acquired from CFD analysis.

29

The drag data for the perfect sphere as well as the deformed VLTAV is captured via an internally mounted force balance which is inserted into the model for mounting within the wind tunnel. Here, the purpose of the force balance is to collect the drag data through the axial force component. It also supports the weight of the model, with weight registered via the normal force component. Figure II-8 shows the perfect sphere model mounted in the wind tunnel using the force balance.

The drag data produced from the wind tunnel experiments must be corrected based on solid body blockage in the wind tunnel. Due to the fact that the cross sectional area of the sphere is $0.0729 \ m^2$ and the cross sectional area of the test section in the wind tunnel is $0.880 m^2$, the percent blockage is approximately $8\%$. According to West and Apelt, "For blockage ratios less than $6\%$, it is shown that the effects of blockage on pressure distribution and the drag coefficient are small and that the Strouhal number is unaffected by blockage" [24]. The Strouhal number (St) is a dimensionless number describing the oscillating flow mechanisms around an object. For this thesis, the research does not look at dynamic oscillations and therefore the Strouhal number is not as great of a concern.
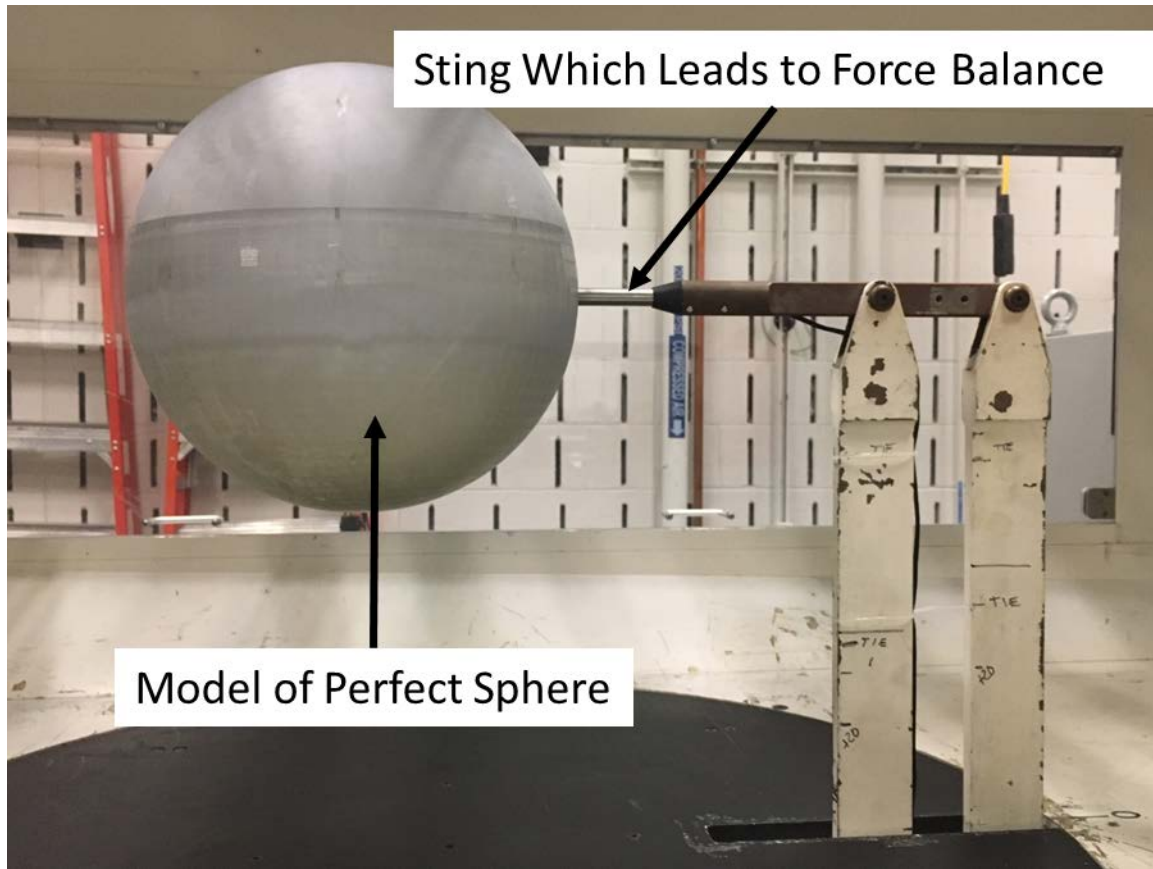
**Figure II-8. Wind tunnel setup for perfect sphere model**

The force balance is rated at 22.67 kg and 11.34 kg for the normal and axial forces about the moment center respectively. Through using the data correlation equation, the maximum drag force expected for a perfect sphere with the same diameter as the experimental model is approximately 0.9 kg which is below the rating of the force balance. The weight of the model, once support material was removed, was approximately 6.8 kg which also fell within the rating of the force balance. Therefore, the force balance used was able to accommodate both force components. The normal and axial force directions for the force balance are indicated in Figure II-9.

31
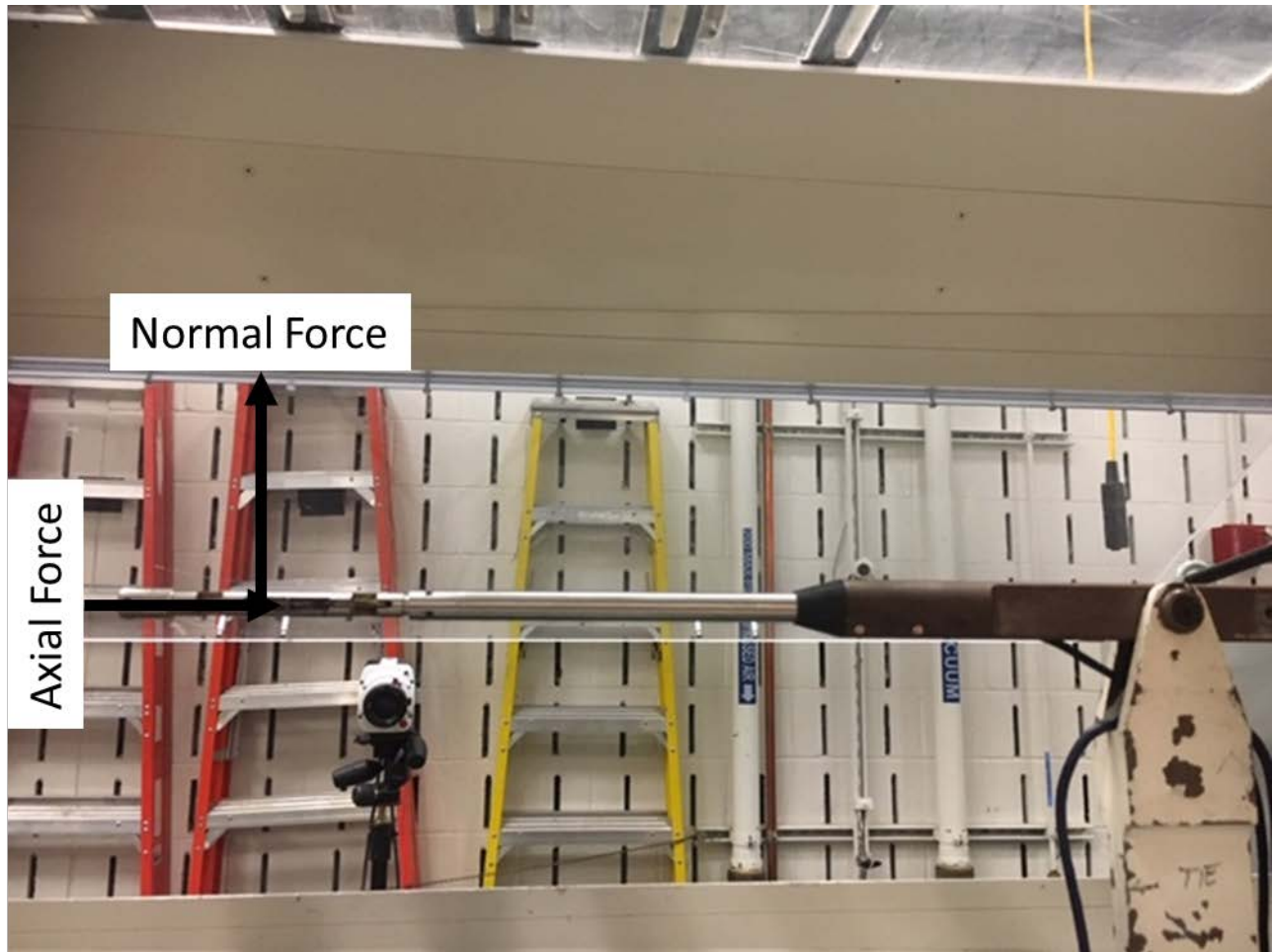
**Figure II-9. Axial and normal directions for force balance**

The pressure acquisition system for the deformed VLTAV model utilizes a
miniature electronic pressure scanner. The unit is a miniature electronic differential
pressure measurement system. The pressures reported from the CFD analysis
conducted by Wright State University were compared to the specifications of the
pressure scanner to ensure that the pressures expected were in the range of the
scanner. The maximum pressure reported from the CFD report was approximately 3
KPa at a velocity of 58.1152 $\frac{m}{s}$ [25]. According to the data sheet for the pressure

32

scanner, the range is $\pm15$ psid (or 103 KPa). Psid is the differential pressure referenced to a pressure that than ambient atmospheric pressure. In the case of these wind tunnel tests, the reference pressure was measured just upstream of the test section. Therefore, the maximum differential pressure expected is within the specifications of the pressure scanner. Also, the static accuracy of the pressure scanner is accurate down to $\pm0.03$ % of the full scale pressure range or approximately $\pm30.9$ Pa [26]. Figure II-10 displays the interfaces and layout of the pressure scanner used for pressure data acquisition within the wind tunnel experiments. The "Measurement Sources" are the tubulation to which the tubes from the model's pressure ports are connected. The "Run Reference Source" is the tubulation to which the reference pressure at the tunnel throat is connected to the scanner. The scanner utilizes silicon piezoresistive pressure sensors for each port. There is a separate sensor for each of the measurement sources. [26]
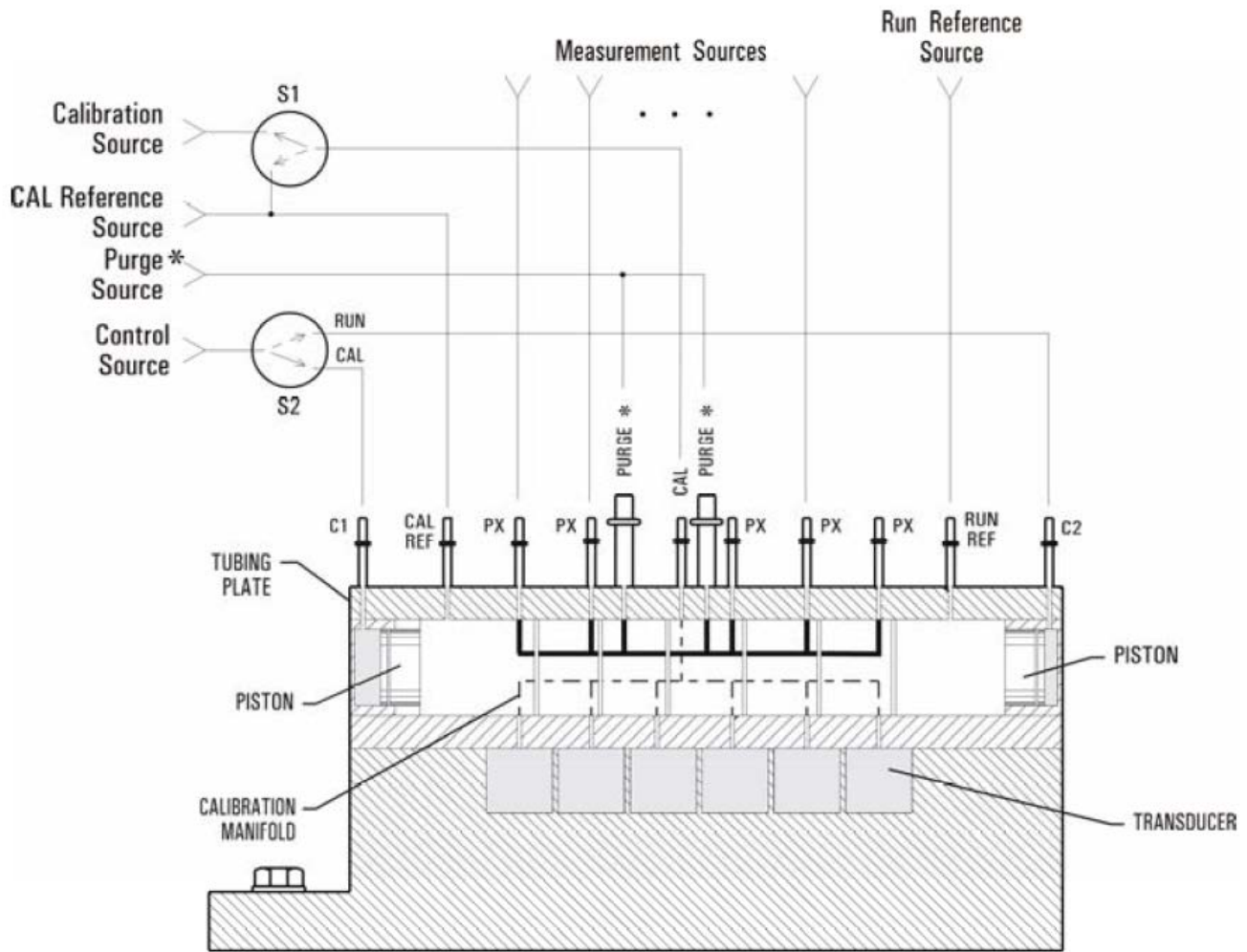
**Figure II-10. Pressure scanner depiction and interfaces**

### 2.5.3 Computational Fluid Dynamics (CFD)

The experimental data acquired from the wind tunnel analyses, to include the drag
and pressure data, is compared with the same data from CFD analyses for both the
perfect sphere scenario and the deformed VLTAV structure. Wright State University,
in collaboration with this research, provided the CFD analysis and results via

34

consulting reports. Ultimately, the data received from the CFD analysis produces a pressure field file which can be imported into the structural analysis software to gain an understanding of the fluid-structure interaction.

The CFD analysis is conducted with the ANSYS fluent software. The students at Wright State, in the first report, demonstrated their CFD capabilities with simple test cases of airfoils and spheres [25]. The analysis utilized far field boundaries at least 15 chord lengths from the structure in order to reduce boundary affects. Also, the mesh was refined near the structure surface and downstream of the surface becoming coarser in the free stream regions where flow gradients are small. The NACA 0012 airfoil was used by Wright State University to show the students capabilities first in the 2-dimensional regime before extending their analysis into the 3-dimensional regime. Figure II-11 shows the results of the 2-dimensional NACA airfoil which validates aspects of the students' capabilities. [25]
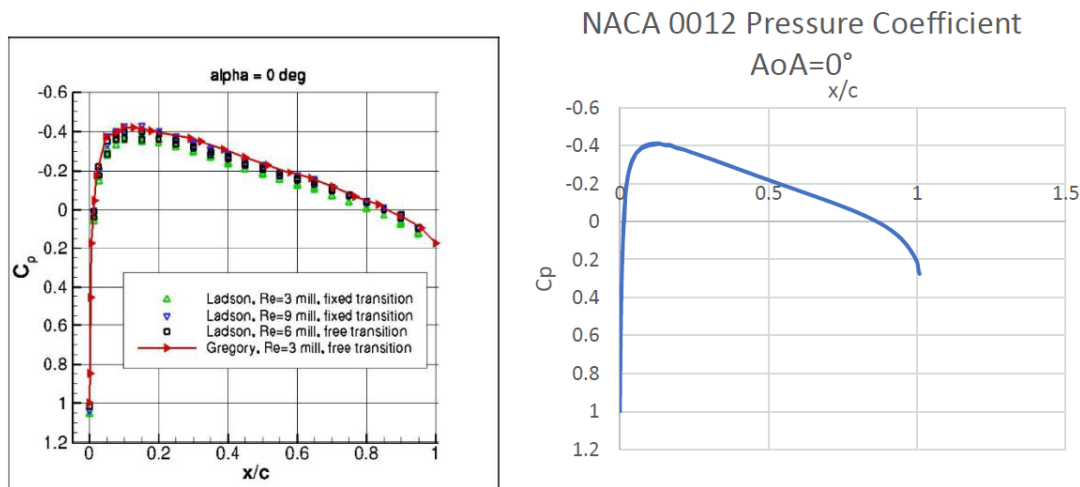


**Figure II-11. NASA experimental results (left), ANSYS fluent generated results (right)**

35

The analysis utilizes the transition based $k$-$kl$-$\omega$ turbulence model. The model consists of three equations and is an eddy-viscosity type and includes transport equations for turbulent kinetic energy ($k_T$), laminar kinetic energy ($k_L$), and inverse turbulent time scale ($\omega$). These three variables represent the $k$-$kl$-$\omega$ within the model's name. According to the ANSYS Theory Guide, the $k$-$kl$-$\omega$ turbulence model "is used to predict boundary layer development and calculate transition onset. This model can be used to effectively address the transition of the boundary layer from a laminar to a turbulent regime" [27]. For the case of the perfect sphere, the CFD analysis was conducted with the inlet, side, bottom, and top boundaries 2.5 diameters away from the sphere and the trailing boundary 7.5 diameters downstream, with a diameter of 0.3048 m for this case. The grid consisted of 503,740 elements which followed the same convention of the airfoil with coarser far field elements up to 0.762 m and finer elements closer to the surface of the sphere at approximately 0.4572 mm. The educational version of Fluent would not allow for more than 512,000 elements. Figure II-12 illustrates the sphere's position in reference to the boundaries within the computational domain.
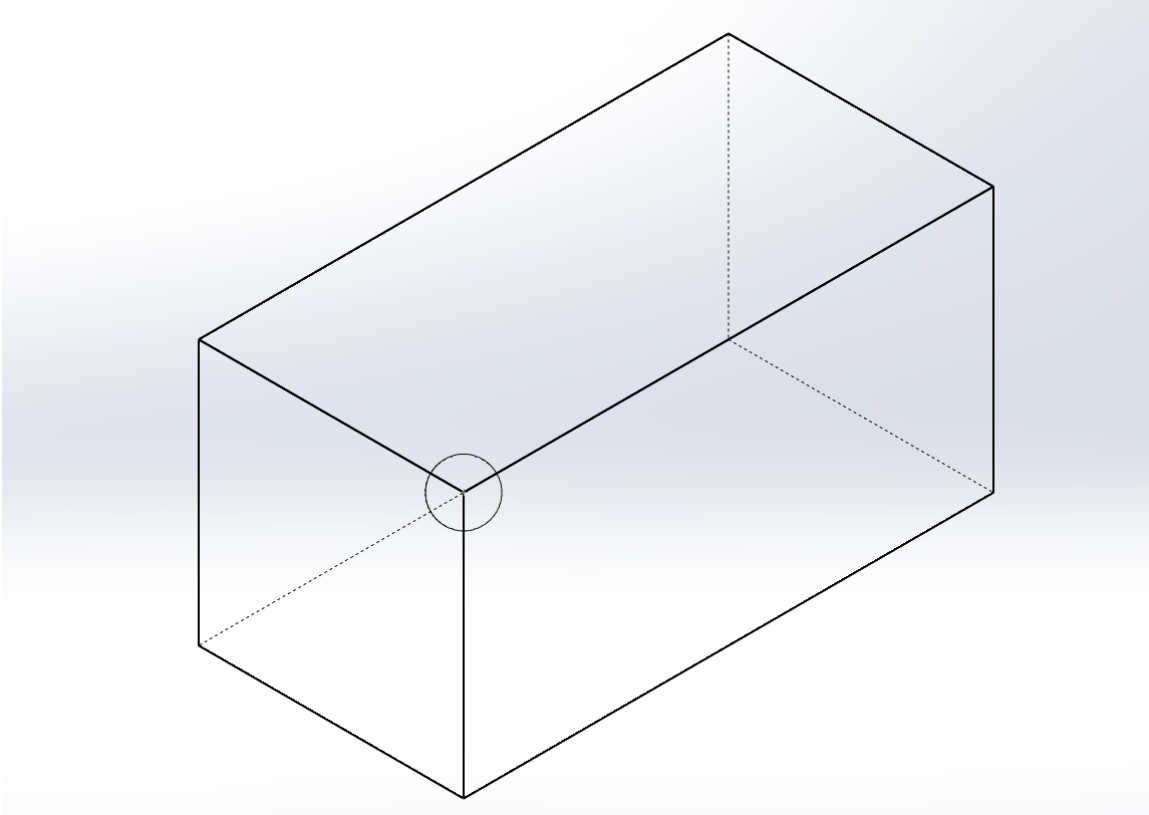
**Figure II-12. Sphere computation domain**

A similar approach was taken in the case of the deformed VLTAV as the perfect sphere scenario. The structure used within the CFD analysis was provided to Wright State based off of the same model that was additively manufactured at the Air Force Institute of Technology for wind tunnel analysis to ensure the data from the CFD analysis should be comparable to wind tunnel results. Within Chapter III on research methodology, the process for converting the structural analysis mesh into a solid body model is explained in greater detail. Both the CFD analysis and the wind tunnel tests were conducted using the geometry exported from the structural analysis mesh. In contrast to the CFD analysis for the perfect sphere, however, the analysis conducted

37

for the deformed VLTAV consisted of not only a fine mesh surrounding the surface of the model, but a fine mesh on the surface as well. The purpose of this approach is to attain pressure data at points on the surface. The point cloud of pressure data can be compared to wind tunnel data and utilized for the load in the structural analysis.
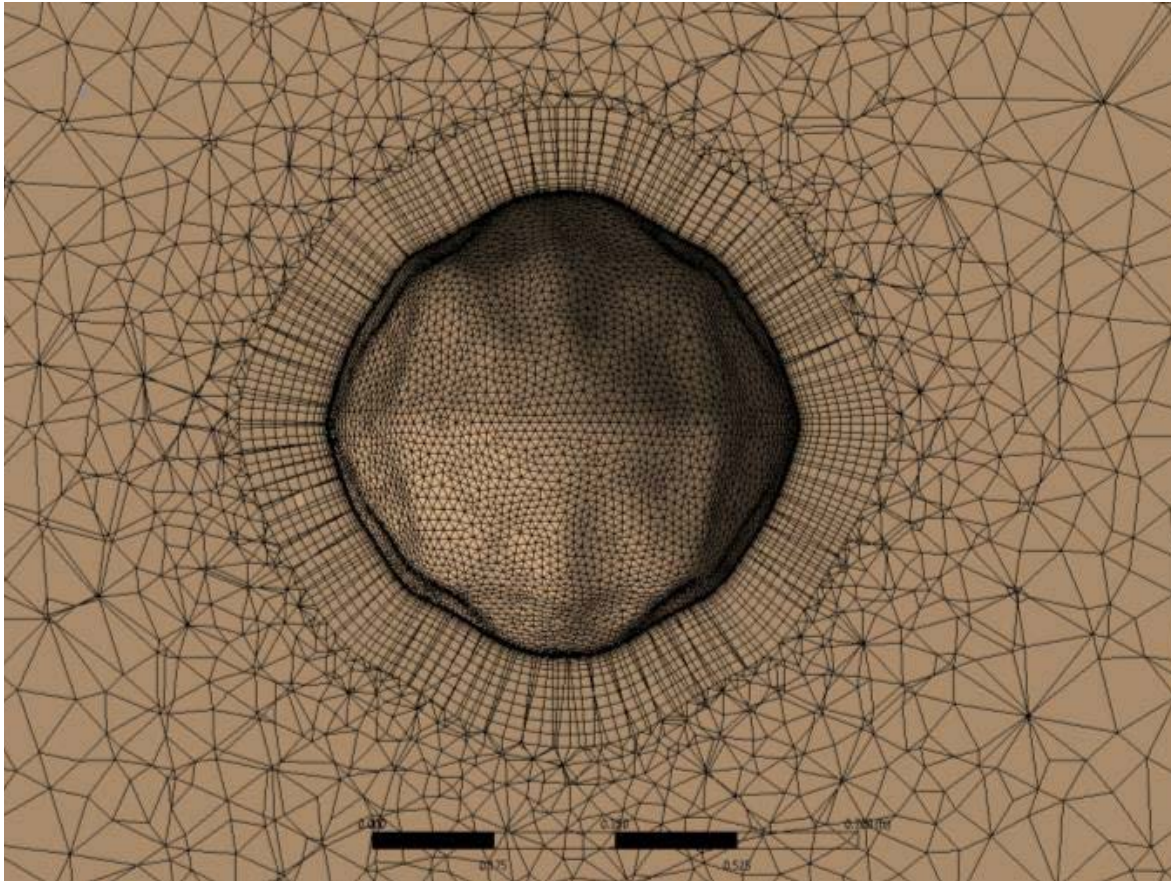


**Figure II-13. Near field mesh around/on the surface of the evacuated sphere**

### 2.5.4   Reynolds Number Scaling

Since the diameter of the model for aerodynamic analysis must be smaller than what is a feasible diameter to maintain a weight-to-buoyancy ratio of less than 1, a scaling factor for the wind speed in the tunnel must be incorporated to maintain

consistent aerodynamic effects. If the small scale model is kept at the same Reynolds Number as the larger diameter model, then the aerodynamic effects can be related. Reynolds Number is calculated via Equation (3) where $\rho$ is the mass density of the airflow, $u$ is the velocity of the airflow, $L$ is the characteristic length of the object being tested, and $\mu$ is the viscosity of the airflow. [28]

$$Re = \frac{\rho u L}{\mu} \qquad (3)$$

As is evident from Equation (3), if the characteristic length is reduced, one of the other parameters must be changed in order to maintain the same Reynolds Number for both the larger and smaller diameter celestial icosahedrons. The method for maintaining consistent Reynolds Numbers in this thesis involves increasing the velocity of the airflow in the wind tunnel. The increase in airspeed for the smaller model as compared to the larger model will counteract the decrease in diameter within Equation (3).

If the Reynolds number is held constant between the larger diameter structural analysis model and the smaller diameter wind tunnel model, then the pressure coefficients and the drag coefficients from the wind tunnel model can be related to the larger diameter structural analysis model. In order to apply this relationship, the deformed structural model must be uniformly proportionally scaled to the wind tunnel diameter. For example, if the maximum displacement of the 0.7576 m diameter structural analysis model is 0.038 m, then the maximum displacement of the 0.2032 m wind tunnel model shall be 0.010 m. This relationship is shown in the equation below.

$$\frac{D_s}{U_s} = \frac{D_w}{U_w} \rightarrow \frac{0.7576m}{0.038m} = \frac{0.2032m}{0.010m}$$

(4)

Where $D_s$ and $D_w$ are the diameters of the structural and wind tunnel model respectively, and $U_s$ and $U_w$ are the maximum displacements of the structural and wind tunnel models respectively. The linear transformation of the structural model shrinks to the size of the wind tunnel model by a scale factor that is the same in all directions. Figure II-14 provides a depiction of the linear scaling taking place.
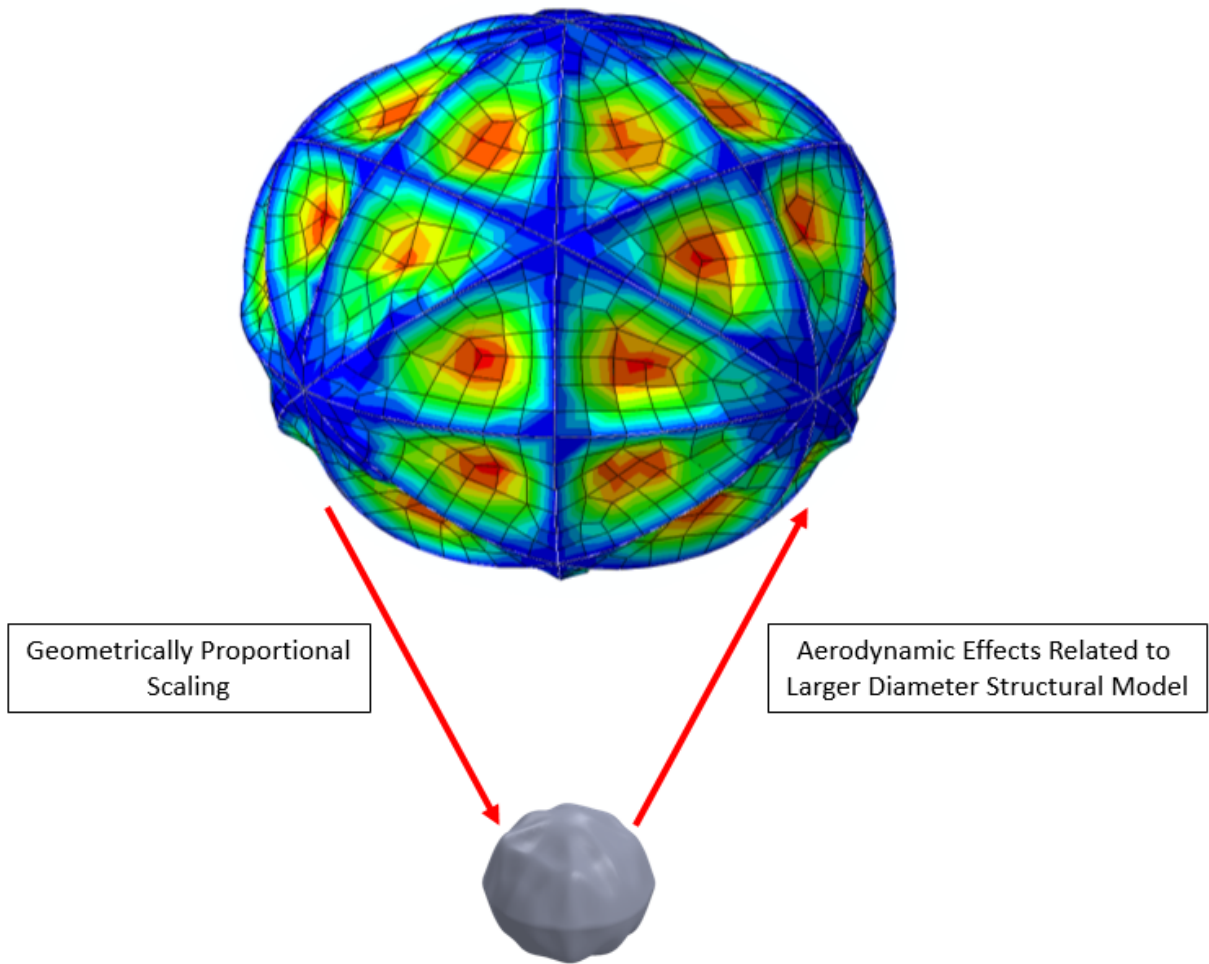


**Figure II-14. Depiction of scaling between structural analysis model and wind tunnel model**

40

## 2.6 Summary

In this chapter, the assumptions and methodology are addressed for the research associated with this thesis. The assumptions include negligible deformations to the model due to aerodynamic effects as compared to load due to the vacuum and this thesis assumes the availability and manufacturability of the materials used in analysis. The methodology section provides an introduction to the succeeding chapter in which the methodology is discussed more in depth.

This chapter also presents the basic theory behind the methods used for this research. The structural analysis theory included high level theory associated with finite element analysis as well as an introduction into nonlinear analysis techniques. The theory sections also included aerodynamic analysis. The aerodynamic analysis section discusses the concept of the aerodynamics of a sphere, the data acquisition techniques used in the research, the CFD methods conducted by Wright State in collaboration with this thesis, and finally the concept behind Reynolds number scaling for wind tunnel analysis.

# III. Research Methodology

## 3.1 Chapter Overview

The previous Air Force Institute of Technology (AFIT) research conducted for the celestial icosahedron design, as well as other geometric shapes, assumes there is a symmetric sea-level pressure evenly distributed over the vacuum lighter than air vehicle's (VLTAV) membrane. The research conducted to date has not evaluated the interaction between the aerodynamic pressures and forces acting on the vehicle with the structural dynamics that have been thoroughly analyzed. In order to accurately characterize the aerodynamics of the celestial icosahedron VLTAV, a structural analysis must be run first in order to determine deformations expected due to atmospheric pressure.

The model analyzed is a variation of the model that Moore analyzed in the Complete Abaqus Environment (CAE) for his thesis. While Moore's model (Figure III-1) had a diameter of 0.7576 meters as the minimum diameter, the model for the wind tunnel tests will need to be smaller in diameter in order to fit in the test section [1].

This chapter addresses the methodology behind the research conducted for this thesis. The aspects addressed include the finite element model, validation of wind tunnel test setup, stagnation pressure scenario, conversion of structural analysis mesh to solid body, additive manufacturing practices, and incorporation of aerodynamic effect to the structural analysis.

42
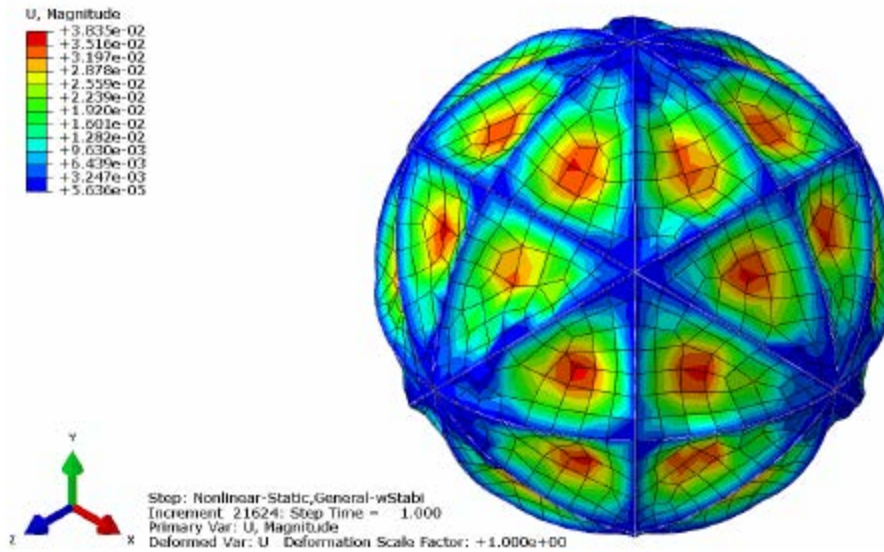
**Figure III-1. Deformation contour plot for the feasible minimum diameter model (0.7576 meters) [1]**

### 3.2 Finite Element Model

In order to produce the deformed geometry, which eventually is tested in the wind tunnel for aerodynamic effects, a structural analysis similar to that of past AFIT students' research must be conducted. The Finite Element Analysis software Abaqus is used to conduct the structural analysis, just as past students have conducted their analysis. The analysis run was consistent with Kyle Moore's analysis of his minimum diameter model. The geometry of the wire frame is 0.3788 m in radius for each of the 9 circular frame elements with a membrane draped over. This model was considered because it is the worst case scenario model for existing factor-of-safety when analyzed with symmetric sea-level pressure acting on the surface. The elements of the frame and the membrane are constrained together using a tie constraint with a surface to surface discretization method. The frame structure was meshed with 552 B31 beam

43

elements and the skin was meshed with 1827 M3D4R membrane elements as shown

in Figure III-2 and Figure III-3 respectively. [1]
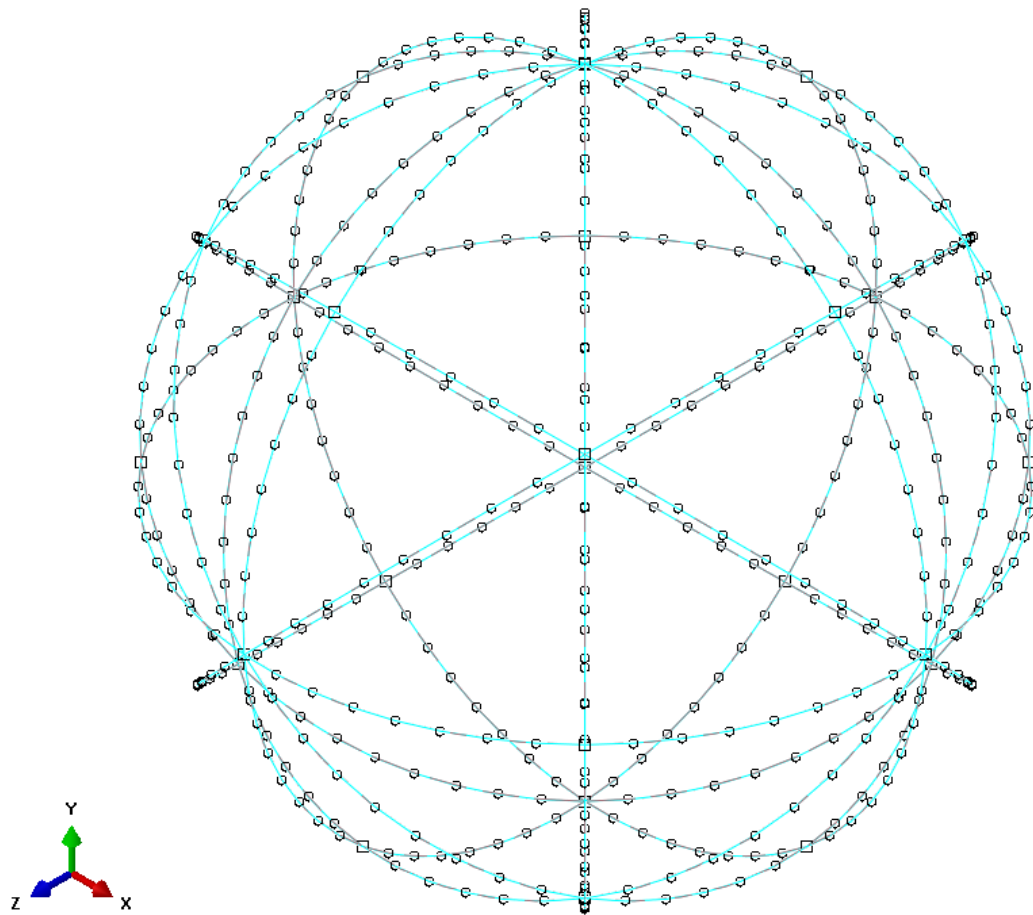


**Figure III-2. B31 element mesh of the frame part**
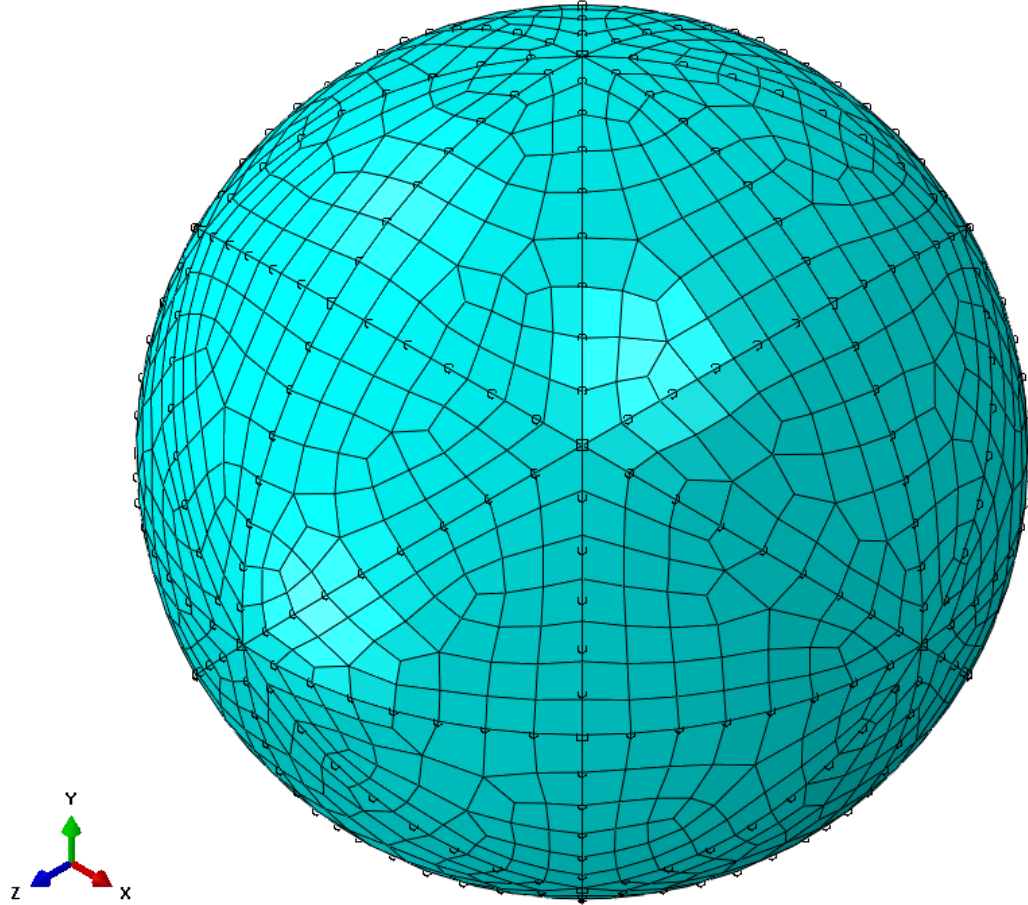
**Figure III-3. M3D4R element mesh of the skin part**

The frame is modeled using thin walled pipes with a radius of $8x10^{-3}$ meters and a thickness of $2.00x10^{-4}$ meters, and the skin is modeled by giving the membrane elements a thickness of $7.75x10^{-7}$ meters [1]. The model also utilizes the same boundary conditions as Moore's model which consisted of constraining both the top and bottom vertices laterally (U1=U3=0). The boundary conditions used can be seen in Figure III-4.

45
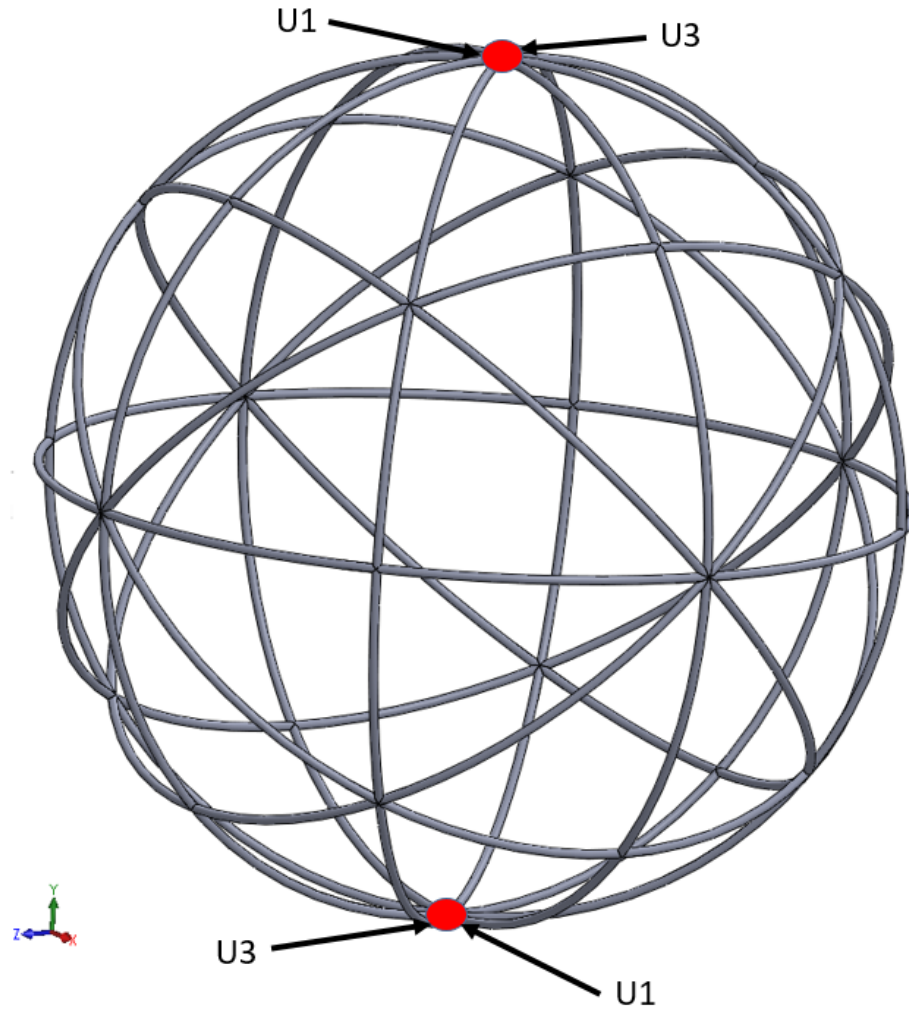
**Figure III-4. Boundary conditions for structural analysis [1]**

The analysis for the finite element model employed the use of a quasi-static, nonlinear loading condition consistent with a pressure equal to sea-level (101,325 Pa) acting uniformly on the outer surface of the celestial icosahedron. The nonlinear step in the analysis utilized the Newton-Raphson technique for addressing nonlinear characteristics. The Newton-Raphson technique is discussed in greater detail in the structural analysis section of the theory chapter.

Also, the quasi-static, nonlinear step utilized the adaptive stabilization feature in the nonlinear analysis. The adaptive stabilization reduces the instabilities and eliminates rigid body modes in an analysis which employs membrane elements. The adaptive stabilization method used in the structural analysis is discussed in greater detail in the theory chapter as is the Newton-Raphson technique. The values used for automatic stabilization and incrementation in the nonlinear analysis step are provided in Table III-1. Also, a study was conducted varying the two parameters of the automatic stabilization tool (dissipated energy fraction and maximum ratio of stabilization to strain energy) to determine if the parameters effect the drastic change in displacement Moore was observing at approximately 10% of the load applied. This study along with the results are discussed in greater detail within the results chapter.

**Table III-1. Nonlinear analysis parameters**

| Dissipated Energy Fraction | $2x10^{-4}$ |
|---|---|
| Maximum Ratio of Stabilization to Strain Energy | $5x10^{-2}$ |
| Maximum Number of Increments | $1x10^{8}$ |
| Initial Increment Size | $1x10^{-6}\ sec$ |
| Minimum Increment Size | $1x10^{-36}\ sec$ |
| Maximum Increment Size | $1\ sec$ |

### 3.3    Stagnation Pressure Comparison

The celestial icosahedron with a diameter of 0.7576m was used to run an analysis within Abaqus to determine the difference in the maximum displacement of a

47

hemisphere with a sea-level atmospheric pressure applied (101,325 Pa) and a hemisphere with a stagnation pressure uniformly applied consistent with the stagnation pressure at 17.8816 $\frac{m}{s}$ (101,509 Pa). The purpose of this analysis is to determine the soundness of the underlying assumption made that the aerodynamics do not significantly affect the deformation of the structure. The analysis conducted used the exact same parameters as the analysis run for the symmetric sea level pressure analysis to include element profile, element type, number of elements, material properties, geometry, tie constraints, boundary conditions, and step conditions. The only option changed within the analysis was the load applied, which was as applied as described previously in this section. The reason a stagnation pressure is used over an entire hemisphere is because it shows the reaction of the structure to a worst case scenario which would not be seen operationally. This allows the aerodynamic analysis of the VLTAV to be conducted on a model which is deformed consistent with a sea-level atmospheric pressure on the outside with an internal vacuum.

The stagnation pressure used assumes the flow over the VLTAV is incompressible which is approximately below 0.3 Mach. This is equivalent to 103.266 $\frac{m}{s}$ for an environment in which the speed of sound is 344.668 $\frac{m}{s}$. The incompressible assumption is valid due to the fact that the velocities used for this research's purposes are well below half of the compressible threshold. The equation for calculating the stagnation pressure for a given velocity, air density, and static pressure is shown below.

48

$$P_{Stagnation} = \frac{1}{2}\rho v^2 + P_{static} \qquad (5)$$

In this equation, $P$ is the pressure whether stagnation or static, $\rho$ is the air density (for the purpose of this research, the air density of an elevation associated with AFIT was used), and $v$ is the airspeed velocity. For a velocity of $17.8816\frac{m}{s}$, it was determined that a stagnation pressure of 101,509 Pa is endured. Figure III-5 and Figure III-6 show the loads applied to the celestial icosahedron with the stagnation pressure hemisphere and the sea-level pressure hemisphere respectively. The addition of the stagnation pressure on the left hemisphere is the difference between the loads highlighted in the figures.
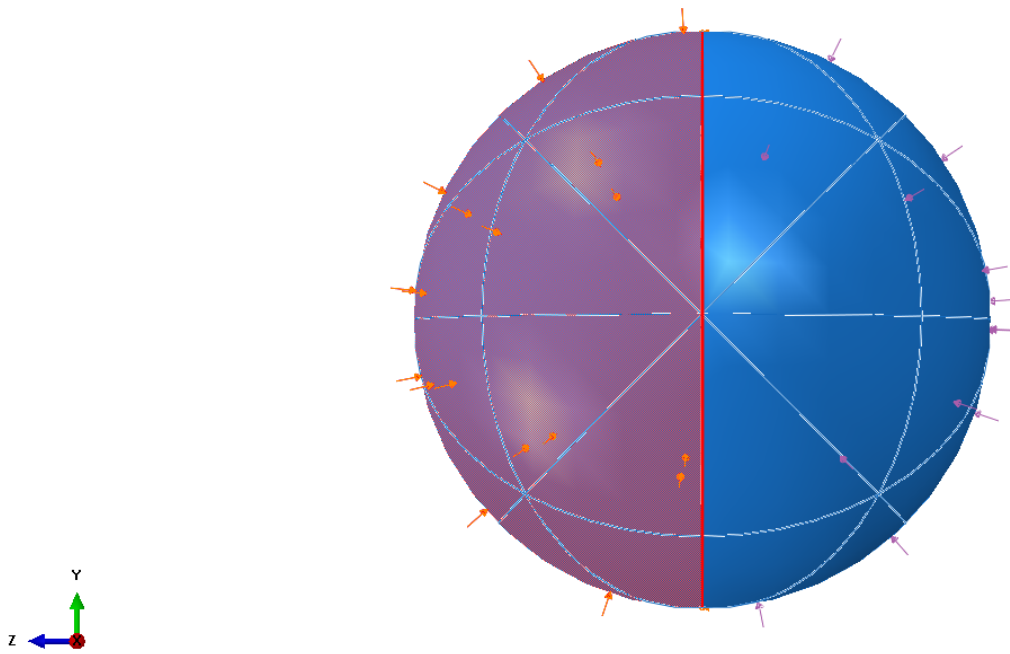
**Figure III-5. Stagnation pressure hemisphere**
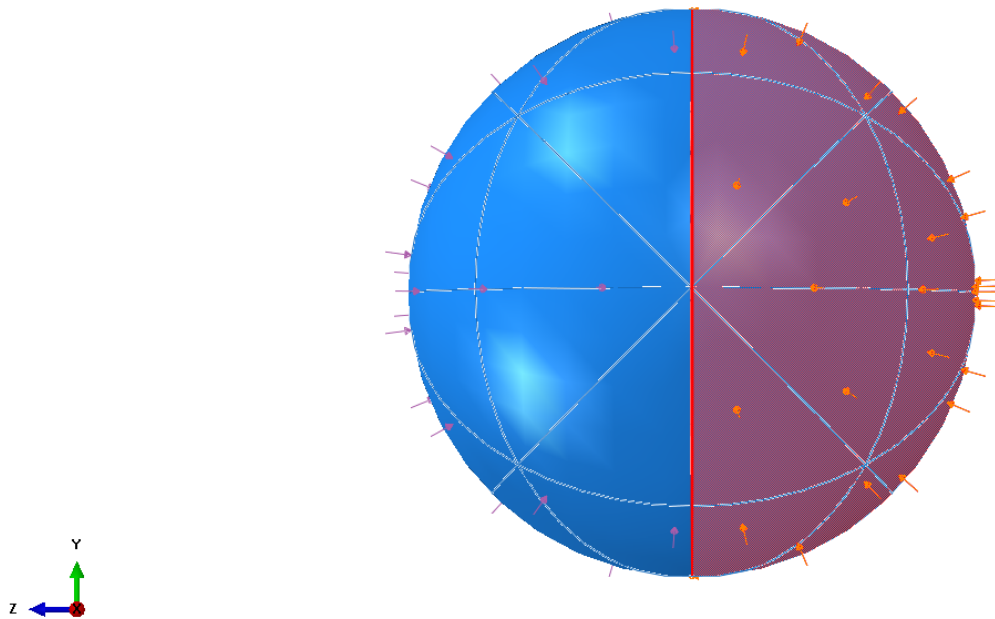


**Figure III-6. Sea-level atmospheric pressure hemisphere**

50

### 3.4    Convert Structural Analysis Mesh to Solid Body

The deformed mesh created from the structural analysis conducted in Abaqus is exported as a point cloud file of deformed nodal positions into the SolidWorks computer-aided design (CAD) software. The add-in ScanTo3D within SolidWorks allows for producing a solid body structure through mapping surfaces onto the point cloud and adding thickness to those surfaces. Once a solid body form of the deformed structure is produced, SolidWorks is used to post process the geometry for use in wind tunnel testing.

First, a point cloud file of the deformed nodal positions after the structural analysis is complete must be exported from Abaqus. Due to the fact that the converged mesh from a geometric standpoint is relatively coarse, an interpolation function in MATLAB is used to smooth the contours of the point cloud file from Abaqus. The interpolation function interpolates nodal coordinates in a spherical coordinate system using natural neighbor interpolation methods. The script can be found in Appendix A. The results of applying this MATLAB function to the point cloud file exported from the structural analysis are shown in Figure III-7 and Figure III-8. As is evident in this figure, the original export is coarse and it is difficult to pick out the nodal points. The interpolated point cloud has much finer resolution for converting into a solid model.

After the interpolation function provides finer resolution, the new point cloud is imported into the SolidWorks ScanTo3D add-in for conversion to a solid body. The Mesh Prep and Surface wizards within the add-in add physical geometry to the point cloud file by draping surfaces over the x-y-z points within the point cloud. These

51

surfaces can be thickened to create a solid body to be utilized for printing a wind

tunnel model or conducting a CFD analysis as was done in this research. The finished

product from converting the deformed mesh from the structural analysis to a solid

body shape is shown in Figure III-9. The solid body shape in the figure had a

diameter of 0.2032 m and the surface was thickened by 0.00635 m to create a solid.
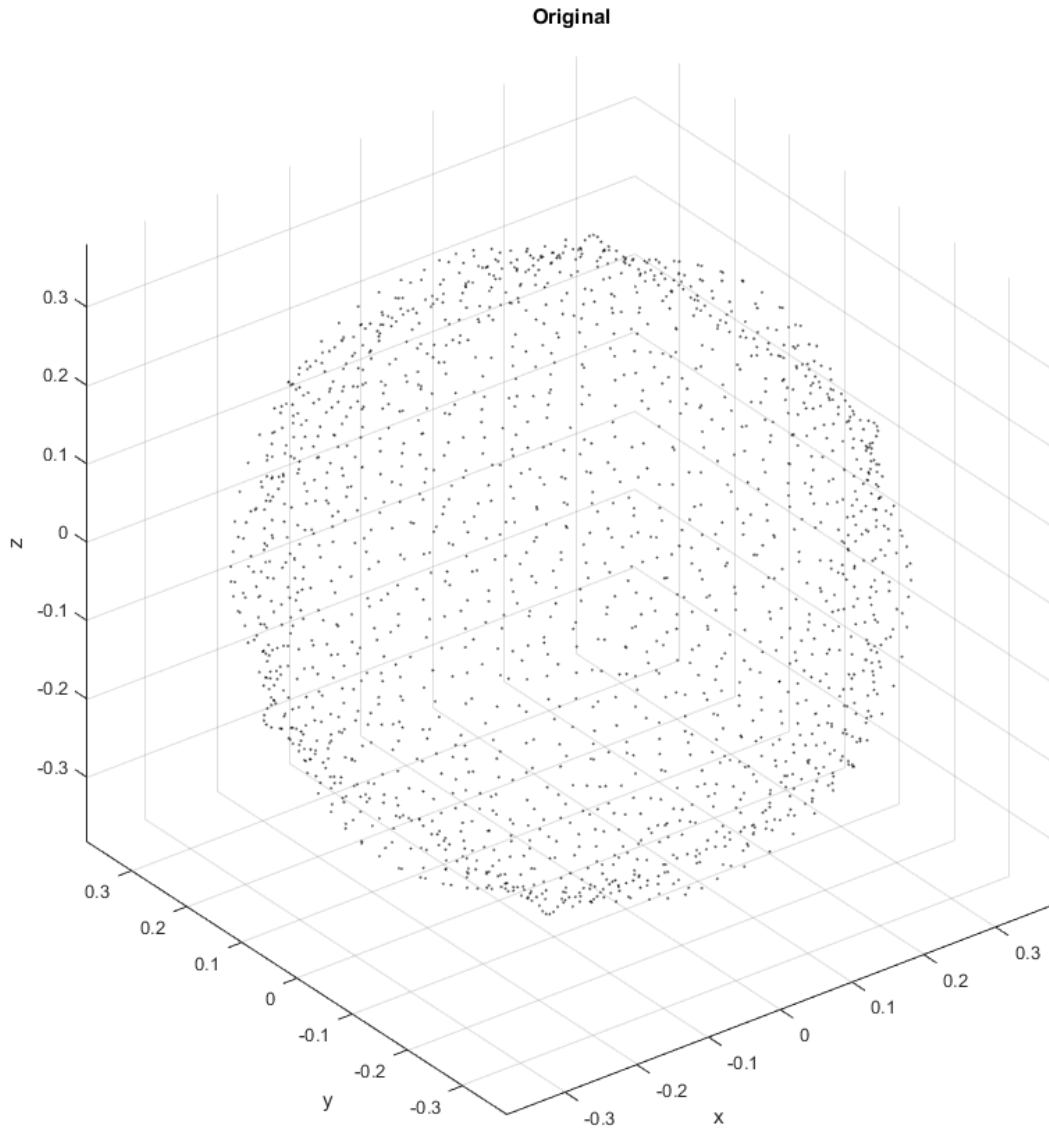


**Figure III-7. Nodal coordinates of structural analysis mesh prior to point cloud interpolation using MATLAB function**

52
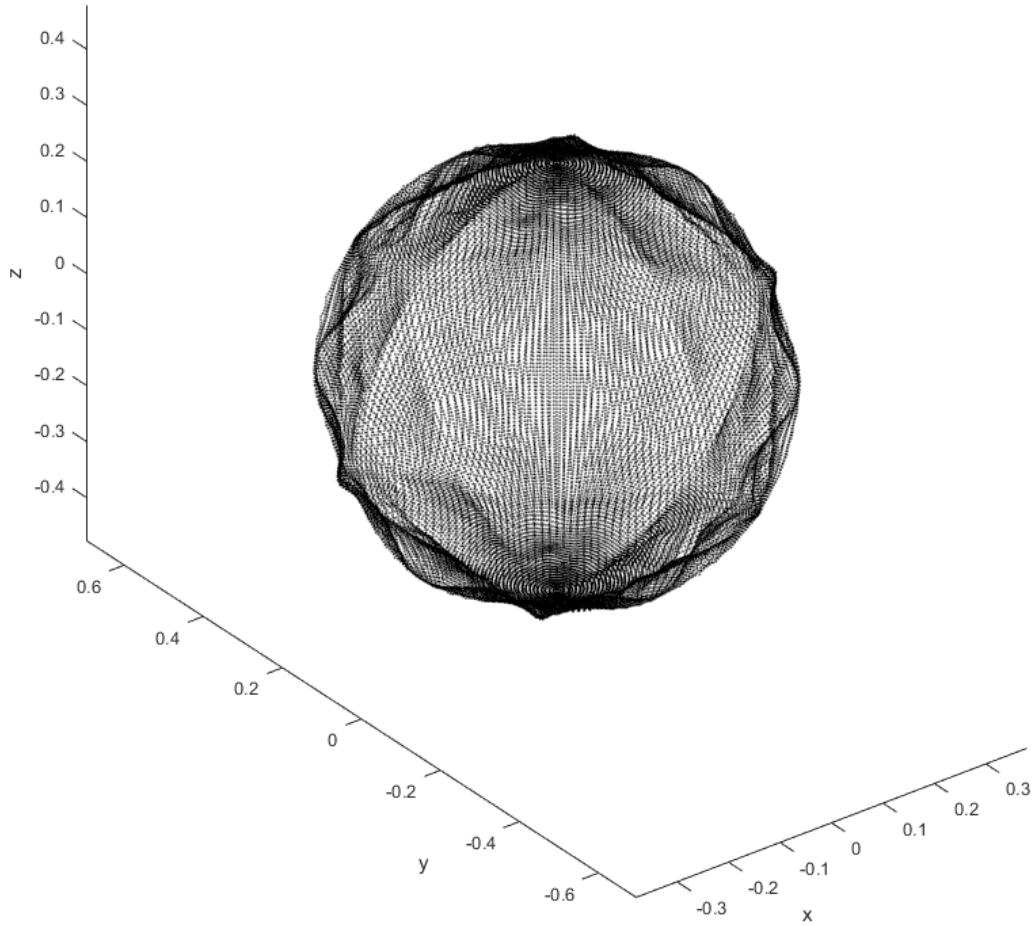
**Figure III-8. Results of applying point cloud interpolation using MATLAB function to the structural analysis mesh**
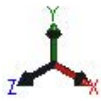
**Figure III-9.Deformed VLTAV post conversion from structural analysis mesh to solid body**

### 3.5    Additive Manufacturing of Tunnel Articles

In order to ensure that the conducted experiments for the deformed celestial

icosahedron are accurate, first the method through which aerodynamic effects would

be measured needed to be validated. Because the aerodynamics of a complete sphere

are well known and well documented, a perfect sphere is manufactured and tested to

ensure that the set-up for the experiments produces accurate results. Figure III-10 and

Figure III-11 show the bottom and top, respectively, of the sphere which will be

printed and tested against data correlation calculations. The spherical model had a

54

diameter of 0.3048 m and a wall thickness of 0.0127 m. The diameter of the deformed

shape, as mentioned in the previous section was reduced to 0.2032 m. The reduction

in diameter is a result lessons learned from the spherical model. For example, the

0.3048 m diameter spherical model vibrated significantly at higher tunnel velocities.

The diameter of the deformed tunnel model was reduced in attempt to mitigate these

vibrations which did result in a much lower level of vibrations during testing. Another

contributing factor to the vibration of the perfectly spherical model was the diameter

of the channel which the force balance fit into. The channel was made to be a slightly

larger diameter than the force balance itself in order to ensure the force balance could

be inserted. Since it was not a perfect fit, the model was able to vibrate in the tunnel.

The diameter of the channel was reduced for the deformed shape in order to reduce

the vibration as well.



Channel for Force Balance
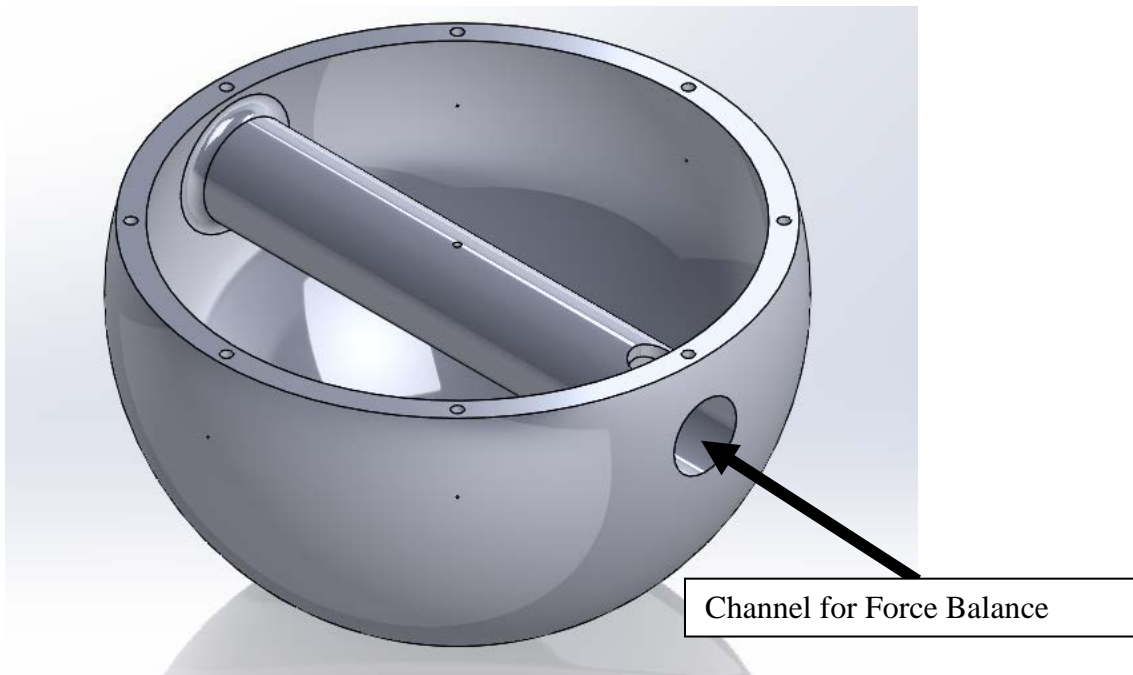
**Figure III-10. Bottom portion of perfect sphere test article**

55
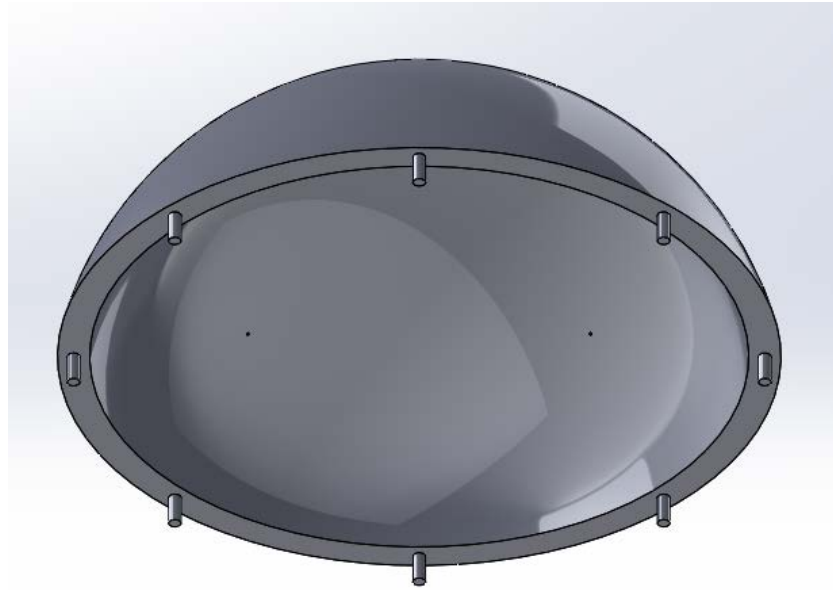
**Figure III-11. Top portion of perfect sphere test article**

The sphere is split into two sections in order to mount the model into the wind

tunnel. The channel seen running through the bottom portion of the sphere is where

the force balance is inserted into the sphere so the test article can be mounted. The

female and male connections on the top of the bottom portion and the bottom of the

top portion respectively provide support to the seam where the two portions of the

sphere connect. Also, pressure taps have been added to the outer surface of the sphere

so that pressures on the surface of the sphere can be measured. A reasonable number

of pressure taps needed to be added in order to compare the experimental results to

the results in CFD analysis. For this purpose, 16 pressure taps were used

symmetrically placed around the model. This allowed enough data points for

comparison against CFD results. Also, more taps were not added to ensure the tubing

56

did not interfere with mounting the model in the tunnel. All of these features are also included in the final deformed model from which the results of this thesis are based. Once printed, this perfectly spherical model is tested in the wind tunnel and compared to analytical results to determine if the test setup is correct.

In order to manufacture the test article, the SolidWorks file of the solid body is exported as a .STL file, which is a file type that describes only the surface of an object through tessellation, and imported into the 3D printing software. The AFIT additive manufacturing facility's Objet Eden 500V 3D printer was used to additively manufacture the perfect sphere test article. The material used was Stratasys' VeroClear rigid transparent polyjet material.



**Figure III-12. Objet Eden 500V 3D printer**

The build of the perfectly spherical model consisted of approximately 1500 layers consuming 6.765 kg of model material as well as 11.406 kg of support material. The build took approximately 47 hours for the bottom of the sphere and 29 hours for the top of the sphere with a total material cost of $1900. Figure III-13 shows the bottom

of the sphere as a finished product on the printer and shows a part of the post-

processing.



Putty knife used for post
process removal of support
material

12in diameter
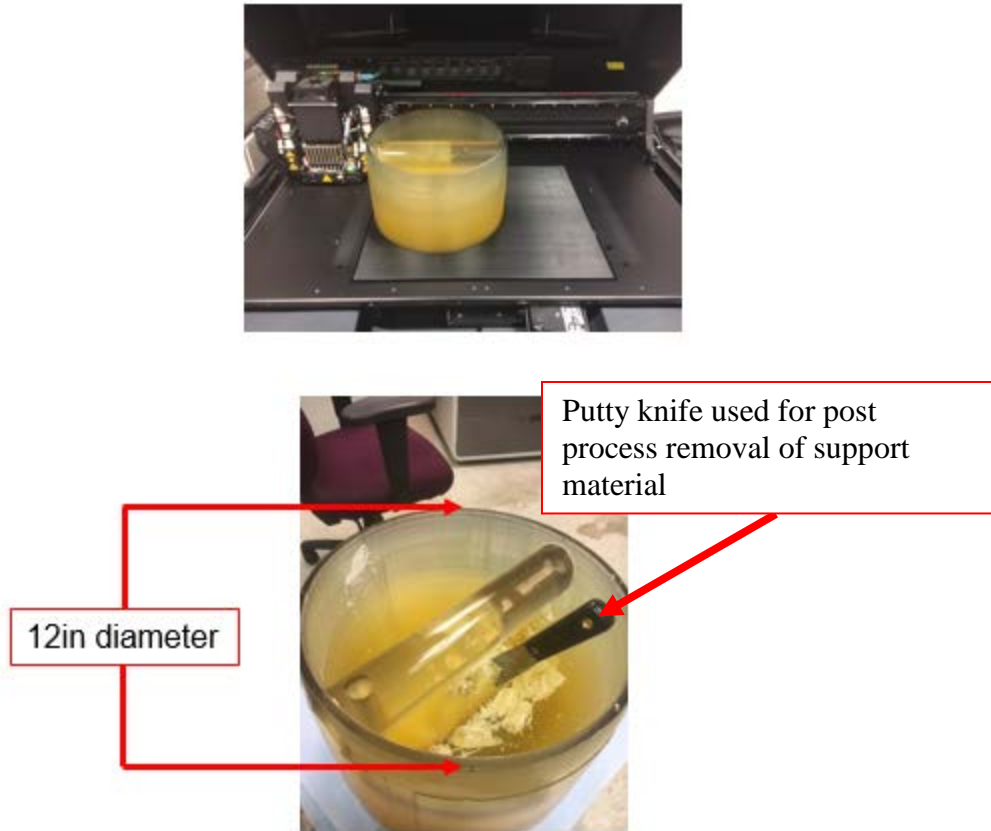
**Figure III-13. Post processing of the bottom portion of the perfectly spherical model**

### 3.6    Validation of Experimentation and Analysis Methods

As mentioned previously, the purpose of conducting analysis and experiments

with the perfectly spherical model is to validate the methods of experimentation and

CFD analysis. By analyzing the sphere in the wind tunnel and in CFD, a comparison

to analytical data can be made to determine if the methods for testing are valid. Also,

the interfaces between structural and CFD analyses could be tested with respect to

exporting and importing models into separate software packages.

58

The sphere is analyzed in the wind tunnel and in the CFD software to compare to the analytical data presented in aerodynamic analysis section of the theory chapter. If the data collected from both CFD and wind tunnel analysis agree with the analytical data, then the design of the wind tunnel test article and the methods used for CFD analysis are validated. The validation of the test methods offers confidence in the data collected from analyzing the deformed VLTAV in the wind tunnel as well as CFD.

Secondly, the sphere test case provides insight into how a model can be exported and imported from different software packages for analysis. Ultimately, the deformed VLTAV model is analyzed in Abaqus, made into a solid model in SolidWorks, and aerodynamically analyzed in the ANSYS Fluent software. The interfaces between these separate software packages had to be understood and established. The spherical model provided an understanding and a validation of these interfaces between software packages. Since the perfectly spherical model built in SolidWorks was imported into the Fluent software and analyzed successfully, it was apparent that the same could be said for the deformed VLTAV model once the deformed shape was produced.

## 3.7    Incorporating Aerodynamic Effects to Structural Analysis

The goal of the research associated with this thesis is to understand the fluid-structure interaction for a celestial icosahedron VLTAV. In order to understand this interaction, a method for incorporating the aerodynamic forces and pressures into the structural analysis had to be developed. The method chosen for doing so uses the point cloud file of pressure data exported from the CFD analysis as a custom load within the structural analysis software to be run as a secondary step once the sea-level

59

pressure has been applied simulating the evacuation of air to create an internal vacuum.

One of the products provided by Wright State University from the CFD analysis is a point cloud file of pressure distribution for each velocity at which the CFD model was run. The point cloud file provides an x, y, and z spatial location on the surface of the model with an associated pressure at that point. This pressure point cloud file is converted into a custom defined load within Abaqus for the structural analysis. Figure III-14 shows the distributed load applied consistent with the pressure distribution for the case of the perfect sphere.
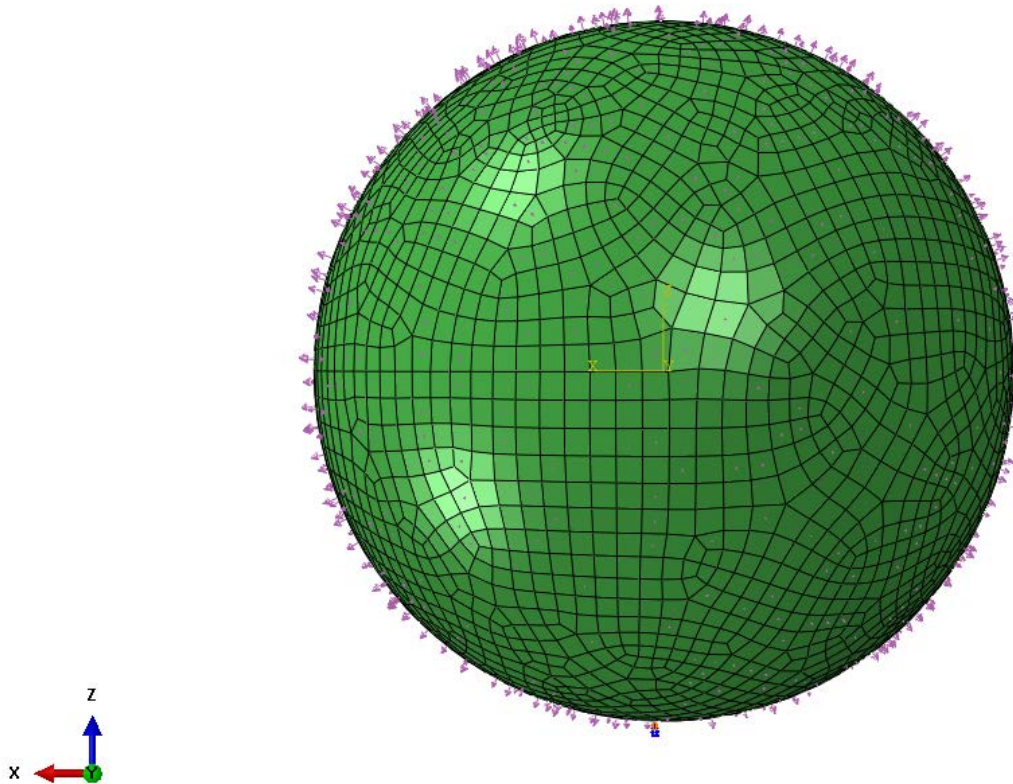


**Figure III-14. Pressure field applied as distributed load in Abaqus**

The pressure is provided as a differential from atmospheric pressure, therefore the method for applying the differential pressure load from aerodynamic effects includes applying the load in a secondary step within the analysis after the atmospheric pressure has been applied to simulate the internal vacuum.

Within the Abaqus load module, the point cloud data is read in as an analytical mapped field. Analytical mapped fields allow you to apply spatially varying load cases to a structural analysis. The Abaqus Online Documentation states, "For example, you can [using analytical mapped fields] define a spatially varying shell thickness or pressure load by providing the thickness or pressure values at different coordinates". The mention of applying spatially varying pressure values is exactly what this research is trying to accomplish with the point cloud file exported from CFD. [18]

## 3.8    Summary

This chapter describes the research methodology and the approach to experimentation for this thesis. An overview of the finite element model is provided to gain an understanding of how the VLTAV is analyzed from a structural analysis point of view. The method for providing confidence in the assumptions for the thesis is provided in the stagnation pressure scenario section. The method for converting the structural analysis model to a solid body model and the means for manufacturing a wind tunnel test article details how the wind tunnel model was created. The validation of the wind tunnel setup explains how confidence in the experimental and computational analysis was built. Lastly, the section on incorporating aerodynamic effects to structural analysis conveys how the CFD data is used within the structural

analysis to provide the results of the fluid-structure interaction. The methods

presented in this chapter led to results outlined in the next chapter.

# IV.   Results and Discussion

## 4.1   Chapter Overview.

This chapter addresses the results from the research associated with this thesis. The topics include the results from the validation of experimental methods, the results from the stagnation pressure comparison, the results from comparing the CFD data to the wind tunnel data, and lastly the results from the structural analysis after incorporating aerodynamic effects. The results are discussed in each of the sections to provide an interpretation of what the results mean in the context of this research.

## 4.2   Validation of Experimentation and Analysis Methods

In order to validate the methods for wind tunnel experiments and computational analyses, the test case of a perfect sphere was analyzed in the wind tunnel as well as in the CFD analysis tools. The aerodynamics of a perfect sphere are well known and documented in literature as described within the theory chapter of this thesis. The available data was compared with CFD and wind tunnel data to support the validation of methods used. Due to time constraints and schedule deconfliction within the wind tunnel, the pressure data for the perfect sphere case was not taken, but instead drag data was used to compare to available data for a perfect sphere. Figure IV-1 shows the experimental drag forces experienced in the wind tunnel compared to the analytical results from utilizing the drag coefficient equation from the data correlation provided by Morrison [23]. As is evident from the plot, the drag peaks and decreases in the experimental data before the analytical data. This is largely attributed to the fact that the analytical data is correlating drag data for a perfectly smooth sphere. The model used in wind tunnel testing for the experiment was additively manufactured

63

using the plastic printer in AFIT's additive manufacturing lab, and as a result of post processing does not have a completely smooth finish.
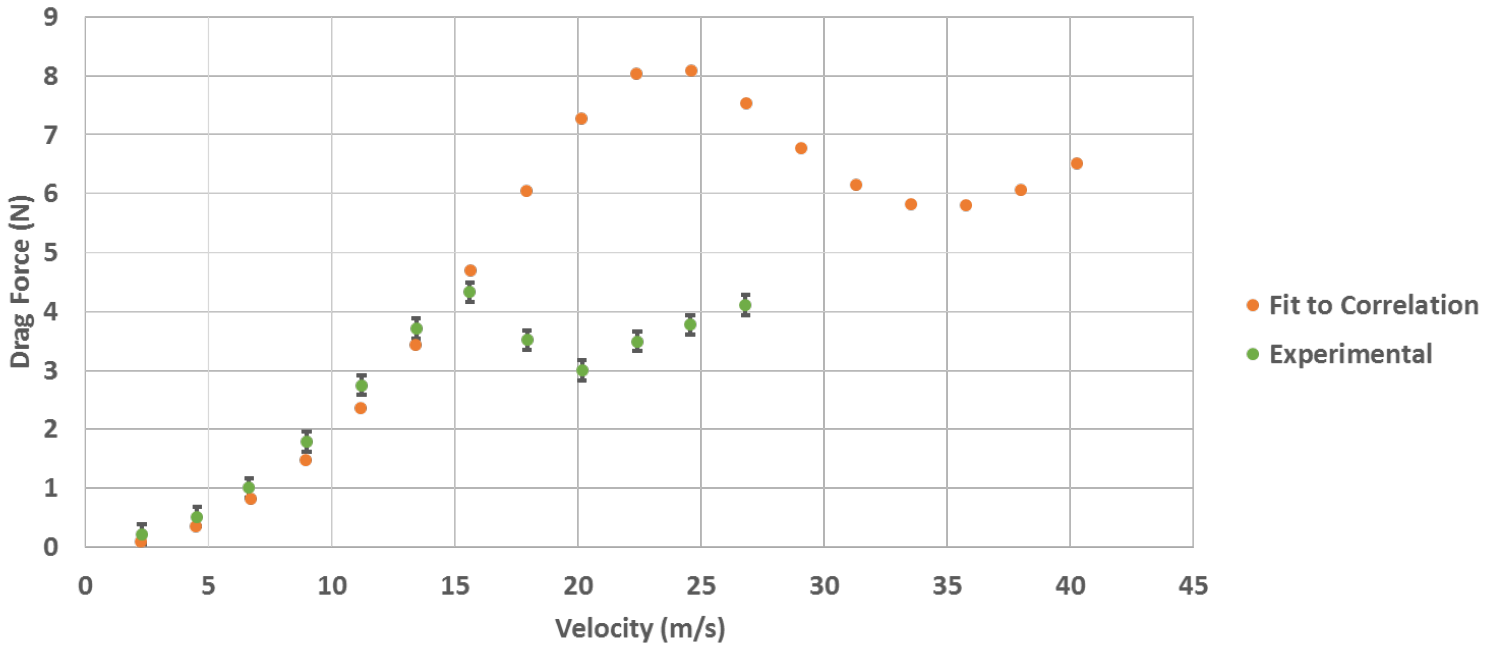


**Figure IV-1. Drag force vs. velocity for analytical and experimental data on a perfect sphere**

Cimbala states in his paper for drag on spheres, "Oftentimes it is desirable to have a very low drag coefficient so that the [sphere] can travel faster through the air. For cases where Reynolds number is not high enough for the drag crisis to occur natural, artificial roughness is often added to the sphere surface" [29]. This partially explains why the drag force lowers in the experimental data at a lower velocity than the analytical. It is because the relatively rough test article is tripping the flow into turbulent flow prior to the smooth sphere therefore causing an earlier drag crisis. However, at lower velocity in the laminar range, the experimental drag force

64

compares well with the analytical drag force therefore adding validity to the experimental setup.

The difference in drag crisis from analytical to experimental is more readily apparent in Figure IV-2. Figure II-7, earlier in the theory chapter shows that the drag crisis occurs where there is a sudden drop in drag coefficient as Reynolds number is increased. The error associated with the values in Figure IV-2 is derived from the error reported in the axial force values in the documentation for the force balance.
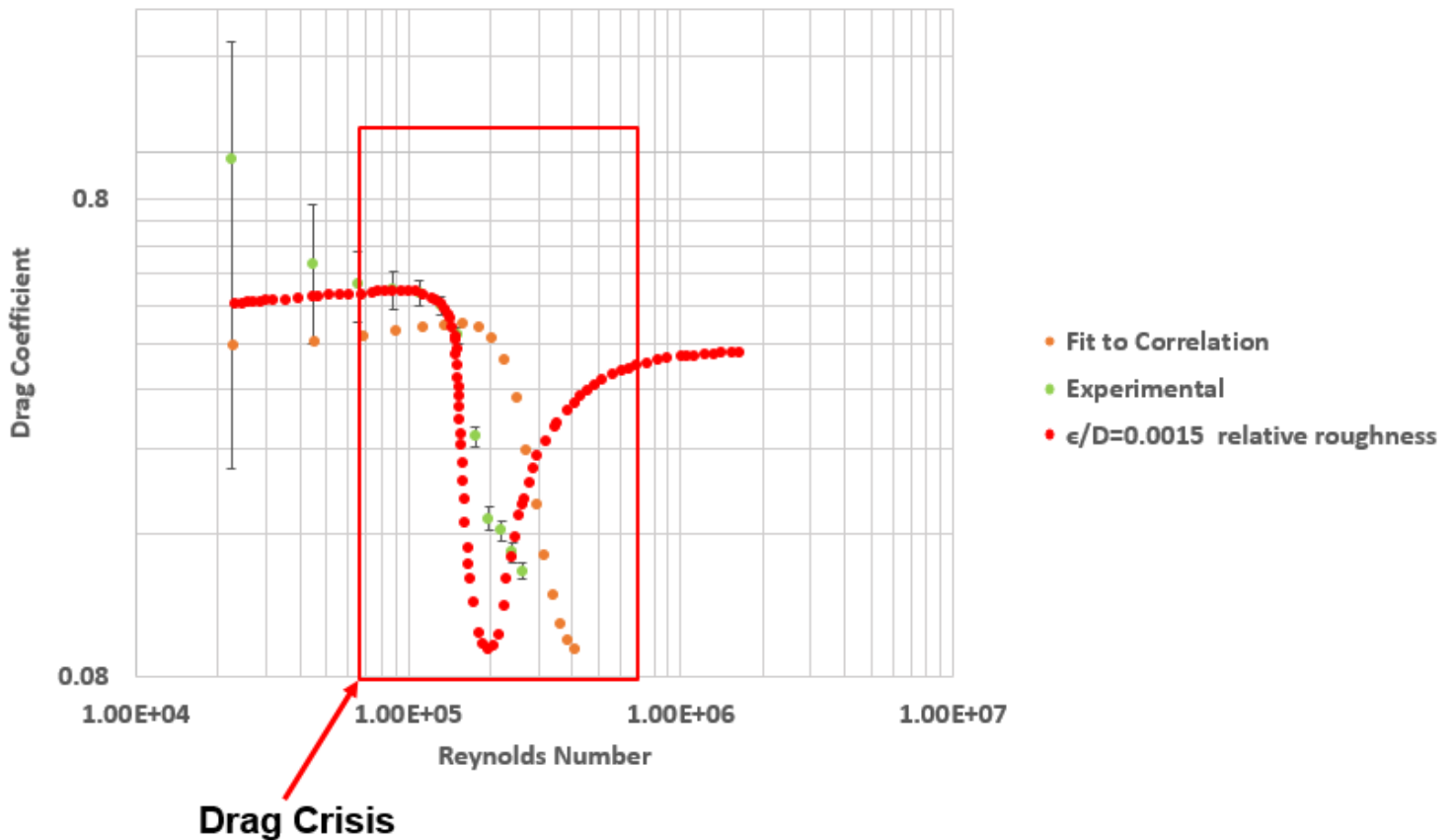


**Figure IV-2. Drag coefficient v. Reynolds number comparing analytical, experimental, and experimental corrected data**

65
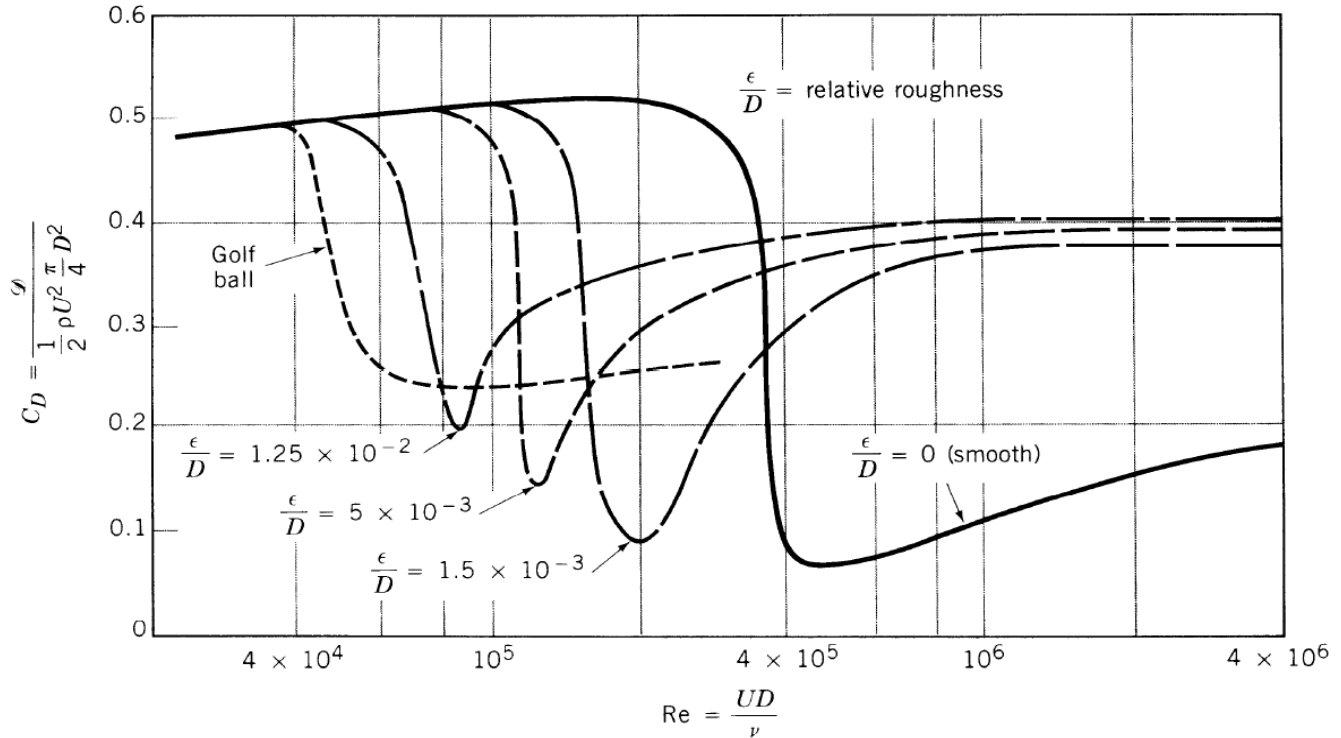
**Figure IV-3. Effect of surface roughness on the drag coefficient of a sphere** [29]

The comparison clearly shows a drop in drag coefficient for experimental data at a lower Reynolds number as compared to the analytical data. It is also important to note that the drag crisis did not happen as early as it would on a dimpled surface such as a golf ball as shown in Figure IV-3. Since the data lies within that range, it is safe to assume that the difference can be attributed to surface roughness. The data would be generally consistent with the $\frac{\epsilon}{D} = 1.5 \; x \; 10^{-3}$ curve from Figure IV-3. The data for a relative roughness value of $\frac{\epsilon}{D} = 1.5 \; x \; 10^{-3}$ is overlaid in Figure IV-2 to show the experimental data experienced a drag crisis at approximately the same Reynolds number.

Also, Figure IV-2 shows that the experimental data corrected for solid body blockage does not differ significantly from the experimental data itself within the

66

AFIT low speed wind tunnel. This effect was predicted within the theory chapter of the thesis. Since the perfectly spherical model has a blockage ratio of approximately 8% it was reasonable to expect there would not be any change in the data.

### 4.3 Stagnation Pressure Comparison

As stated previously, the stagnation pressure scenario allows for comparison of a perfectly symmetric sea level pressure load applied to the VLTAV and an asymmetric pressure load applied consisting of stagnation pressure at $17.8816 \frac{m}{s}$ applied to one hemisphere and atmospheric pressure applied to the other. Figure IV-4 and Figure IV-5 show the displacements of both of the hemispheres.
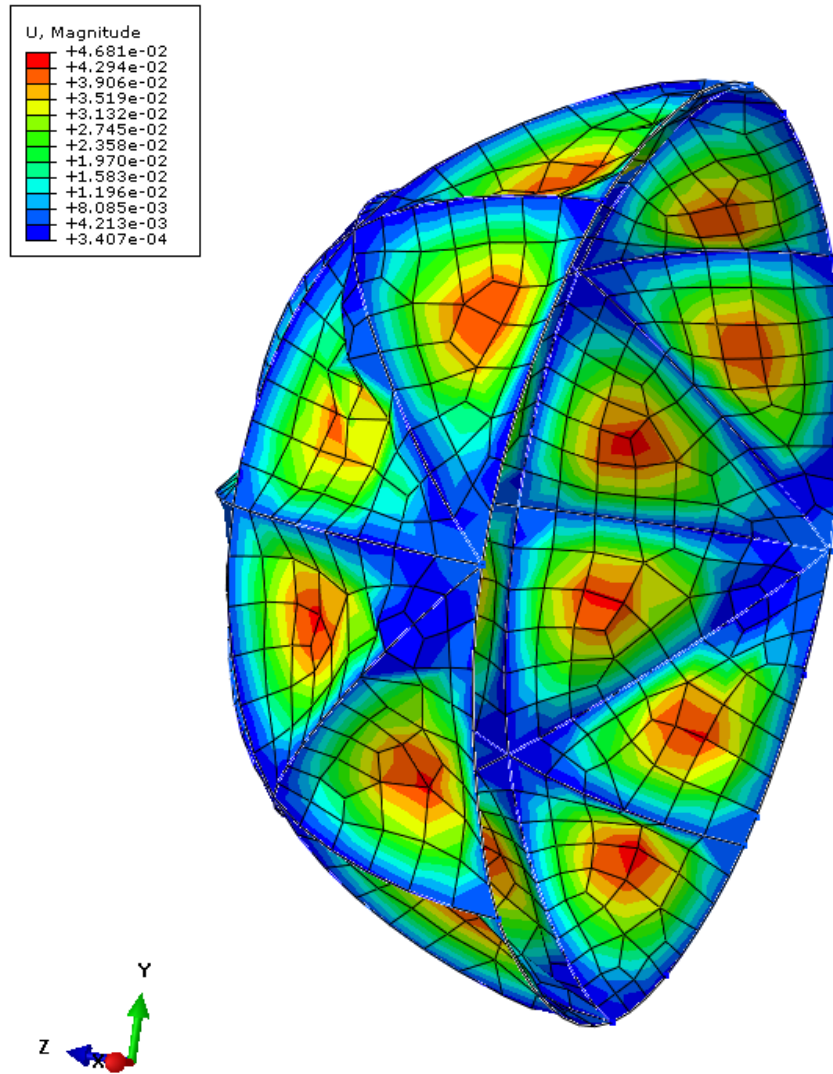
**Figure IV-4. Displacement of the hemisphere with stagnation pressure applied (101,509 Pa)**
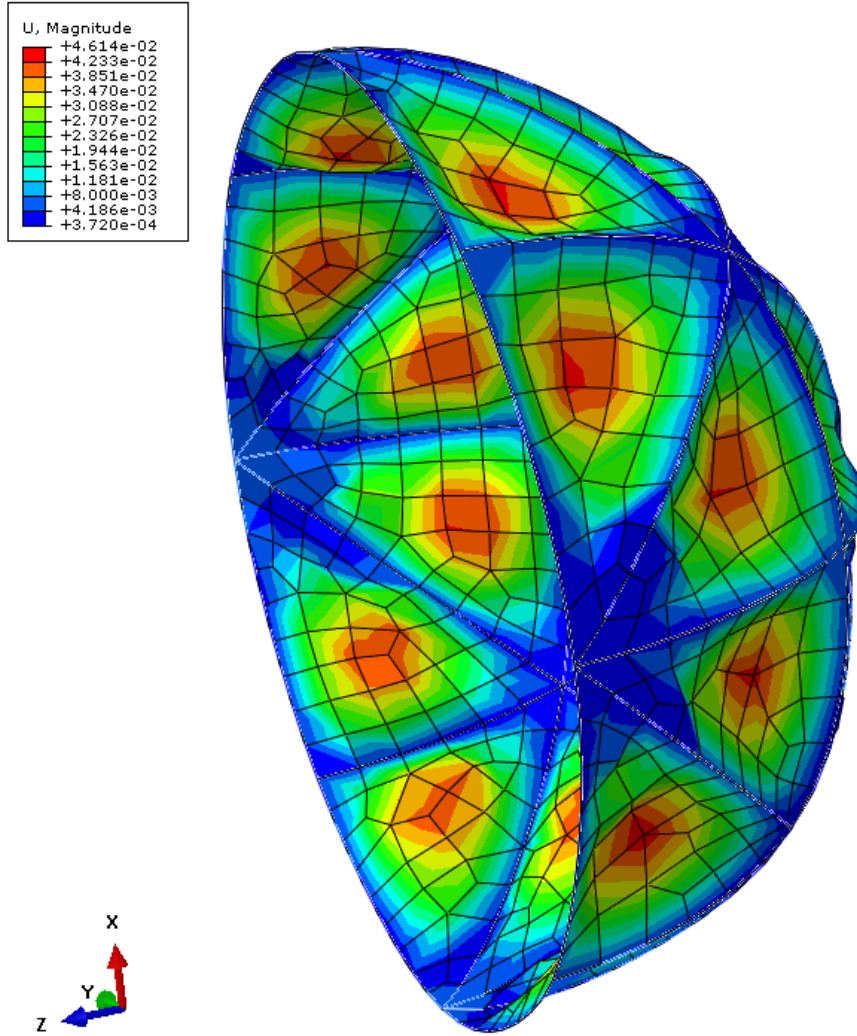
**Figure IV-5. Displacement of the hemisphere with sea level pressure applied (101,325 Pa)**

From the maximum displacements displayed in the legend, it is evident that the hemisphere with only sea level pressure applied is displaced less than the hemisphere with the stagnation pressure applied.

Table IV-1 tabulates the maximum pressure on each of the hemispheres along with the percent difference.

69

**Table IV-1. Maximum displacement of each hemisphere of stagnation pressure scenario**

| Stagnation Pressure Displacement (m) | Sea Level Pressure Displacement (m) | Percent Difference (%) |
|---|---|---|
| $4.761 x 10^{-2}$ | $4.681 x 10^{-2}$ | 1.7 |

This is a small percent difference and on the order of fractions of a millimeter in magnitude. Therefore, the difference in maximum displacement for the two pressure distributions is not significant enough to be of a concern when manufacturing the wind tunnel model. This shows that that the assumption made in the theory chapter of using a sea level pressure applied symmetrically over the entire celestial icosahedron in the analysis used to create the deformed model for wind tunnel analysis is a valid means of approaching the problem. The next section discusses another study conducted based on future work recommended by Kyle Moore in his research.

## 4.4    Follow-On Automatic Stabilization Study

As Moore was conducting Finite Element Analyses on the skin and frame of a celestial body at differing diameters, he noticed a phenomena of dramatic change in deformation as the load was applied in the results. Since this membrane response had not been observed previously, a study was carried out to determine the origin. As he post-processed the results, he tracked a point on the skin and documented the

70

displacement of that point as it deformed through the steps of the analysis. A similar approach was taken for this study.

The objective of this study is to determine if the values for the automatic stabilization tool affect this phenomena. For the original model, the default values of 0.0002 for the dissipated energy fraction and 0.05 for the maximum ratio of stabilization to strain energy were used.

It is assumed that analyzing a singular section of Moore's model with the same parameters that he used is sufficient for the purposes of the analysis. Figure IV-6 shows a section of Moore's model that was used for computational efficiency.

Most of the model parameters were consistent with Moore's model to include element cross sections, element types, element number, load type, and tie constraints. However, new boundary conditions had to be considered for the analysis. It was determined that since the beams themselves deflect, the most appropriate boundary
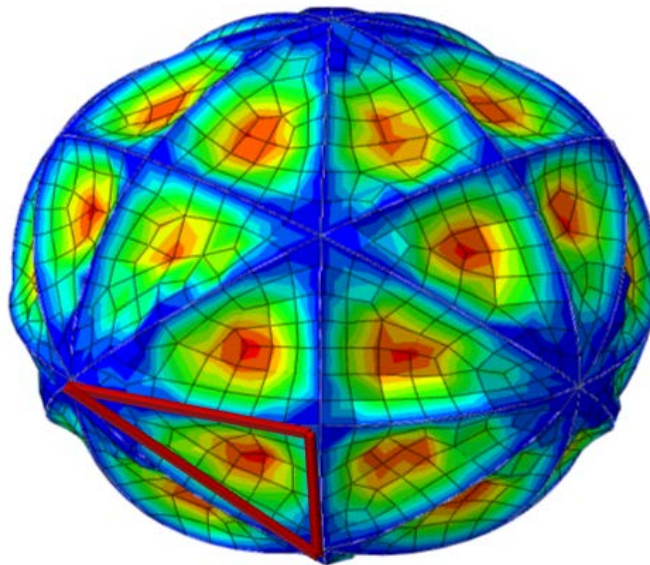
condition for the study would be to apply translational constraints at the three vertices

of the triangle but not rotational constraints as shown in Figure IV-7.

**Figure IV-6. Section of celestial icosahedron analyzed for the analysis**
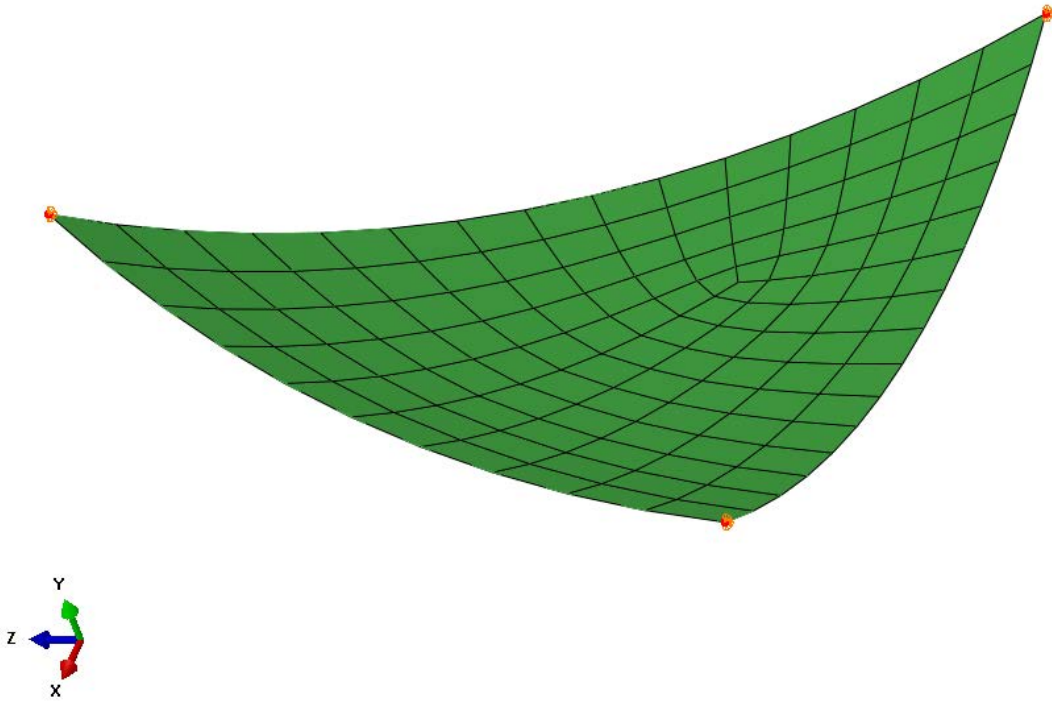


**Figure IV-7. Translational boundary conditions applied to the triangular section for analysis**

Figure IV-8 shows the node which is tracked as the analysis is carried out to

document the displacement as the load is applied. The displacements shown in the

figure are in meters.

72
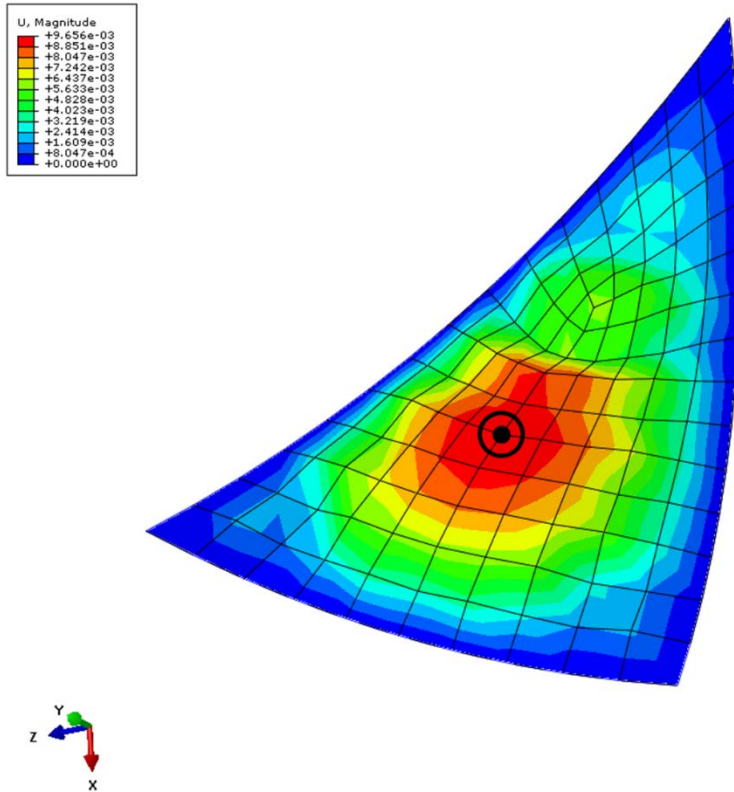
**Figure IV-8. Location of the tracked point on the skin** [1]

Through plotting the results of the displacement at this point, as shown in Figure IV-9, the same phenomena that Moore observed is apparent under 10% of sea-level applied pressure. The skin reduces in deformation before continuing in a nonlinear fashion to 100% of sea-level pressure. The movement indicates a dramatic snapping effect.

73
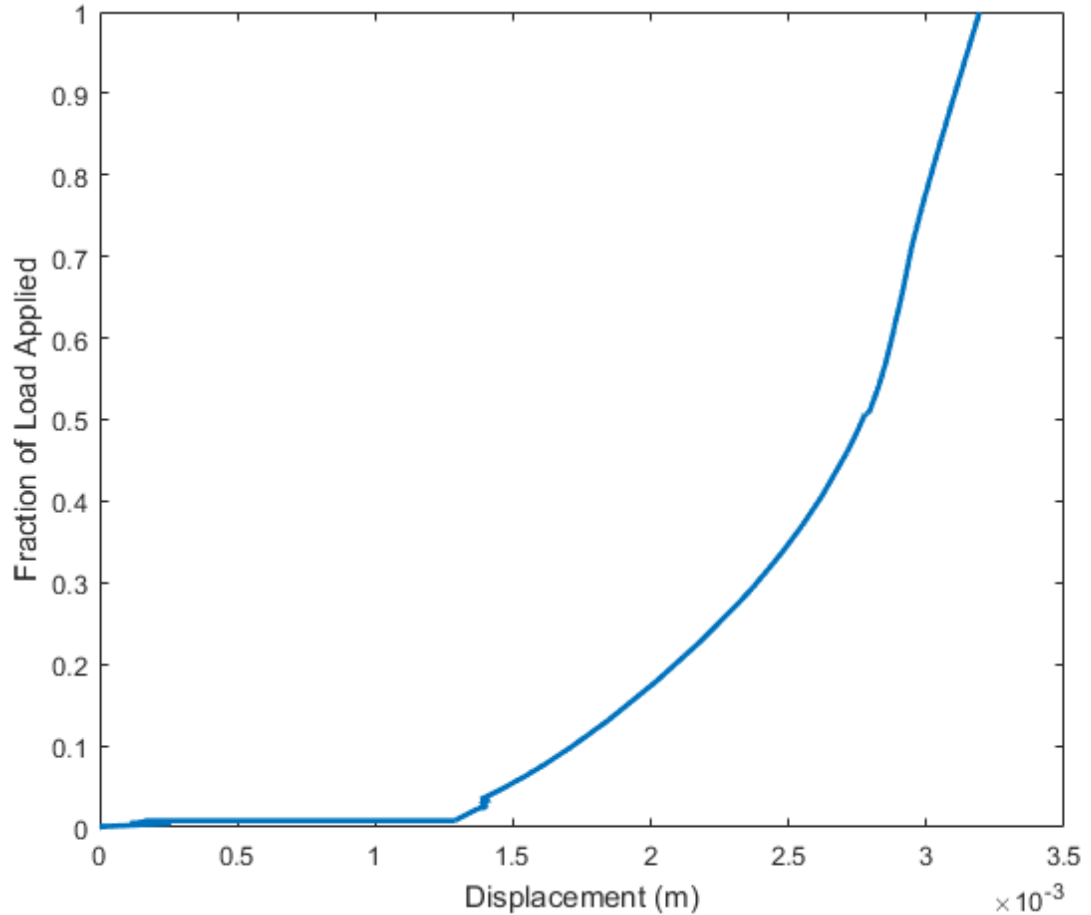
**Figure IV-9. Plot of deformation v. the fraction of sea-level pressure applied for the triangular section model**

It is observed that physically, since the membrane and frame are tied together through a constraint, the membrane is following the beam deflection as well as experiencing its own deflections. The results for displacement observed along the edge of the other members of the frame show the same behavior as observed in Figure IV-9.

The deformed geometry observed throughout the runs deforms in a way that would physically be expected. As the model was run through the steps, the skin deformed at a higher rate than the frame due to the fact that the skin is less stiff. The

74

maximum displacement of the skin, depending on which run was conducted, was approximately $8x10^{-3}m$.

The FE model was constructed with the geometries of the physical frame and membranes in mind. The frame is constructed with a pipe cross section consisting of a radius of $2.22829x10^{-3}m$ and a $1.11415x10^{-4}$ thickness. The material properties for the frame are set at $1250 \frac{kg}{m^3}$ density and $293x10^9$ Pa for Young's Modulus with a Poisson's Ratio of 0.33. The skin is constructed as a membrane with a $1.92464x10^{-5}$ $m$ thickness. The material properties for the skin are set at $2000\frac{kg}{m^3}$ density and $500x10^9$ Pa for Young's Modulus and a Poisson's Ratio of 0.33. The weight of the frame accounts for approximately 98.9% of the total weight whereas the skin accounts for approximately 1.1% of the total weight of the structure.

The same phenomenon from Moore's thesis is observed in the runs for this analysis at approximately 7% of the total applied load (sea-level pressure). As the values of the maximum ratio of stabilization to strain energy are varied, the results of the phenomena region (as shown in Figure IV-9) of the displacement seem to be unaffected. The same structural analysis model was run for differing values of maximum ratio of stabilization to strain energy, dissipated energy fraction, and the structural damping of the skin. The structural damping was varied to determine if it could have an effect on the region as well. The theory behind the adaptive stabilization technique can be found in the structural analysis section of the chapter on theory. Table IV-2 below shows the parameters that were varied. As each parameter was varied, the other parameters within the table were held constant.

75

Through varying all of these parameters, there was not a significant effect on the region of large changes in deformation for less than 10% of the load applied.

**Table IV-2. Parameters varied for automatic stabilization study**

| Dissipated Energy Fraction | Maximum Ratio of Stabilization to Strain Energy | Structural Damping of Skin |
|---|---|---|
| 0.0001 | 0.001 | 0.05 |
| 0.0002 | 0.01 | 0.1 |
| 0.0005 | 0.05 | 0.2 |
| 0.001 | 0.1 | 0.25 |
| 0.005 | 0.5 | 0.5 |

Since the varying of the parameters did not significantly affect the region of large changes in deformation, there is more confidence in the realization that the observation is a physical phenomenon. As discussed previously the physical effect causing this rapid change in deformation is most likely attributed to a wave type motion in the membrane as the load is applied. Now that more confidence is built into the structural analysis model, the CFD data for the deformed shape must be compared to wind tunnel data in order to build confidence in the CFD data.

## 4.5    CFD Comparison to Wind Tunnel

In order to use the CFD data for incorporation into the structural analysis model to study the effects of aerodynamic pressures, the CFD data is compared to wind tunnel results of the deformed VLTAV model to determine if the CFD data is reasonable. The first comparison made is the pressures measured at the ports on the wind tunnel

76

model compared to the pressures reported in the CFD analysis point cloud file. In order to compare the pressures from the wind tunnel results to the CFD data, the closest point in the CFD mesh to a certain pressure port on the wind tunnel model had to be determined. A MATLAB script was developed to find and compare pressure data between the CFD and wind tunnel data at the x, y, and z spatial position of each of the pressure ports. The MATLAB script can be found in Appendix B.

Figure IV-10 shows the spatial positions of each pressure port on the wind tunnel model within SolidWorks. The pressure ports were distributed evenly and symmetrically throughout the structure. The MATLAB script described in the previous paragraph was necessary to relate CFD and experimental data because while there were 16 data points experimentally, the CFD results exported thousands of data points for pressure due to the fineness of the mesh.
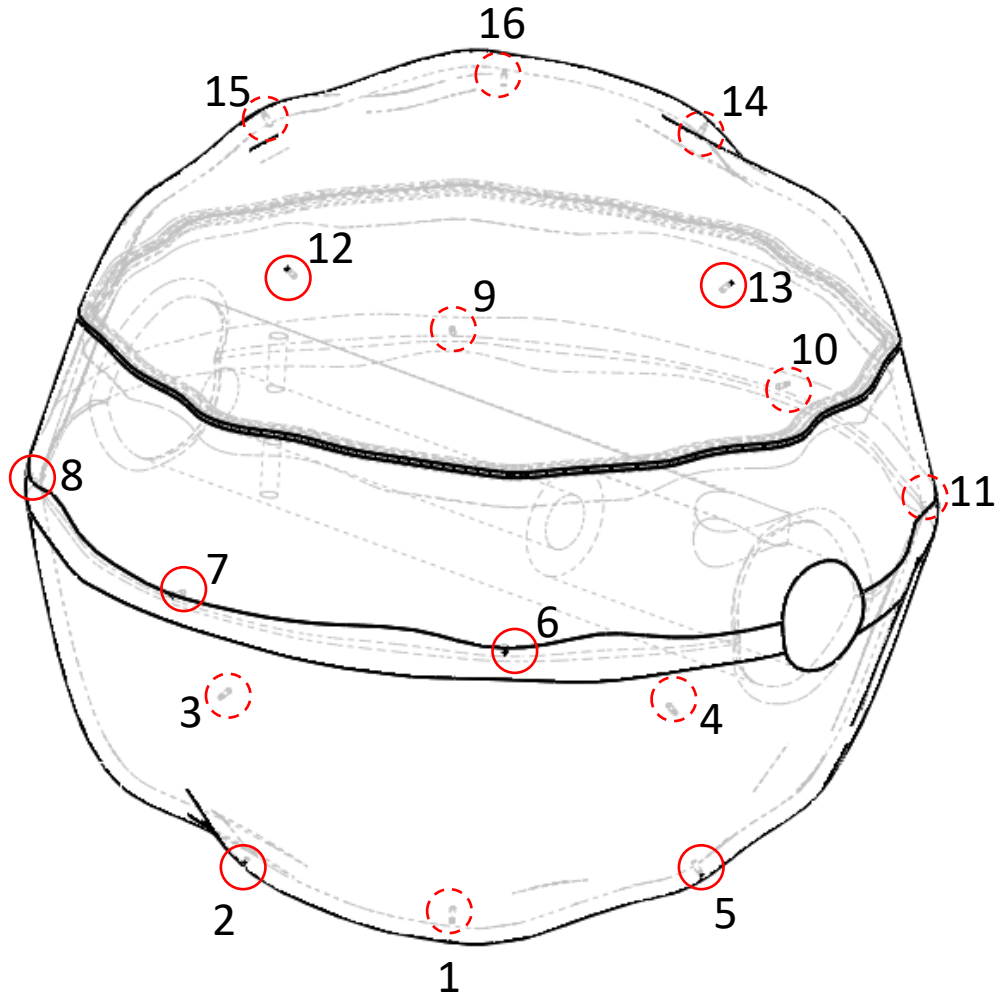
**Figure IV-10. Spatial orientation of pressure ports on the wind tunnel structure**

The comparison between the pressure output from the CFD analysis provided by

Wright State University and the measured experimental pressures are provided for

velocities of 50 mph ($22.352\frac{m}{s}$) to 100 mph ($44.704\frac{m}{s}$). The wind tunnel was run at

lower velocities but the data at lower velocities is not shown because the error

associated with the pressure scanner data acquisition system is above 15% of the

measured values so there is not enough confidence in the experimental results. The

data for lower velocities with error reported can be seen in Appendix C. The figures

below show the comparison between CFD and experimental results.
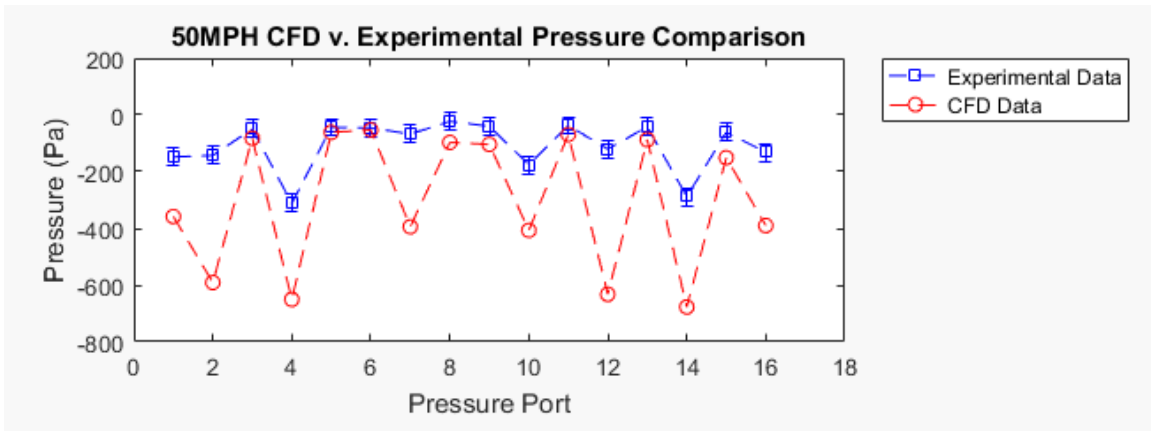


**Figure IV-11. Comparison of pressure data from CFD analysis and experimental results for 50 mph**
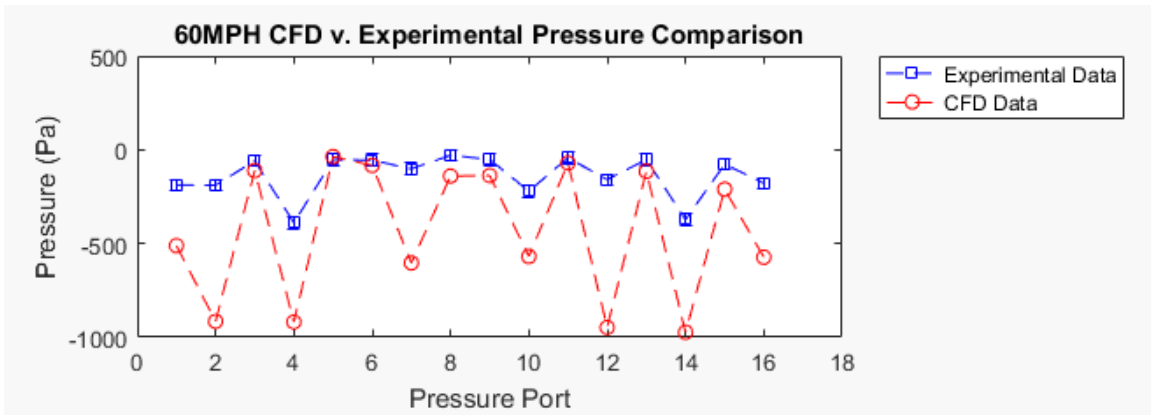


**Figure IV-12. Comparison of pressure data from CFD analysis and experimental results for 60 mph**
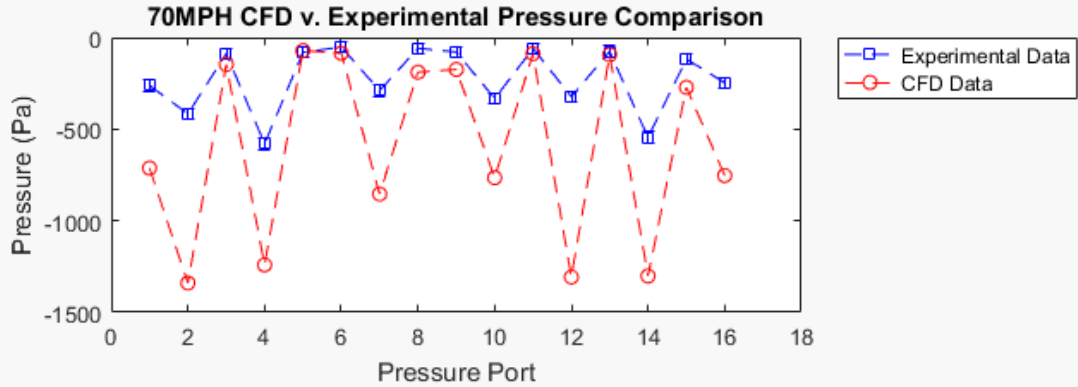
**Figure IV-13. Comparison of pressure data from CFD analysis and experimental results for 70 mph**
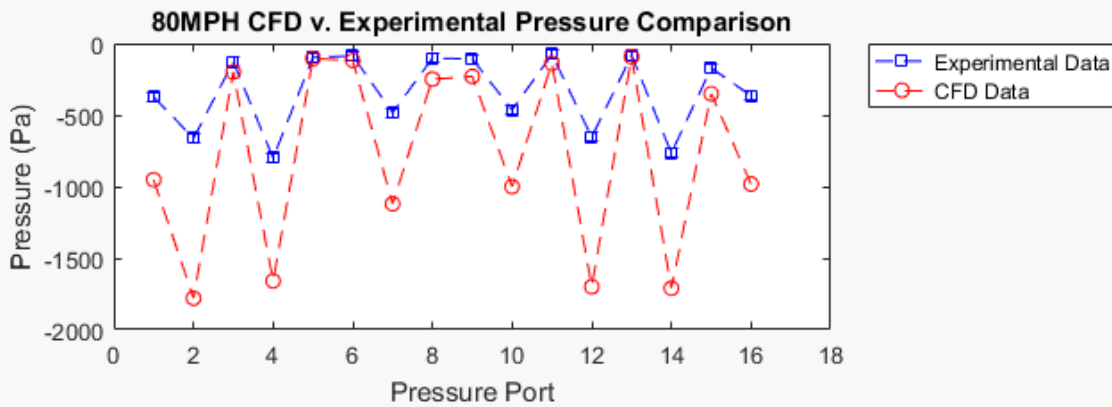


**Figure IV-14. Comparison of pressure data from CFD analysis and experimental results for 80 mph**
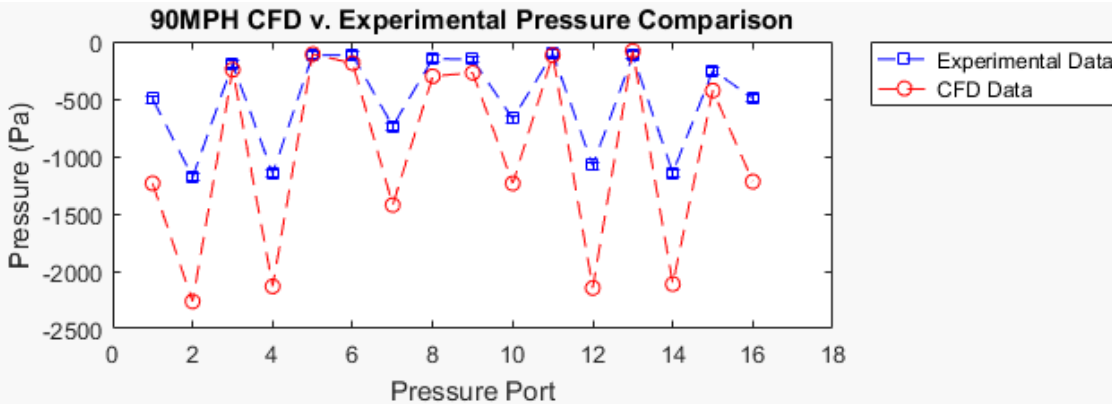


**Figure IV-15. Comparison of pressure data from CFD analysis and experimental results for 90 mph**

80
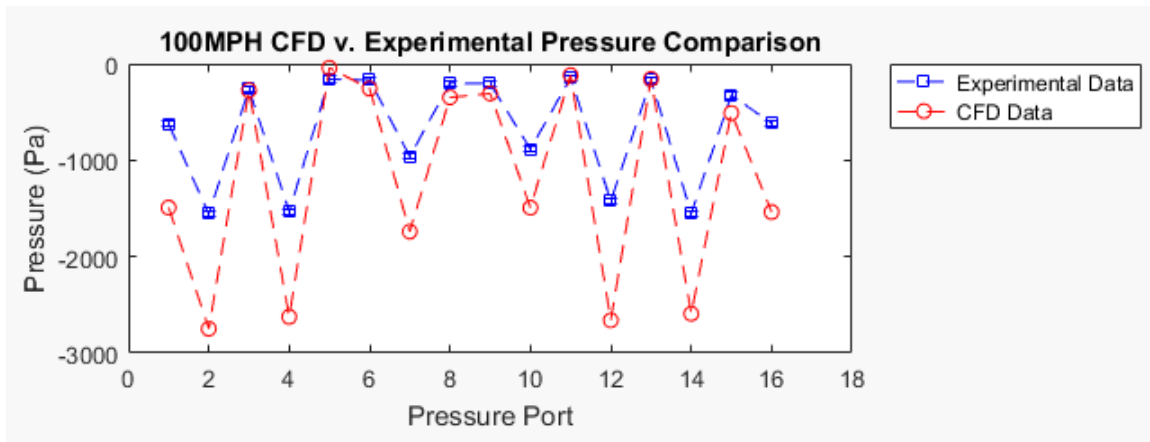
**Figure IV-16. Comparison of pressure data from CFD analysis and experimental results for 100 mph**

The pressure profiles shown in each of the comparisons for velocities tested and analyzed are consistent between experimental and CFD data. It is evident from the figures, however, that the magnitude of the pressures vary between CFD analysis and experimentation. The magnitudes for pressure in the experimental data are consistently less than the pressure exported from the CFD analysis. This could be attributed to a number of factors. First, the CFD analysis did not analyze the deformed VLTAV structure within a simulated wind tunnel or with a mounting structure behind the VLTAV. The CFD analysis was conducted assuming freestream flow around the structure without any attachments or wind tunnel boundaries modeled as shown in Figure II-13. Also, the CFD analysis assumes a perfectly smooth surface. The additively manufactured model, however, does not create a structure with a perfectly smooth surface which could account for some of the pressure magnitude losses. The coefficient of drag for the deformed shape was also compared to the original data correlation for a perfect sphere, but the comparison was not included in the body of this thesis. The data is included in Appendix C to show

81

the shift in the drag crisis as is expected for a deformed shape. The data is included in the appendix because the results in the final structural analysis shown in the subsequent section are based off of the pressure profile not the drag data.

## 4.6    Structural Analysis with Aerodynamic Effects

As a result of the pressure profiles of CFD and wind tunnel data matching well, there is high confidence in the pressure profile provided from CFD analysis. The CFD data provides higher fidelity in the pressure profile on the surface of the deformed VLTAV structure as compared to the 16 data points collected at each velocity from wind tunnel results. The higher fidelity provided from the CFD analysis is ideal for creating the pressure distribution on the surface of the membrane when conducting the structural analysis in Abaqus. Figure IV-17 indicates the results from the structural analysis with aerodynamic effects considered for the celestial icosahedron VLTAV.
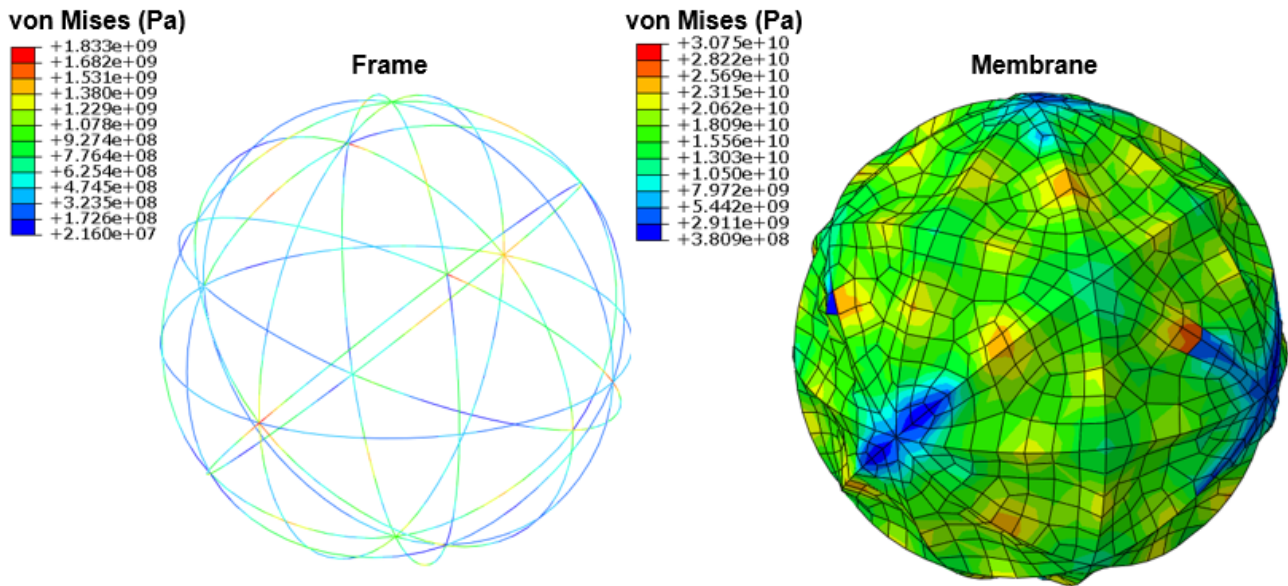


**Figure IV-17. Maximum von Mises stress in the frame and membrane of the celestial icosahedron VLTAV with aerodynamic pressure applied**

The results shown are associated with a structural analysis conducted on the celestial icosahedron VLTAV with a pressure profile applied representative of approximately $15.6 \frac{m}{s}$ (35 mph) flow. This is the highest equivalent velocity for which data was taken during wind tunnel analysis. Table IV-3 shows the comparison of the von Mises maximum stress in the frame and in the membrane with the material properties of CNT composite and graphene for the frame and membrane respectively.

**Table IV-3. Material properties compared to structural analysis results**

| Material | Yield Stress (GPa) | Maximum Stress From Analysis (GPa) | Factor of Safety |
|---|---|---|---|
| CNT (Frame) | 3.8 | 1.8 | 2.1 |
| Graphene (Membrane) | 50 | 30.8 | 1.6 |

The results from the structural analysis with aerodynamic effects applied shows the factor of safety for the frame and the membrane are above 1.5. The addition of the pressure profile from the CFD data does not significantly affect the maximum stress in the frame or membrane to reduce the factor of safety below 1.5.

## 4.7    Summary

The results presented in this chapter show the effect of applying the initial step of a fluid-structure interaction to the celestial icosahedron VLTAV. The studies conducted to include validation of experimentation, stagnation pressure comparison, and the follow-on automatic stabilization study show confidence in the experimental setup as well as the analysis methods used in the research conducted for this thesis. The results from comparing CFD and wind tunnel results show agreement between

83

the pressure profiles provided by each data set. Therefore, the CFD data provided an adequate representation of the pressures on the deformed VLTAV which were used as an input into the structural analysis model. The structural analysis of the celestial icosahedron VLTAV with aerodynamic pressures applied did not show significant degradation of the factor of safety for the frame or membrane.

## V.    Conclusions and Recommendations

The results demonstrated that the wind tunnel setup is validated through the analysis of the perfectly spherical model. The assumption that aerodynamic effects have limited significance on the deformation of the VLTAV is validated through the stagnation pressure scenario analysis. The region of large deformation in the membrane at low loads is determined to be a physical phenomenon by conducting the automatic stabilization study. The CFD data is validated through the comparison with wind tunnel pressure profiles. Lastly, the structural analysis of the celestial icosahedron VLTAV with aerodynamic pressures applied indicates an insignificant change in maximum stress and therefore does not reduce the factor of safety below 1.5.

The analysis and wind tunnel experiments with the perfect sphere show that the model used for experimentation is a reasonable design. Since a wind tunnel model had to be designed for analyzing the deformed VLTAV structure, first a spherical test article with interfaces for the AFIT wind tunnel was designed. This test article allowed for the identification of design flaws before manufacturing a test article for the deformed structure. Also, it provided confidence in the experimental data of the

84

deformed body because the sphere's experimental data could be compared to previously published data. The comparison of the experimental data with previously published data revealed that the test article design was valid and could be used as a baseline for the deformed shape.

The structural analysis, which took into account the stagnation pressure for a $17.8816\frac{m}{s}$ airflow applied to one hemisphere of the structural model, provided confidence in some of the assumptions that were made. One assumption made was that the VLTAV structure would not significantly deform due to aerodynamic effects as compared to the structural load the vehicle endures due to the internal vacuum. This assumption was validated through the stagnation pressure scenario because applying a stagnation pressure to one hemisphere only increased the deformation by approximately 1%.

In the research conducted by Kyle Moore, he experienced a phenomenon in which the deformation of the membrane initially changed drastically in a structural analysis of the VLTAV where the load applied was less than 10% of sea level pressure. In Moore's future research section he proposed, "The behavior observed in this research may be due to numerical inaccuracies within the finite element model, or it could be the product of some physical phenomena not yet known" [1]. The study conducted on a small triangular portion of the VLTAV demonstrated the same phenomenon while allowing for more efficient run times. The analysis varied parameters within the adaptive automatic stabilization tool within Abaqus to determine if the phenomenon was numerical or physical. Since varying the parameters did not have an effect on the region, it is presumed that the phenomenon is a physical one.

85

The CFD and experimental results were compared to determine if the CFD results could be used within the structural analysis of the VLTAV to gain an understanding of the fluid-structure interaction of airflow around the vehicle. The CFD pressure profile matched the experimental results well at higher velocities where the sensitivity in the pressure scanner had high fidelity compared to the pressures measured. Therefore, the CFD pressure profile can be used to analyze the structural response to the fluid flow around the VLTAV.

Lastly, after analyzing the pressure profile as a load within the structural analysis model, the results showed that the structural integrity of the celestial icosahedron VLTAV was not significantly affected. For the atmospheric conditions considered in this research, the structural analysis indicates that the VLTAV does not experience high enough stress to be at risk of collapse. Therefore, it is concluded that a full nonlinear fluid-structure interaction analysis is not necessary for the celestial icosahedron design. The aerodynamics do not significantly affect the stress in the structure compared to the stress associated with a symmetrically applied atmospheric pressure which simulates an internal vacuum in the structure.

After conducting the research for this thesis, it is recommended that CFD analysis be conducted for a much higher velocity than what was represented in this thesis. The effective air velocity researched in this thesis was approximately $15\frac{m}{s}$ (35 mph). This is because the wind tunnel has a constraint on airspeed. However, because confidence in the CFD model was shown, the CFD model could be run at higher velocity to ensure the conclusions stated previously are valid for a higher velocity.

# Appendix A. Matlab interpolation file

**Point Cloud Interpolation to Create Finer Cloud**

```
clc;clear all; close all
```

Inputs

```
gridsize        = 200; % total cloud points = gridsize^2
numInterpSteps  = 200;  % Number of interpolation steps ("equitorial bands")
interpMethod    = 'natural'; % Interpolation method, methods: 'natural', 'linear',
'nearest', 'cubic'
input_file_name = 'Cylinder'; % name of file containing x,y,z points (no headers)
```

Point Cloud Interpolation

```
PC = importdata([input_file_name '.txt']);
[az,el,r] = cart2sph(PC(:,1),PC(:,2),PC(:,3));
    % az = azimuth angle, counterclockwise in the x-y plane in radians from the positive
x-axis, within [-pi pi]
    % el = elevation angle in radians from the x-y plane, within [-pi/2, pi/2]
    % r  = radius
PCs = [az,el,r]; % Original point cloud in spherical coordinates

% New Grid Points (Angles)
azq   = linspace(-pi,pi,gridsize)';
elq   = linspace(-pi/2,pi/2,gridsize)';
count = 1;
AZEL  = zeros(length(elq)*length(azq), 2);
for j = 1:length(azq)
    for k = 1:length(elq)
        AZEL(count,:) = [azq(j) elq(k)];
        count = count + 1;
    end
end
azq = AZEL(:,1);
elq = AZEL(:,2);

% Interpolation (Radius)
[rq,C] = interp_spherical(az,el,r,azq,elq,interpMethod,numInterpSteps);
[xq,yq,zq] = sph2cart(azq,elq,rq);
PCq = [xq,yq,zq];
```

Plot

```
figure
subplot(1,2,1)
    pcshow(PC);
    title('Original'); xlabel('x'); ylabel('y'); zlabel('z')
subplot(1,2,2)
    hold on
    pcshow(PCq);
```

```matlab
    title('Interpolated'); xlabel('x'); ylabel('y'); zlabel('z')
    hold off
```

New Point Cloud Save

```matlab
fid = fopen([input_file_name '_' num2str(length(xq)) 'points' '.txt'],'wt');
for ii = 1:size(PCq,1)
    fprintf(fid,'%g\t',PCq(ii,:));
    fprintf(fid,'\n');
end
fclose(fid);
```

*Published with MATLAB® R2016a*

88

## Interpolate into Spherical Coordinate System

```matlab
function [varargout]=interp_spherical(varargin)
% function [Ri,Ci]=interp_spherical(T,P,R,Ti,Pi,interpMethod,numberInterpSteps)
% ------------------------------------------------------------------------
% The function |interp_spherical| interpolates in a spherical coordinate
% sytem using standard interp2 type inter"equator" such that polar artifacts
% can be minimized. For each interpolapolation methods or those based on
% Delaunay tesselations in the angular space such as natural neighbour
% interpolation method. Standard spherical interpolation of this type
% creates artifacts at the poles. Hence |interp_spherical| splits the
% interpolation up into a number of steps (set by numberInterpSteps). The
% function aims to interpolate at the tion step the interpolation problem is
% rotated such that the currect "equatorial band" is centered at the
% equator.
%
% Kevin Mattheus Moerman
% gibbon.toolbox@gmail.com
%
% Change log:
% 2017/09/13 Removed demo mode. Improved input parsing
%
%-------------------------------------------------------------------------
```

### Parse input

```matlab
switch nargin
    case 5
        T=varargin{1};
        P=varargin{2};
        R=varargin{3};
        Ti=varargin{4};
        Pi=varargin{5};
        interpMethod='natural';
        numberInterpSteps=10;
    case 6
        T=varargin{1};
        P=varargin{2};
        R=varargin{3};
        Ti=varargin{4};
        Pi=varargin{5};
        interpMethod=varargin{6};
        numberInterpSteps=10;
    case 7
        T=varargin{1};
        P=varargin{2};
        R=varargin{3};
        Ti=varargin{4};
        Pi=varargin{5};
        interpMethod=varargin{6};
        numberInterpSteps=varargin{7};
    otherwise
```

```matlab
            error('Wrong number of input arguments');
    end
if numberInterpSteps==1
    [Ri]=interp_spherical_part(T,P,R,Ti,Pi,interpMethod);
    switch nargout
        case 1
            varargout{1}=Ri;
        case 2
            varargout{1}=Ri;
            varargout{2}=Ri;
    end
else
    %Getting source vertices
    V=zeros(size(R,1),3);
    [V(:,1),V(:,2),V(:,3)] = sph2cart(T,P,R);

    %Getting target vertices
    Vi=zeros(size(Pi,1),3);
    [Vi(:,1),Vi(:,2),Vi(:,3)] = sph2cart(Ti,Pi,ones(size(Pi)));

    %Determine the rotation settings
    rotationRange=linspace(0,pi,numberInterpSteps+1);
    rotationRange=rotationRange(1:end-1);
    phiThreshold=diff(rotationRange(1:2))/2;

    %Step wise spherical interpolation around equator
    indDone=[];
    Ri=ones(size(Vi,1),1);
    Ci=ones(size(Vi,1),1);
    for q=1:1:numberInterpSteps
        %Rotate so that points of interest are at equator
        [DCM,~]=euler2DCM([rotationRange(q) 0 0]); %Direction cosines matrix
        Vr=V*DCM; %Rotated source vertices
        Vri=Vi*DCM; %Rotated target vertices

        %Convert to spherical coordinates
        [Tr,Pr,Rr]=cart2sph(Vr(:,1),Vr(:,2),Vr(:,3)); %Source
        [Ti,Pi,~]=cart2sph(Vri(:,1),Vri(:,2),Vri(:,3)); %Target

        %Get indices for the current target vertices
        indDoNow=find(Pi>=-phiThreshold & Pi<=phiThreshold);
        indDoNow=indDoNow(~ismember(indDoNow,indDone)); %remove ones done already

        %Interpolate region
        [Ri_step]=interp_spherical_part(Tr,Pr,Rr,Ti(indDoNow),Pi(indDoNow),interpMethod);
        Ri(indDoNow)=Ri_step; %Setting new radii
        Ci(indDoNow)=q; %Store iteration index for current points

        indDone=unique([indDone; indDoNow]); %Adding vertix indices to done list
    end

    varargout{1}=Ri;
```

90

```matlab
        varargout{2}=Ci;

    end

end

function [Ri]=interp_spherical_part(T,P,R,Ti,Pi,interpMethod)
%Tesselate data above, below, left and right to aid interpolation (and
%avoid some polar- and edge artifacts)
T=[T+2*pi; T+2*pi; T+2*pi; T; T; T; T-2*pi; T-2*pi; T-2*pi];
P=[P-pi; P; P+pi; P-pi; P; P+pi; P-pi; P; P+pi];
R=repmat(R,[9,1]);

%Removing double points
fRound=1e5; %Rounding factor for unique test
[~,indUni,~]=unique(round([T P R]*fRound)/fRound,'rows');
P=P(indUni);
T=T(indUni);
R=R(indUni);

if strcmp(interpMethod,'natural') || strcmp(interpMethod,'linear') ||
strcmp(interpMethod,'nearest') %TriScatterdInterp function
    F_delaunay=scatteredInterpolant([T P],R,interpMethod); %interpolator
    Ri=F_delaunay([Ti Pi]);
elseif strcmp(interpMethod,'cubic') %Griddata function
    Ri = griddata(T,P,R,Ti,Pi,interpMethod);
else
    error('Invalid interpolation method. The following methods are supported: linear,
nearest, and cubic')
end
end
```

*GIBBON footer text*

License: https://github.com/gibbonCode/GIBBON/blob/master/LICENSE

GIBBON: The Geometry and Image-based Bioengineering add-On. A toolbox for image segmentation, image-based modeling, meshing, and finite element analysis.

Copyright (C) 2018  Kevin Mattheus Moerman

This program is free software: you can redistribute it and/or modify it under the terms of the GNU General Public License as published by the Free Software Foundation, either version 3 of the License, or (at your option) any later version.

This program is distributed in the hope that it will be useful, but WITHOUT ANY WARRANTY; without even the implied warranty of MERCHANTABILITY or FITNESS FOR A PARTICULAR PURPOSE.  See the GNU General Public License for more details.

You should have received a copy of the GNU General Public License along with this program.  If not, see http://www.gnu.org/licenses/.

*Published with MATLAB® R2016a*

# Appendix B. MATLAB script to compare wind tunnel and CFD data

```matlab
clc; close all; clear all;

xyzExp = xlsread('xyzExp.xlsx','B2:D17'); %Read the xyz spatial position of pressure
ports
xyzExp = xyzExp.*0.0254; %Convert port position from in to m
LxyzExp=length(xyzExp); %Set the length of the pressure port file as an index variable

PercDiff=zeros([9 16]); %Preallocate Percent Difference table

ports=[1:LxyzExp]; %Creates array of how many ports are used

max_pres=zeros([1 9]); %Preallocates an array for maximum pressures

figure(); %Creates figure in which all velocity comparison plots will be placed

for h=20:10:100 %increments through 20mph run to 100mph run at 10mph increments
    %iterates through CFD filenames
    filenameCFD=[num2str(h),' ','MPH.xlsx'];

    %imports CFD data from file for this iteration
    CFD_data = xlsread(filenameCFD,'A2:D4647');

    %Creates a variable for the number of data points in CFD file
    LCFD=length(CFD_data);

    %Preallocates array for a row sum the same length as CFD file
    row_sum=zeros(LCFD,1);

    %iterates through Experimental filenames
    filenameExp = ['Experiment_4Feb19_',num2str(h),'mph.xlsx'];

    %imports Experimental data from file for this iteration
    Exp_data = xlsread(filenameExp,'F2:U18');

    %Preallocates vector for storing CFD index of point that is closest to an xyz
location for an experimental pressure port
    indexVector=zeros([1 LxyzExp]);

    for i=1:LxyzExp;%iterates through the total number of pressure ports

        %iterates through the total number of CFD data points to find closest point to
pressure port xyz location
        for j=1:LCFD;

            %calculates the difference in xyz location for CFD point and pressure port
            Dif = xyzExp(i,:)-CFD_data(j,1:3);
```

```matlab
            %sums the xyz differences to calculate an error
            sum_new = sum(abs(Dif));

            %assigns the error for each point in the CFD file compared to a single xyz
location for a pressure port
            row_sum(j)=sum_new;
        end

        %finds the minimum error and assigns an index (row) from the CFD file for the xyz
location
        indexVector(i)=find(row_sum == min(row_sum));
    end

    %turns the CFD pressures into a row instead of a column
    CFDPres=transpose(CFD_data(indexVector, 4));

    %averages the pressure for each pressure port over a run at a particluar velocity
    ExpPres=(sum(Exp_data)./size(Exp_data, 1))*6894.76;

    %Finds the maximum pressure for each particular velocity run
    max_pres((h/10)-1)=max(abs(ExpPres));

    %indexes the percent differences for pressures for each velocity run
    x=(h/10)-1;

    %calculates the percent difference for every pressure port xyz location accross for
every velocity run
    PercDiff(x, 1:16)=abs(minus(CFDPres, ExpPres)./CFDPres)*100;

    %creates a 3x3 matrix of subplots within the preallocated figure to place pressure
profile comparisons
    subplot(3, 3, ((h/10)-1));

    %assigns the error from the pressure scanner
    err = 30.9*[1 1 1 1 1 1 1 1 1 1 1 1 1 1 1 1];

    %plots the pressure data for every port with error bars
    errorbar(ports, ExpPres, err, '--sb');
    hold on

    %plots data from CFD at each port
    plot(ports, CFDPres, '--or');

    %creates title for comparison plots
    title([num2str(h),'MPH CFD v. Experimental Pressure Comparison']);

    %labels the x axes
    xlabel('Pressure Port');

    %labels the y axes
    ylabel('Pressure (Pa)');
```
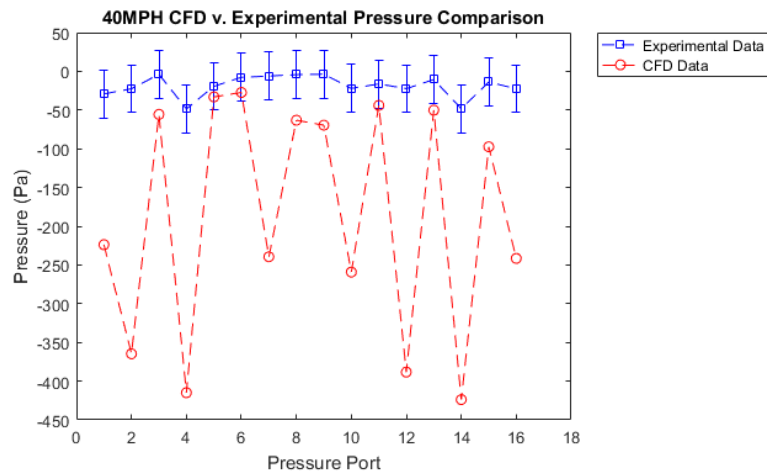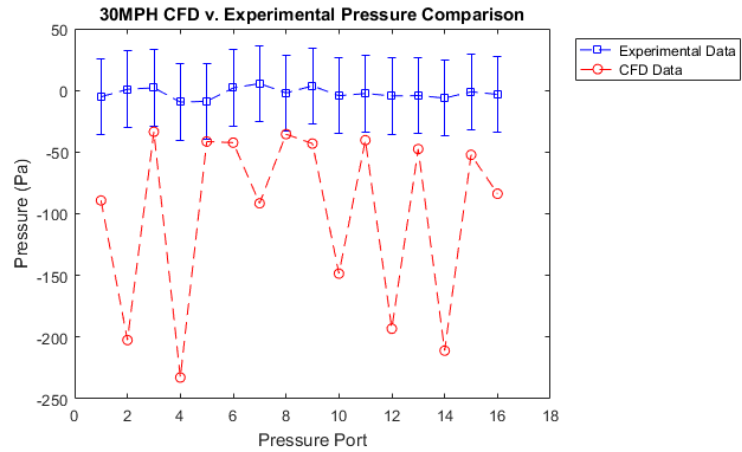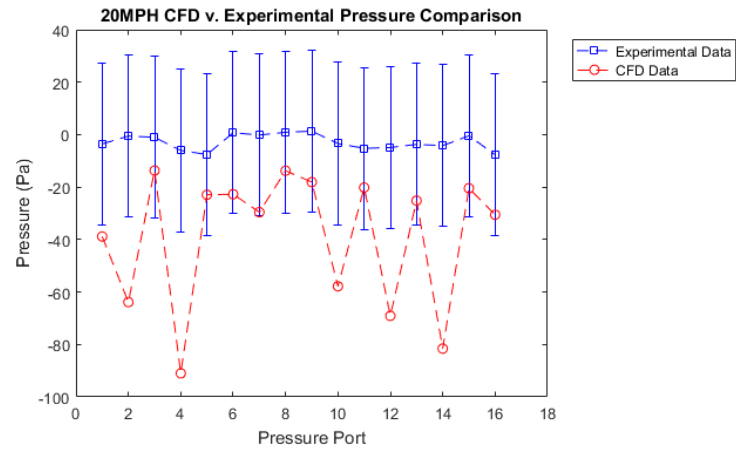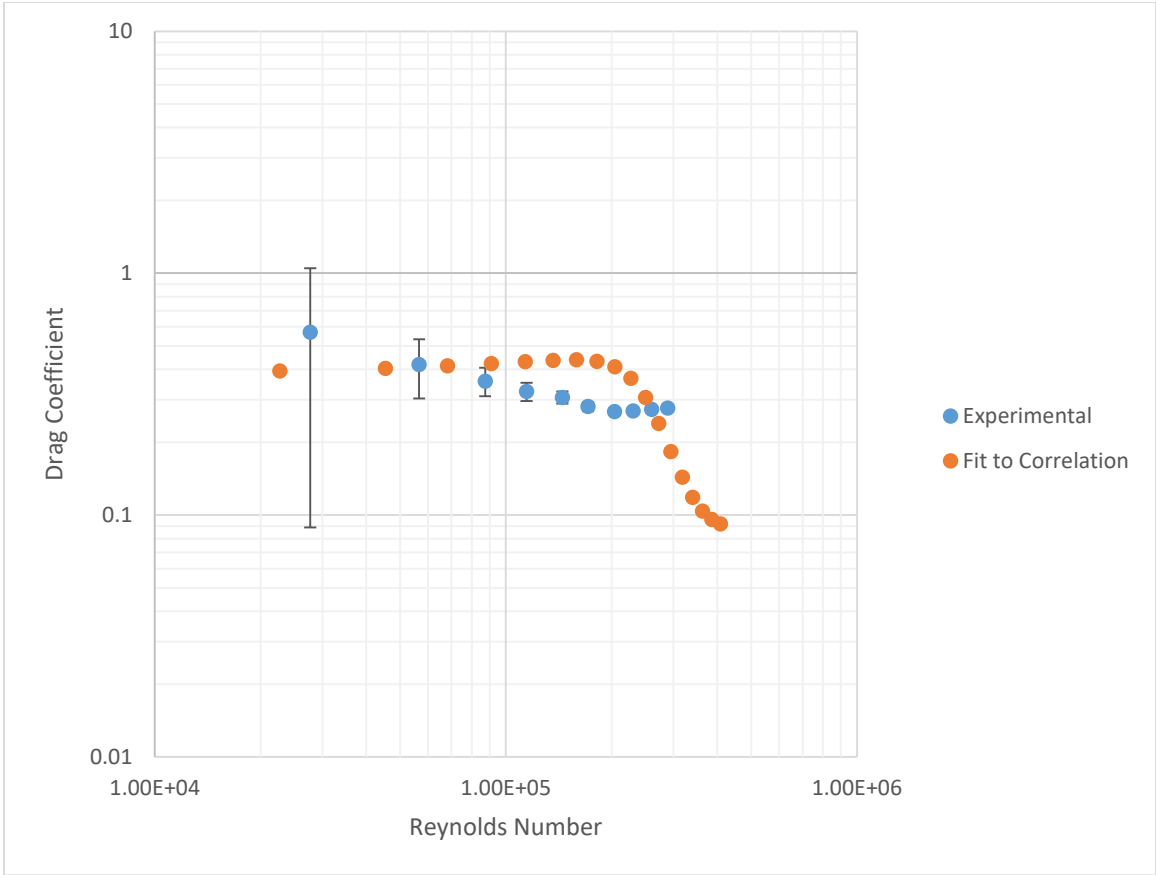
93

```
    %creates a legend for the plots
    legend('Experimental Data','CFD Data','Location','northeastoutside');
end
```

94

# Appendix C. Deformed VLTAV pressure comparisons and drag coefficient data

## Bibliography

[1]     K. D. Moore, "Quasi-Static Nonlinear Analysis of a Celestial Icosahedron Shaped Vacuum Lighter than Air Vehicle," Master's Thesis, Air Force Institute of Technology, Wright Patterson AFB, Ohio, 2018.

[2]     R. Adorno-rodriguez, "Nonlinear Structural Analysis of an Icosahedron and its Application to Lighter than Air Vehicles Under a Vacuum," Master's Thesis, Air Force Institute of Technology, Wright Patterson AFB, Ohio, 2014.

[3]     B. Cranston, "Conceptual Design, Structural Analysis, and Design Space Exploration of a Vacuum Lighter than Air Vehicle," Ph.D. dissertation, Air Force Institute of Technology, Wright Patterson AFB, Ohio, 2014.

[4]     D. Noel, "LIGHTER THAN AIR CRAFT USING VACUUM," *Corresp. Specul. Sci. Technol.*, vol. 6, no. 3, pp. 262–266, 1983.

[5]     "What Goes Up...," *Libraries University of Wisconsin-Madison*, 2016. [Online]. Available: https://www.library.wisc.edu/specialcollections/2016/05/19/what-goes-up/. [Accessed: 06-Sep-2018].

[6]     M. Alghofaily, "Finite Element Analysis and Experimentation of an Icosahedron Frame under Compression," Master's Thesis, Air Force Institute of Technology, Wright Patterson AFB, Ohio, 2015.

[7]     D. Howe, "Lighter than Air Vehicles," *Encycl. Aerosp. Eng.*, pp. 1–14, 2010.

[8]     L. C. Cadwallader and J. S. Herring, "Safety issues with hydrogen as a vehicle fuel," *Idaho Natl. Eng. Environ. Lab.*, pp. 1–13, 1999.

[9]     K. Kendig, *Sink or Float: Thought Problems in Math and Physics*. The Mathematical Association of America, 2008.

97

[10] B. Carroll, "Archimedes' Principle." [Online]. Available: https://physics.weber.edu/carroll/archimedes/principle.htm.

[11] T. T. Metlen, "Design of a Lighter than Air Vehicle that Achieves Positive Buoyancy in Air Using a Vacuum," Master's Thesis, Air Force Institute of Technology, Wright Patterson AFB, Ohio, 2012.

[12] R. B. Fuller, "Building Construction," 1954.

[13] W. Ren and H.-M. Cheng, "The Global Growth of Graphene," *Nat. Nanotechnol.*, vol. 9, no. 10, pp. 726–730, 2014.

[14] Q. F. Cheng *et al.*, "Carbon nanotube/epoxy composites fabricated by resin transfer molding," *Carbon N. Y.*, vol. 48, no. 1, pp. 260–266, 2010.

[15] Q. F. Cheng *et al.*, "High Mechanical Performance Composite Conductor: Multi-Walled Carbon Nanotube Sheet/Bismaleimide Nanocomposites," *Adv. Funct. Mater.*, vol. 48, no. 1, pp. 260–266, 2010.

[16] B. S. El-tawil and G. G. Deierlein, "Understanding Nonlinear Analysis," no. June, pp. 647–655, 2001.

[17] R. Cook, D. Malkus, M. Plesha, and R. Witt, *Concepts and Applications of Finite Element Analysis*, Fourth. Hoboken: John Wiley & Sons. Inc., 2002.

[18] Dassault Systemes, "Abaqus 6.14 Online Documentation," 2014. [Online]. Available: http://dsk.ippt.pan.pl/docs/abaqus/v6.13/index.html.

[19] R. de Borst, M. A. Crisfield, J. J. C. Remmers, and C. V. Verhoosel, *Non-linear Finite Element Analysis of Solids and Structures*, Second. West Sussex: John Wiley & Sons. Inc., 2012.

[20] T. J. Ypma, "Historical development of the Newton-Raphson Method," *SIAM*

*Rev.*, vol. 37, no. 4, pp. 531–551, 1995.

[21]    "Solving Nonlinear Problems." MIT Abaqus Docs, 2017.

[22]    F. F. Abraham, "Functional dependence of drag coefficient of a sphere on reynolds number," *Phys. Fluids*, vol. 13, no. 8, pp. 2194–2195, 1970.

[23]    F. Morrison, "Data correlation for drag coefficient for sphere," *... Michigan Technol. Univ. Houghton, MI, www ...*, vol. 6, no. April, pp. 1–2, 2010.

[24]    G. S. West and C. J. Apelt, "The effects of tunnel blockage and aspect ratio on the mean flow past a circular cylinder with Reynolds numbers between 10000 and 100000," *J. Fluid Mech.*, vol. 114, no. January 1982, pp. 361–377, 1982.

[25]    M. Wolff, K. Mcintosh, and M. Phillipp, "ARS Consulting Report," 2018.

[26]    "Miniature Electronic Pressure Scanners Data Sheet," *Specifications*. A-Tech Instruments LTD., 2000. Available: http://www.a-tech.ca/Product/Series/38/ESP-16HD_Miniature_Pressure_Scanner/?tab=1. [Accessed: 20-Nov-2018]

[27]    "Ansys Fluent 12.0 Theory Guide." ANSYS, Inc., pp. 49–53, 2009.

[28]    "Reynolds Number," *Engineering Toolbox*, 2003. [Online]. Available: https://www.engineeringtoolbox.com/reynolds-number-d_237.html. [Accessed: 06-Sep-2018].

[29]    "Drag of a Sphere," *National Aeronautics and Space Administration*, 2015. [Online]. Available: https://www.grc.nasa.gov/www/k-12/airplane/dragsphere.html. [Accessed: 29-Oct-2018].

99

# REPORT DOCUMENTATION PAGE

*Form Approved*
*OMB No. 0704-0188*

The public reporting burden for this collection of information is estimated to average 1 hour per response, including the time for reviewing instructions, searching existing data sources, gathering and maintaining the data needed, and completing and reviewing the collection of information. Send comments regarding this burden estimate or any other aspect of this collection of information, including suggestions for reducing the burden, to Department of Defense, Washington Headquarters Services, Directorate for Information Operations and Reports (0704-0188), 1215 Jefferson Davis Highway, Suite 1204, Arlington, VA 22202-4302. Respondents should be aware that notwithstanding any other provision of law, no person shall be subject to any penalty for failing to comply with a collection of information if it does not display a currently valid OMB control number.
**PLEASE DO NOT RETURN YOUR FORM TO THE ABOVE ADDRESS.**

| 1. REPORT DATE *(DD-MM-YYYY)* | 2. REPORT TYPE | 3. DATES COVERED *(From - To)* |
|---|---|---|
| 22-03-2019 | Master's Thesis | Sep 17-Mar 19 |

**4. TITLE AND SUBTITLE**

INITIAL STAGE OF FLUID-STRUCTURE INTERACTION OF A CELESTIAL ICOSAHEDRON SHAPED VACUUM LIGHTER THAN AIR VECHICLE

**5a. CONTRACT NUMBER**

**5b. GRANT NUMBER**

**5c. PROGRAM ELEMENT NUMBER**

**6. AUTHOR(S)**

Graves, Dustin, P., Capt

**5d. PROJECT NUMBER**

**5e. TASK NUMBER**

**5f. WORK UNIT NUMBER**

**7. PERFORMING ORGANIZATION NAME(S) AND ADDRESS(ES)**

Air Force Institute of Technology
Graduate School of Engineering and Management (AFIT/EN)
2950 Hobson Way
Wright-Patterson AFB OH 45433-7765

**8. PERFORMING ORGANIZATION REPORT NUMBER**

AFIT-ENY-MS-19-M-216

**9. SPONSORING/MONITORING AGENCY NAME(S) AND ADDRESS(ES)**

AFOSR/RTA
Att: Dr. Jaimie Tiley
875 N. Randolph Street
Suite 325, Room 3112
Arlington, Va 22203-1768    (703) 588-8316

**10. SPONSOR/MONITOR'S ACRONYM(S)**

AFOSR

**11. SPONSOR/MONITOR'S REPORT NUMBER(S)**

**12. DISTRIBUTION/AVAILABILITY STATEMENT**

DISTRIBUTION STATEMENT A:
APPROVED FOR PUBLIC RELEASE; DISTRIBUTION UNLIMITED.

**13. SUPPLEMENTARY NOTES**

**14. ABSTRACT**

The analysis of a celestial icosahedron geometry is considered as a potential design for a Vacuum Lighter than Air Vehicle (VLTAV). The goal of the analysis is ultimately to understand the fluid-structure interaction of the VLTAV and the surrounding airflow. Up to this point, previous research analyzed the celestial icosahedron VLTAV in relation to withstanding a symmetric sea-level pressure applied to the membrane of the structure. This scenario simulates an internal vacuum being applied in the worst-case atmospheric environmental condition. The next step in analysis is to determine the aerodynamic effects of the geometry. The experimental setup for obtaining aerodynamic effects is validated prior to analyzing the deformed celestial icosahedron geometry by analyzing a perfect sphere utilizing the same manufacturing process and setup expected to be adopted for the celestial icosahedron experiments. The data received from Computational Fluid Dynamics (CFD) analysis of the deformed structure in collaboration with Wright State University is used to determine the significance of aerodynamic effects on the structure. The pressure profiles experienced in the wind tunnel experiments and CFD analysis are comparatively similar. Therefore, the CFD data is used to conduct a structural analysis in which aerodynamic effects are incorporated.

**15. SUBJECT TERMS**

Fluid-Structure Interaction, Lighter than Air Vehicle, Structural Analysis, Computational Fluid Dynamics

| 16. SECURITY CLASSIFICATION OF: | | | 17. LIMITATION OF ABSTRACT | 18. NUMBER OF PAGES | 19a. NAME OF RESPONSIBLE PERSON |
|---|---|---|---|---|---|
| a. REPORT | b. ABSTRACT | c. THIS PAGE | | | Dr. Anthony N. Palazotto, AFIT/ENY |
| U | U | U | UU | 99 | 19b. TELEPHONE NUMBER *(Include area code)* (937) 785-3636 x4599 anthony.palazotto@afit.edu |

Standard Form 298 (Rev. 8/98)
Prescribed by ANSI Std. Z39.18